Fate and Transport of Carbon Nanomaterials in Unsaturated and Saturated Soils

U.S. EPA Agreement Number: R832535

Final Report

Prepared by:

Kurt D. Pennell, Ph.D., P.E.[1]	Principal Investigator
Joseph B. Hughes, Ph.D., P.E.[2]	Co-Principal Investigator
Linda M. Abriola, Ph.D.[1]	Co-Principal Investigator
Yusong Li, Ph.D., P.E.	Post-Doctoral Fellow
Yonggang Wang, Ph.D.	Graduate Research Assistant

[1]Department of Civil & Environmental Engineering
Tufts University
200 College Avenue
Medford, MA 02155

[2]School of Civil and Environmental Engineering
Georgia Institute of Technology
Environmental Science and Technology Building
311 Ferst Drive
Atlanta, GA 30332-0512

January 26, 2011

DISCLAIMER

The research reported herein was supported by grant RD-832535 from the U.S. Environmental Protection Agency's Science to Achieve Results (STAR) program. The work has not been subject to EPA review, and therefore, does not necessarily reflect the views of the Agency, and no official endorsement should be inferred.

TABLE OF CONTENTS

ACKNOWLEDGEMENTS

The research described in this final report was supported by the U.S. Environmental Protection Agency through the Science to Achieve Results (STAR) program. We wish to thank Drs. Mitch Lasat and Paul Shapiro, program managers for the project, for their administrative assistance and support of the project.

We thank Dr. Susan Burns and Dr. Nils Kroeger for use of their Brookhaven ZetaPlus and Malvern Zetasizer instruments, respectively, Dr. Jed Costanza for performing GC-MS analysis of THF and GBL, Dr. Menachem (Meny) Elimelech for his helpful suggestions, Dr. Sharon Walker for performing streaming potential measurements, .

CHAPTER 1

INTRODUCTION

1.1 RESEARCH MOTIVATION AND SCOPE

Widespread production and application of novel materials at the nanoscale is expected to increase dramatically over the next decade. Such an increase in production and dissemination will inevitably lead to the release of nanoscale compounds into the environment, either from industrial sources or through disposal in municipal waste streams. The current understanding of nanomaterial fate and transport in subsurface environments is quite limited. For example, it is not known how such compounds will interact with soil matrices, whether they can be modeled as colloidal particles using classic particle filtration theory, and how unsaturated soil conditions will impact transport and retention. Thus, the overall goal of this project was to improve our knowledge of carbon-based nanoparticle fate and transport in porous media, including reference solids and natural soils. Detailed laboratory experiments were conducted to explore the fate and transport of these engineered nanomaterials as a function of soil properties in one-dimensional systems. The research was specifically designed to couple detailed experimental studies with the development and evaluation of mathematical models. Thus, in addition to expanding our fundamental knowledge of nanomaterial fate and transport in the environment, one of the key benefits of this project was the development of a nanoparticle transport simulator. The project was structured around the three tasks, which are summarized below:

Task 1. Investigate the fate and transport of carbon-based nanomaterials in water-saturated soils. The effects of flow velocity, grain size, ionic strength and species on nanoscale fullerene (nC_{60}) aggregate and multi-walled carbon nanotube (MWCNT) transport and retention behavior was evaluated in one-dimensional columns packed with quartz sands or natural soils.

Task 2. Investigate the effects of stabilizing agents on the transport of (C_{60}) nanomaterials in porous media. The effects of natural (humic and fulvic acids) and anthropogenic (surfactants) stabilizing agents on the transport and retention of fullerene (nC_{60}) aggregates in quartz sands was evaluated in a series of column experiments.

Task 3. Develop and evaluate a numerical simulator to describe C_{60} nanomaterial transport, retention and release in porous media. Mathematical models were developed and implemented in a one dimensional transport simulator, to predict nanomaterial transport and retention in the experimental systems. The numerical simulator was validated and refined based on comparisons between model predictions and experimental data.

1.2. RESEARCH ACTIVITIES

1.2.1. TASK 1: As part of Task 1 research efforts initially focused on experimental measurement of nanoscale fullerene (nC_{60}) aggregate transport and retention in water-saturated quartz sands as a function of flow velocity, grain size, ionic strength, and ionic species. For all expe1riments, aqueous suspensions of nC_{60} aggregates were prepared from fullerene powder that was dissolved in tetrahydrofuran (THF). The C_{60}-saturated THF solution was mixed with an equal volume of water and evaporated at 75^{o}C repeatedly to remove residual THF. The resulting aqueous stock suspension contained approximately 6 mg/L of nC_{60} aggregates in purified de-ionized (DI)

water. The mean diameter of nC_{60} aggregates in this suspension was approximately 100 nm, determined by dynamic light scattering (DLS). To prepare aqueous suspensions for use in batch and column experiments, approximately 100 mL of the nC_{60} stock suspension were added to an equal volume of DI water containing either NaCl or $CaCl_2$. The final concentration of background electrolyte in the aqueous nC_{60} suspensions ranged from 1 to 100 mM, which was adjusted to pH 7.0 with $NaHCO_3$. For the transport experiments, glass columns (2.5 cm dia. X 10 or 15 cm length) were packed with either 20-30, 40-50, 80-100 or 100-140 mesh Ottawa sand and then completely saturated with water. Non-reactive tracer studies were performed to assess water flow characteristics and to determine the hydrodynamic dispersion coefficient. A pulse of nC_{60} suspension was then introduced into each column using a syringe pump, followed by nC_{60}-free solution at the same flow rate. Effluent samples were collected continuously in 15 mL sterile tubes and analyzed for nC_{60} content by ultraviolet spectroscopy. At the conclusion of each transport experiment, the columns were dissected into 1.5 cm increments and extracted to obtain nC_{60} retention profiles.

As the mean grain size of Ottawa sand decreased from 0.71 to 0.13 mm, the time required for nC_{60} appearance in the column effluent increased, while the total amount of nC_{60} transported through the column decreased. Similarly, when the pore-water velocity was decreased from ca. 8 to 1 m/day, breakthrough of nC_{60} aggregates was delayed, and was only observed in 20-30 and 40-50 mesh Ottawa sand. Thus, depending upon the grain size and flow rate, either nearly complete breakthrough of nC_{60} aggregates, or conversely, nearly complete retention of nC_{60} aggregates was observed. In column experiments conducted with 40-50 mesh Ottawa sand and 1.0 mM $CaCl_2$, nC_{60} aggregates appeared in the column effluent after approximately 1.4 pore volumes (PVs), and gradually increased to a maximum relative concentration of approximately 0.9 after introduction of 2.5 to 3.0 PVs of the nC_{60} suspension. Following reintroduction of nC_{60}-free solution, the effluent concentration of nC_{60} declined sharply, approaching a value of zero at approximately 6.5 PVs. The asymmetric shape of the effluent breakthrough curves (BTCs) suggests that deposited nC_{60} aggregates were not readily released from the Ottawa sand. When either the ionic strength was increased from 3.05 to 30.05 mM or the sand grain size was decreased from 0.335 to 0.125 mm, virtually all of nC_{60} introduced into the column was retained. When NaCl was employed as the background electrolyte, much greater transport of nC_{60} aggregates was observed through Ottawa sand compared similar experimental conditions with $CaCl_2$.

Derjaguin-Landau-Verwey-Overbeek (DLVO) theory was used to calculate electrostatic interaction energy profiles for quartz sand and nC_{60} aggregates as a function of electrolyte species and concentration. The resulting interaction energy profile for $CaCl_2$ at the lower ionic strength (3.05 mM) indicates a net repulsive force near the sand surface, which should prevent deposition of nC_{60} aggregates. However, divalent cations are known to form complexes with negatively charged surface sites, thereby reducing the repulsive surface charge, which is not accounted for by DLVO theory. In addition, a small secondary attractive region (-0.5 kT) existed approximately 33 nm from the surface, which could also contribute to nC_{60} aggregate retention. At the higher ionic strength (30.05 mM), a primary attractive force existed near the surface, consistent with the strong tendency for nC_{60} aggregates to be retained by Ottawa sand. In the presence of NaCl at 3.05 mM, a large primary repulsive force (45 kT) existed near the surface, with a small secondary minimum (-0.25 kT) approximately 38 nm from surface. This repulsive force is consistent with the minimal retention of nC_{60} aggregate observed in column experiments conducted with NaCl. At the higher ionic strength (30.05 mM), the primary

repulsive force was reduced to approximately 25 kT, while the secondary attractive region became stronger (-9 kT), consistent the greater retention of nC_{60} aggregates.

To further investigate the aggregate detachment process, a series of recovery experiments were conducted in which nC_{60} aggregates were deposited in columns packed with 100-140 mesh Ottawa sand with 1.0 mM $CaCl_2$ as the background electrolyte. This was followed by changes in flow rate, ionic strength or solution pH, addition of cosolvent or surfactant. Approximately 1% of the deposited nC_{60} aggregates were removed when the column was flushed with DI water (IS $\approx$ 0) or 50% ethanol, while doubling the flow rate or flushing with 0.1% Tween 80 resulted in negligible recovery of deposited nC_{60} aggregates. In contrast, injection of DI water (3 PV) adjusted to pH 10.0 and 12.0 resulted in substantial increases in nC_{60} effluent concentration, corresponding to the recovery of 17.2 and 27.6% of deposited mass, respectively. The effect of tube length (0.5-2, 10-30, and 100 um) on MWNT transport in Ottawa sand was evaluated in separate column studies. At the length of 0.5-2 um, MWNT transport mimicked the behavior of a non-reactive tracer. When the length was increased to either 10-30 um or 100 um, however, retention of MWNTs in sand increased to ca. 17% and 40% of total input mass, respectively.

To investigate the transport and retention of nC_{60} under more realistic conditions, column studies were conducted with Webster soil, a silty clay loam (3.3% OC) and Appling soil, a loamy coarse sand (0.75% OC). When a pulse (100 mL) of nC_{60} suspension was introduced, the spatial distribution of nC_{60} retained in Appling and Webster soils was similar, with a maximum concentration of 40 ug/g near the column inlet. As the amount of nC_{60} suspension applied to Appling soil was increased to 32.5 and 65 PVs, the nC_{60} retentions profile exhibited a peak concentration of ca. 110 and 130 μg/g, respectively. The existence of concentration plateau and the increasing penetration of nC_{60} with increasing number of PVs applied suggest that Appling soil possesses a maximum nC_{60} retention capacity of ca. 140 μg/g under these conditions.

1.2.2. TASK 2: A series of column studies was conducted in Task 2 to investigate the effects of stabilizing agents on nC_{60} transport and retention behavior. Influent nC_{60} suspensions were prepared by mixing with concentrated stock solutions containing either polyoxyethylene (20) sorbitan mono2leate (Tween 80), Suwannee River humic acid (SRHA) or Suwannee River fulvic acid (SRFA) to achieve the desired final concentration of Tween 80 (1,000 mg/L), SRHA (20 mg C/L) or SRFA (20 mg C/L). Due to concerns over the potential effects of residual THF on nC_{60} transport, an additional influent nC_{60} suspension was prepared as described above, followed by spiking with 10 mg of THF to yield a THF concentration of ca. 50 mg/L.

In the presence of SRHA or SRFA, breakthrough of nC_{60} in the column effluent occurred at approximately 1 PV, earlier than observed in similar nC_{60}-alone experiments. Once nC_{60} appeared in the column effluent, relative concentrations increased rapidly to a plateau value greater than 0.98, followed by sharp descent, with relative concentrations approaching zero at the end of pulse injection. The amount of nC_{60} retained in the columns was less than 2.9% of the injected mass, which is approximately one tenth of the nC_{60} mass retained in absence of either SRHA or SRFA. Retention of nC_{60} decreased gradually along the travel distance, with the maximum solid phase concentration of 0.18 μg/g near the column inlet.

When the nC_{60} suspension was premixed with Tween 80, nC_{60} BTCs were identical to those obtained with a non-reactive tracer (bromide), with breakthrough at approximately 1 PV followed by a rapid increase to a relative concentration (C/C_0) plateau value of 1.0. When nC_{60} was introduced into an Ottawa sand column that had been pre-treated with Tween 80, the relative

concentration of nC_{60} reached a maximum value of 0.9. In both the nC_{60}-Tween 80 mixed and pretreated experiments, a similar sharp ascent and descent in the nC_{60} BTCs was observed. No measurable amounts of retained nC_{60} were observed when 1,000 mg/L Tween 80 was mixed with the nC_{60} input suspensions. In contrast, when a surfactant-free nC_{60} suspension was delivered to columns pretreated with Tween 80, 6.3 and 7.1% of the introduced nC_{60} mass was retained in the columns. While a large fraction of the introduced nC_{60} mass was transported through Tween 80-pretreated columns (>93%), retention of nC_{60} near the column inlet was substantial, with more than 77% of total retained nC_{60} mass occurring in the first 5 cm from column inlet.

1.2.3. TASK 3: A mathematical model was developed as part of Task 3 in order to describe the transport of nC_{60} aggregates through water-saturated porous media using a modified form of the advection-dispersion reactive (ADR) transport equation. Assuming conditions of homogeneity, laminar flow, and the absence of particle-particle interactions on the surface, the one-dimensional ADR transport equation for a stable nC_{60} suspension can be written as:

$$\frac{\partial C}{\partial t} + \frac{\rho_b}{\theta_w}\frac{\partial S}{\partial t} = D_H \frac{\partial^2 C}{\partial x^2} - v_p \frac{\partial C}{\partial x} \tag{1.1}$$

where, C is the nC_{60} aggregate concentration in the aqueous phase, t is time, ρ_b is the solid bulk density, θ_w is the volumetric water content, S is the attached or solid-phase concentration of nC_{60}, D_H is the hydrodynamic dispersion coefficient, x is the travel distance, and v_p is the interstitial or pore-water velocity. Following deposition, nC_{60} aggregates may remain attached to the surface or may detach and re-enter the mobile aqueous phase. A first-order kinetic expression was used to describe the attachment and detachment of nC_{60} aggregates in water-saturated quartz sands:

$$\frac{\rho_b}{\theta_w}\frac{\partial S}{\partial t} = k_{att} C \quad \frac{\rho_b}{\theta_w} k_{det} S \tag{1.2}$$

where, k_{att} and k_{det} are the first-order attachment and detachment rate coefficients, respectively.

Results obtained from our early column studies suggested that the release of nC_{60} was negligible, and therefore, the detachment rate coefficient, k_{det}, was assumed to approach zero. In addition, the relatively constant or flat nC_{60} retention profiles observed in those column studies suggested that nC_{60} aggregate attachment approached a limiting or maximum value. Thus, equation 2 was rewritten as:

$$\frac{\rho_b}{\theta_w}\frac{\partial S}{\partial t} = k'_{att} \Psi C \tag{1.3}$$

where k'_{att} is the attachment rate coefficient at low surface coverage and ψ is a blocking function that is related to the maximum particle attachment capacity S_{max}:

$$\Psi = \frac{S_{max} \quad S}{S_{max}} \tag{1.4}$$

A numerical simulator, based upon the mathematical model described by (1), (3) and (4), successfully captured the initial gradual increase and subsequent sharp decline observed in measured nC_{60} BTCs and relatively flat retention profiles observed for different size fractions of Ottawa sand and background electrolyte conditions. In marked contrast, a model based on the

traditional filtration theory (equation (2)) failed to accurately fit either the nC_{60} effluent BTCs or retention profiles. Both the maximum retention capacity (S_{max}) and the attachment rate (k_{att}) were found to decrease with increasing sand grain size. For example, the value of S_{max} decreased from 13.8 ug/g sand to 0.8 ug /g sand as the mean grain size increased from 0.125 mm to 0.71 mm at a flow velocity of 8.0 m/day, and from 7.9 ug/g sand to 0.5 ug/g sand at the slower flow velocity of 1.0 m/day. Also, for a particular size fraction of Ottawa sand, S_{max} increased with a decrease in flow velocity, consistent with the observed delay in initial breakthrough at the lower flow rate. For example, in columns packed with 40-50 mesh Ottawa sand, initial breakthrough occurred at ca. 1.3 PVs at pore-water velocity of 7.88 m/d; whereas, nC_{60} breakthrough did not occur until ca. 4.4 PVs at a velocity of 1.03 m/d.

Based on the experimental findings, the mathematical modeling effort focused on describing the transport and retention of nC_{60} in the presence of stabilizing agents (i.e., SRHA and Tween 80). The hyper-exponential decay profile obtained for nC_{60} has been reported in colloid transport studies and attributed to a variable particle attachment rate (k_{att}) along the travel distance. Therefore, a lognormal distribution of k_{att} was selected and coupled to the clean bed filtration model. Although predictions from this model matched observations of both the measured BTCs and retention profiles, the selection of a distribution function for the attachment rate is arbitrary. Careful evaluation of the measured retention profiles revealed that the maximum nC_{60} concentration retained by the solid phase was consistent with the observed retention capacity, indicating that the maximum retention capacity of nC_{60} had been reached near the column inlet. Thus, we hypothesized that the observed hyper-exponential decay retention profile obtained for nC_{60} for the Tween 80-coated Ottawa sands resulted from an increase in the available surface area due to desorption of Tween 80. Desorbed Tween 80 in water may then adsorb onto nC_{60} aggregate surfaces, preventing nC_{60} from further attachment. Thus, a mathematical model was developed which coupled Tween 80 reactive (adsorption-desorption) transport with the deposition of nC_{60} on available surfaces. Consistent with previous laboratory studies, the model assumed that Tween 80 sorption conforms to a Langmuir isotherm model. In applying this system of equations, the value of D_H was obtained from fitting the non-reactive tracer BTCs, k_{att} and S_{2max} were obtained from prior modeling efforts, and the Langmuir parameters were obtained from batch isotherms for Tween 80 adsorption to Ottawa sand. Predictions obtained using the new model demonstrated the ability of the model to capture the gradual decrease in the maximum concentration of nC_{60} and the hyper-exponential decrease in nC_{60} retention with distance from the column inlet.

1.3. KEY RESEARCH OUTCOMES/FINDINGS

1. In water-saturated quartz sands, nC_{60} aggregate transport decreases and retention increases as mean grain size and flow rate decrease.
2. Transport and retention of nC_{60} aggregates in water-saturated porous media is strongly influenced by electrolyte species and concentration. At low ionic strength (1 mM $CaCl_2$), nC_{60} aggregates are readily transported through quartz sands, while at higher ionic strength (10-100 mM $CaCl_2$) nC_{60} aggregates are strongly retained by quartz sands. This effect may be due to bridging to adsorbed Ca^{2+} ions in the primary energy minimum.
3. Once deposited, nC_{60} aggregate retention is largely irreversible, with minimal detachment observed even after flushing with low ionic strength solutions (DI water) or solutions containing surfactant (1% Tween 80) or cosolvent (50% ethanol). Introduction of pH 12 water was required to detach substantial quantities of retained nC_{60} aggregates.

4. A mathematical model that incorporates a rate-limited attachment coefficient and a limiting retention capacity term was able to accurately simulate both nC_{60} transport and deposition in water-saturated porous media.
5. Mixing nC_{60} suspensions with stabilizing agents, including Tween 80, SRHA and SRFA, enhanced the transport, and reduced the deposition, of nC_{60} aggregates in water-saturated 40-50 mesh Ottawa sand.
6. When 40-50 mesh Ottawa sand was pretreated (coated) with Tween 80, adsorption of Tween 80 onto quartz sand surfaces reduced the retention and facilitated the transport of nC_{60} aggregates.
7. A mathematical model that simultaneously accounts for the adsorption-desorption of Tween 80 and nC_{60} attachment was able to accurately predict nC_{60} transport behavior in the presence of Tween 80.
8. In two natural soils, Appling and Webster, containing appreciable amounts of clay minerals and organic matter, complete retention of nC_{60} was observed even after introducing up to 65 PVs of nC_{60} suspension. The S_{max} nanoparticle transport model was able to capture this behavior.
9. Dispersed MWNTs were readily transport through 40-50 mesh Ottawa sand. Retention of MWNTs increased with the tube length, however, even at the manufacture reported tube length of 100 μm, more than 50% of MWNTs passed through the column.

CHAPTER 2

BACKGROUND INFORMATION

2.1. OVERVIEW OF CARBON-BASED NANOMATERIALS

As allotropes of carbon, fullerene (C_{60}) and carbon nanotubes (CNTs) have attracted particular attention from the scientific community since their discovery (Iijima, 1991; Kroto et al., 1985). Due to their unique physical and chemical properties, many applications have been proposed and implemented in various fields, such as superconduction, nonlinear optical material, sensor, personal care, and pharmaceuticals. The commercial production and use of fullerene nanomaterials will inevitably lead to their release into the environment, either from industrial sources or through disposal in municipal waste.

Although solid C_{60} is hydrophobic and has extremely low solubility in water (Fortner et al., 2005), several facile methods have recently been developed to disperse it into water in the form of aggregates without the help of stabilizing agent (Cheng et al., 2005; Fortner et al., 2005). These aggregates (referred to nC_{60}) are comprised of underivatized C_{60}, are negatively charged, and have diameters ranging from 5 to 200 nm. Such stable aqueous suspensions were soon proposed to be the most relevant form of C_{60} in environment. The subsequent cytotoxicity studies have suggested that nC_{60} is toxic to some fish, mice and human cell lines (Oberdorster, 2004; Sayes et al., 2004). Although debates over nC_{60} toxicity continue, nC_{60} is considered to be an emerging contaminant. Similar to solid C_{60}, CNTs exhibit very high hydrophobicity and extremely low water solubility. Dispersion of MWNTs into water in the presence of natural organic matter has been reported recently, and thus, the potential exists for CNTs to enter water bodies.

The concerns over potential adverse effects of nC_{60} and CNTs have initiated research on their fate in the environment. Results of several studies have demonstrated that the stability of fullerene nanoparticles is dependent upon the electrolyte species and concentration, which is attributed to the electrostatic interactions (Chen and Elimelech, 2006; Saleh et al., 2008). With an analog to colloid stability, the Derjaguin-Landau-Verwey-Overbeek (DLVO) theory has been used to qualitatively interpret nC_{60} stability. Generally, nC_{60} and CNTs can be destabilized by increasing ionic strength or by addition of multivalent ions. However, the presence of natural organic matters serves to enhance the stability of nC_{60} in suspension, even at very high monovalent electrolyte concentrations.

In parallel to the aggregation of nC_{60}, the transport and deposition behavior of nC_{60} in water-saturated porous media, such as ideal glass beads and fine sands, have been evaluated in few studies (Brant et al., 2005; Cheng et al., 2005; Espinasse et al., 2007; Lecoanet and Wiesner, 2004; Lecoanet et al., 2004). Most of these experiments were conducted in 40-50 mesh glass beads and under transition flow condition (e.g., close to laminar flow), and no particle retention data were reported in any of these studies. In the effort to identify mechanisms governing nanoparticle transport and retention, clean-bed filtration theory has been directly adopted. However, it is difficult to know whether such clean-bed filtration theory is applicable to the deposition of nC_{60} and CNTs in porous media without analyzing retention profile data. Although results of batch experiments have shown that SRHA or SRFA is able to enhance nC60 transport in porous media, the direct experimental observation in column experiments has not been

reported. In addition, majority of transport data reported to date have been primarily limited to well-defined, idealized porous media (e.g., glass beads). Far less attention has been directed toward nanoparicle transport in natural soils, where fine clay minerals and organic matter are present.

2.2. PROPERTIES OF CARBON-BASED NANOMATERIALS

Molecular C_{60} has a hollow truncated-icosahedral structure consisting of 12 pentagons and 20 hexagons with one carbon atom on each vertex and a carbon bond (single or double) along each edge (Figure 2.1). This stable structure exhibits I_h symmetry. The carbon valence (4 –) is satisfied by connecting to other carbons with one double bond (at the junction of two hexagons) and two single bonds (at the junction of a hexagon and a pentagon). Compared to diamond and graphite, solid C_{60} possesses a density of 1.65 g/cm^3, which is less than that of graphite (2.3 g/cm^3). In terms of crystalline lattice, solid C_{60} has the face centered cubic lattice structure with a lattice constant of 14.17 Å (Fischer et al., 1992; Heiney et al., 1991; Pierson, 1993) at 300 K and atmospheric pressure, which is revealed by synchrotron X-ray measurement. At temperatures below 260 K, the structure of solid C_{60} transited to simple cubic (Heiney et al., 1991; Prassides et al., 1992). Theoretically, liquid C_{60} can be obtained at high temperature and pressure, which have not been verified yet (Fortner, 2006). At elevated temperatures, sublimation of solid C_{60} occurs at 550 ^oC in inert atmosphere (e.g., Ar and He) and at normal pressure (Rausch and Braun, 2001), and at 700 ^oC in vacuum (Fortner, 2006; Ismail and Rodgers, 1992).

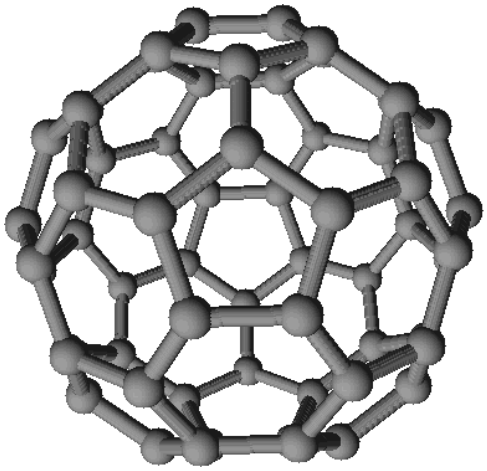

Figure 2.1. Structure of C_{60}.

The solubility of C_{60} in organic solvents, which play an important role in C_{60} extraction and purification, has been widely studied since the beginning of mass production of solid C_{60} in 1990. To date, over 150 solubility values have been reported (Hirsch and Brettreich, 2005; Kulkarni and Jafvert, 2008). Unlike other solids with temperature-dependent solubilities, C_{60} exhibits the maximum solubility in hexane, toluene and CS_2 at ca. 280 K (Ruoff et al., 1993b). Although many scientists have attempted to model and predict C_{60} solubility (Hansen and Smith, 2004; Heymann, 1996b; Kulkarni and Jafvert, 2008; Marcus et al., 2001; Ruoff et al., 1993a; Sivaraman et al., 1992), no direct dependence on certain solvent parameters has been found

(Fortner, 2006; Hirsch and Brettreich, 2005). Studies show that C_{60} solubility has strongly correlated with solvent polarizability (Ruoff et al., 1993a), molecular size (Ruoff et al., 1993a), surface area (Murray et al., 1995), molar volume (Ruoff et al., 1993b) and electron-donor capacity (Talukdar et al., 1997). The solubility of C_{60} in typical solvents is summarized in Table 2.1.

Table 2.1. C_{60} solubility in several commonly used organic solvents at 25 ^{o}C.

Solvent	Solubility (mg/L)
Acetone	1 [b]
Acetonitrile	0.04 [a]
Benzene	1,700 [b]
Carbon disulfide	7,900 [b]
Cyclohexane	36 [b]
Ethanol	1.4 [a]
Methanol	0.027 [a]
n-decane	71 [b]
Octanol	42.9 [a]
THF*	11 [a]
Toluene	3,000 [a]
Water	1.3×10^{-14} [c]

[a] from Kulkarni and Jafvert (Kulkarni and Jafvert, 2008)
[b] from Ruoff et al. (Ruoff et al., 1993a)
[c] from Heymann (Heymann, 1996a)
* Argument of solvated crystal exists

Due to the spherical shape, small size and capability of generating singlet oxygen under light irradiation, C_{60} holds high potential to benefit biological and medical applications. However, the extremely low solubility (e.g., 1.3×10^{-14} mg/L) of solid C_{60} in water (Heymann, 1996b; Ruoff et al., 1993a) largely hinders its application in these two fields. Hence, the dissolution or solubilization of C_{60} in water has attracted great attention in scientific community. Generally, there are three ways to disperse C_{60} in water: (1) modify C_{60} chemically with hydrophilic groups (Arrais and Diana, 2003; Chiang et al., 1994; Dugan et al., 1997; Lamparth and Hirsch, 1994; Sawada et al., 2003; Yamago et al., 1995), (2) disperse C_{60} with the help of water-soluble surfactants (Bensasson et al., 1994; Guldi et al., 1994), polymers (Ungurenasu and Airinei, 2000; Yamakoshi et al., 1994), natural macromolecules (Andersson et al., 1992; Guldi et al., 1994; Litvinova et al., 2001) and humic substances (Terashima and Nagao, 2007), (3) form stable colloidal aggregates (Andrievsky et al., 1999; Andrievsky et al., 1995; Cheng et al., 2004; Deguchi et al., 2001; Fortner et al., 2005; McHedlov-Petrossyan et al., 1997; Scrivens et al., 1994; Terashima and Nagao, 2007). Unlike the first two methods, the third method delivers C_{60} into water without any stabilizer. Since the size of such aggregate is scaled up to nanometer or even micron, some properties of pristine C_{60}, such as hydrophobicity, are substantially changed (Andrievsky et al., 2002; Fortner et al., 2005). Recently, nanoscale C_{60} aggregates (termed as nC_{60}) have been proposed as the most environmental relevant form of C_{60} (Fortner et al., 2005; Lyon et al., 2006).

To date, several protocols have been developed to produce stable suspensions of nC_{60} in water (e.g., Deguchi et al., 2001; Fortner et al., 2005; Deguchi et al., 2006; Brant et al., 2006; Scrivens et al., 1994). Despite of various preparation methods, aqueous nC_{60} suspensions produced by all methods are typically stable for up to 18 months, confirmed by electrophoresis experiments to possess negative charges. The origin of the negative surface charge is not completely understood. Two hypotheses have been proposed; (1) molecular C_{60} is partially oxidized by water to produce amphiphilic C_{60} (Li et al., 1993); (2) C_{60} accepts electrons from water molecules (Andrievsky et al., 1995; Deguchi et al., 2001), which is supported by ^{13}C NMR data (Fortner et al., 2005).

To develop a dispersion of CNTs, two interaction forces are required to be counterbalanced: the attractive van de Waal's force between nanotubes and the wetting force between hydrophobic nanotube surface and water. Three strategies have been tested to be effectively disperse CNTs to water: ultrasonication, surface alteration through stabilizing agents (e.g., surfactant), and surface functionalization through chemical reactions. Although ultrasonication is commonly used in most dispersing methods to initially debundle solid nanotubes, it can be independently used to prepare CNT suspensions. For example, Saleh et al. (2008) prepared MWNT suspensions by solely applying sonication. As the authors observed, ultrasonication significantly broke nanotube lengths from 6.6 μm down to 1.5 μm.

In the second strategy, various surfactants or polymers, such as polyvinyl pyrrolidone, polystyrene sulfonate, sodium dodecylbenzene sulfonate (NaDDBS), sodium dodecyl sulfate, and Triton X-100 (Chen et al., 2004; Islam et al., 2003; Matarredona et al., 2003; O'Connell et al., 2001; O'Connell et al., 2002), were used to coat the nanotube surface to induce electrostatic or steric interactions (Hilding et al., 2003) between single tubes or bundles produced through either the pre-sonication or high shear flow. However, CNTs are not favorably dispersed in all surfactants. For example, poly(methyl methacrylate-co-ethyl acrylate), polyvinyl alcohol, polyethylene glycol, and polyallyl amine are observed to not successfully disperse SWNTs (Hilding et al., 2003; O'Connell et al., 2001). Islam et al. (2002) observed that the suspension with a SWNT to NaDDBS wight ratio of 1:10 and SWNT concentration of 20 mg/mL remained in dispersed state at least 3 months. Other than surfactant or polymers, natural organic matter (e.g., humic and fulvic acids) is also capable of dispersing CNTs in water (Hyung et al., 2007; Wang et al., 2008).

The third strategy to disperse CNTs in water is to covalently bond functional groups to tube surface and, in turn, impacting the interactions between the tube and water. The traditional surface functionlization is through acidic treatment with HNO_3, H_2SO_4, or the mixture, through which –COOH and –OH are bonded onto nanotubes (Hilding et al., 2003; Kuznetsova et al., 2001; Zhao et al., 2002). Zhao et al. (2002) modified the traditional acidic treatment protocol by using concentrated H_2SO_4/30% H_2O_2 and adding a sonication process after reaction and found that the functionalized SWNT suspension was stable for at least a month.

2.3. NANOPARTICLE STABILITY AND AGGREGATION

Several papers have been published to address the stability of nC_{60} under various solution conditions. The methods used to assess nC_{60} stability include the long-time settling in dark (Brant et al., 2005a; Chen and Elimelech, 2006; Deguchi et al., 2001; Fortner et al., 2005) and aggregation kinetic analysis (Chen and Elimelech, 2006; Chen and Elimelech, 2007). In absence of background electrolyte, the hydrodynamic diameter of nC_{60} will not change significantly for periods up to 6 months (Chen and Elimelech, 2006). Interestingly, if salts, such as NaCl and

$CaCl_2$, are added, precipitation can occur under certain electrolyte concentration, and is dependent upon the ionic composition. Such agglomeration in the presence of salt suggests nC_{60} stability originates from the electrostatic repulsion (Brant et al., 2005; Chen and Elimelech, 2006; Deguchi et al., 2001; Fortner et al., 2005). Due to the negatively charge on C_{60} aggregate surface, the interaction energy based on Derjaguin-Landau-Verwey-Overbeek (DLVO) theory has been used to explain the stability and aggregation behavior of nC_{60} as a function of ionic strength and composition. The trend of increasing C_{60} diameter with ionic strength is consistent with well with DLVO theory, where the secondary energy minimum is suggested to be responsible for observed agglomeration behavior (Brant et al., 2005). As ionic strength increases the thickness of the electrical double layer (EDL) of an nC_{60} aggregate is compressed, allowing more aggregates to approach each other (Brant et al., 2005a; Brant et al., 2005b). In terms of ionic species, the presence of multivalent ions, such as Ca^{2+} and Mg^{2+}, stronger surface charge screening, coupled with the formation of surface complexation, largely reduces zeta potential of nC_{60}, which results in a larger aggregate size. On the other hand, Chen and Elimelech (Chen and Elimelech, 2006; Chen and Elimelech, 2007) conducted the aggregation kinetic studies based on real-time observation of nC_{60} diameter change with time. Plots of attachment efficiency (inverse stability ratio) vs. electrolyte concentration exhibited reaction-limited (repulsion dominated) and diffusion-limit (attraction dominated) regions. The nC_{60} critical coagulation concentration (CCC) was 120 mM for NaCl and 4.8 mM for $CaCl_2$. The attachment coefficients at various NaCl concentrations ranging from 0.06 to 0.35 M match the prediction from DLVO theory, if the Harmark constant is chose to be 6.7×10^{-21} J (Chen and Elimelech, 2006). Using a similar approach, nC_{60} aggregation kinetics in presence of humic acids is assessed, although the structure characteristics of nC_{60} (with humic acids) are unknown. The data for electrophoretic mobility and kinetics showed that the adsorption of humic acid to nC_{60} was very rapid and the presence of humic acid even at the concentration level of 1 mg C/L largely reduced nC_{60} aggregate growth rate. Such a reduction in aggregate growth rate was attributed to nC_{60} stabilization due to steric repulsion (Chen and Elimelech, 2006).

The aggregation behavior of suspended CNTs has been studied since 2001 through UV absorbance (Sano et al., 2001a), static light scattering (SLS) (Chen et al., 2004), photoemission (Niyogi et al., 2007), and pseudo-dynamic light scattering (Saleh et al., 2008). Sano et al. (2001) studied suspensions of acid-treated SWNT using a UV and found that the CCC was described by Schulze-Hardy rule, a simple solid sphere model with only VDW and EDL interactions, in which CCC was proportional to z^{-6}, where z was the electrolyte valency. Chen et al. (2004) employed multi-angle SLS to investigate the aggregation status of pristine SWNTs in Triton X-100 and acid-treated SWNTs in water or Triton X-100 and found those aggregates were fractal-like. When pristine SWNTs were well dispersed in 1% sodium dodecylsulfate, Niyogi et al. (2007) observed light emission of individual nanotubes and found that salts were able to control the aggregation status, reflected by emission intensity pattern. The aggregation behavior of pristine CNTs in suspension was further studied by Saleh et al. (2008) using a SLS instrument at only one angle. Saleh and co-authors found that the plot of attachment efficiency (α) vs. electrolyte concentration exhibited slow and fast aggregation kinetic regions, similar to those of nC_{60} system. The authors pointed out that this feature of MWNT aggregation behaviors with electrolyte concentration indicated that the MWNT suspension was stabilized by DLVO type (electrostatic) interactions. With addition of SRHA to the suspension, lower attachment efficiencies were obtained and such a stability enhancement was attributed to steric repulsions.

DLVO theory is commonly used to predict the stability of colloids by estimating the interactions between colloidal particles. The surface interaction forces between colloids mainly include VDW, EDL, Lewis acid-base and steric forces. Basically, the total interaction energy calculated in DLVO theory is the addition of the contributions from VDW and EDL forces, while in the extended DLVO theory acid-base and steric interactions are also considered.

The VDW interactions are apolar, electrodynamic interactions resulting from randomly oriented dipole-dipole interactions, randomly oriented dipole-induced dipole interactions, and fluctuating dipole-induced dipole interactions. In most cases VDW interactions between two colloid particles immersed in water are attractive. The magnitude of VDW forces depends on the separation distance between particles, the size of the particles, and the Hamaker constant. Hamaker constant is a material parameter and originated from van der Waal's potential integeral over two spheres. In addition, VDW forces are long-range forces and can be effective at large separation distances (e.g., greater than 10 nm). However, at separations greater than ca. 10 nm in free space, retardation effects, largely due to the finite time of propagation (Gregory, 1981), come into play and need to be considered. For nC_{60} aggregates, the VDW interaction energy can be calculated as follows (Gregory, 1981):

$$E_V = -\frac{Ar}{12d}[1-\frac{bd}{\gamma}\ln(1+\frac{\gamma}{bd})] \tag{2.1}$$

where A is the Hamaker constant and 6.7×10^{-21} J (Chen and Elimelech, 2006) is used for nC_{60}, b is a constant with the value of 5.32, r is the nanoparticle radius, d is the surface to surface distance and γ is the characteristic wavelength of the interaction, assumed to be 100 nm (Schenkel and Kitchener, 1960).

The EDL interactions are Coulombic interactions between charged entities, and can be repulsive or attractive, depending upon the sign and value of particle surface potential. The magnitude of EDL forces is a function of the separation distance, the diameter of particles, the surface potential of particles, electrolyte concentration, and counterion valance. The surface potential is situated at the precise particle-liquid interface and is not directly measurable, but can be derived from the zeta potential, which is measured at the slipping plane by electrokinetic methods such as electrophoresis. For rigid particles, the surface potential is often approximated as the zeta potential by converting electrophoretic mobility (μ_e) using the Henry's equation (Deshiikan and Papadopoulos, 1998):

$$\mu_e = \frac{2\varepsilon\xi f(\kappa r)}{3\mu} \tag{2.2}$$

where ε is the dielectric constant, ξ is the zeta potential, $f(\kappa r)$ is the Henry's function, μ is the dynamic viscosity, and κ is Debye parameter. The Debeye parameter is defined as:

$$\kappa^2 = \frac{F^2\sum_i c_i z_i^2}{\varepsilon RT} \tag{2.3}$$

where F is the Faraday constant, c in the molar concentration, z is the valence of the ion, and R is the ideal gas constant. The Henry's function can be expressed as (Deshiikan and Papadopoulos, 1998):

$$f(\kappa r) = 1.000 \qquad (\kappa r \leq 0.1) \quad (2.4)$$

$$f(\kappa r) = 1.0275157930 + 0.0857619670\log(\kappa r) + 0.1058385007(\log(\kappa r))^2 + 0.0464011331(\log(\kappa r))^3 \qquad (0.1 < \kappa r \leq 3.55) \quad (2.5)$$

$$f(\kappa r) = 1.0622739775 - 0.0740929226\log(\kappa r) + 0.3832612499(\log(\kappa r))^2 - 0.1256407214(\log(\kappa r))^3 \qquad (3.55 < \kappa r \leq 35.5) \quad (2.6)$$

$$f(\kappa r) = 0.7682190386 + 0.6988704751\log(\kappa r) \; 0.2263212573(\log(\kappa r))^2 + 0.0248691121(\log(\kappa r))^3 \qquad (35.5 < \kappa r \leq 1000) \quad (2.7)$$

$$f(\kappa r) = 1.500 \qquad (\kappa a > 1000) \quad (2.8)$$

Once the value of the zeta potential is computed, the EDL interaction energy can be calculated from the equation of Gregory (Gregory, 1975):

$$E_{edl} = \frac{64\pi nkTr}{\kappa^2}\tanh^2\left(\frac{ze\zeta}{4kT}\right)\exp(-\kappa d) \qquad (2.9)$$

where n is the number of cations, k is Boltzmann constant, T is the absolute temperature, z is the charge number, and e is the electron charge. In contrast to the VDW interactions, which are generally not affected by solution ionic strength, the EDLs are strongly dependent upon ionic strength and composition. For example, an increase in ionic strength strongly reduces the zeta potential, and thereby the double layer interaction energy.

2.4. CLEAN-BED FILTRATION THEORY

Two basic conceptual approaches have been employed to describe particle filtration, based on a mass balance approach and trajectory theory. In the former, mass balance calculations are used to describe particle removal by an isolated sphere or collector, with the inherent assumption that a packed bed or porous medium consists of a collection of spherical particles. Yao et al. (1971) presented the following steady-state mass balance filtration equation:

$$\frac{C}{C_0} = \exp\left[-\frac{3}{2}\frac{(1-\theta_w)}{d_c}\alpha\eta_0 L\right] \qquad (2.10)$$

where C_0 is the influent particle concentration, η_0 is the theoretical (maximum) collector efficiency, θ_w is the volumetric water content of porous media and L is the length of the bed or column. The above equation may also be expressed as a clean-bed filtration coefficient:

$$\frac{C}{C_0} = \exp(-\lambda L) \qquad (2.11)$$

where $\lambda = \frac{3}{2}\frac{(1-\theta_w)}{d_c}\alpha\eta_0$. As colloidal particles migrate through a porous medium several mechanisms may contribute to particle retention and deposition, including straining (sieving), sedimentation, diffusion, inertial impaction, and hydrodynamic forces. In most water treatment

applications, it is generally accepted that diffusion (Brownian motion) and sedimentation (gravitational settling) are the predominant mechanisms responsible for particle retention (Amirtharajah, 1988). Trajectory theory was initially developed to describe the single-collector efficiency, η_0, as a function of particle diffusion, interception and sedimentation, where $\eta_0 = \eta_D + \eta_I + \eta_G$ (Yao et al., 1971). Here, η_D, η_I and η_G are the collector efficiencies for diffusion, interception and gravity (sedimentation):

$$\eta_D = 4(\frac{Ud_c}{D_p})^{-2/3} = 4N_{P_e}^{-2/3} \qquad \eta_I = \frac{3}{2}(\frac{d_p}{d_c})^2 = 1.5N_R^2 \qquad \eta_G = \frac{(\rho_p - \rho_l)gd_p^2}{18\mu U} = N_G \quad (2.12)$$

Here, D_p is the bulk particle diffusion coefficient, d_p is the colloid particle diameter, ρ_p is the particle density, and g is the gravitational constant. To simplify the expressions, three dimensionless terms are incorporated: N_{Pe} (Peclet Number), N_R (Interception Number), and N_G (Gravitation Number). The diffusion term given above, η_D, was refined by Yao et al. (Yao et al., 1971) to account for collisions generated by diffusion, using the Happel (Happel, 1958) flow field factor, $A_s = 2(1-p^5)/(2-3p+3p^5-2p^6)$, where $p = (1-\theta_w)^{1/3}$. This model was subsequently refined by Rajagopalan and Tien (Rajagopalan and Tien, 1976) so that all terms represent fluid flows in concentric spherical space surrounding the collector particles.

$$\eta_0 = 4A_s^{1/3}N_{P_e}^{-2/3} + A_s N_{L_o}^{1/8} N_R^{15/8} + 0.00338 A_s N_G^{6/5} N_R^{-2/5} \quad (2.13)$$

where N_{Lo} represents the contribution of van der Waals attractive forces to particle removal and is defined as $N_{Lo} = 4A/9\pi d_p U$. As noted by Logan et al. (Logan et al., 1995) this form of the trajectory theory equation is consistent with the mass balance filtration equation presented above. Using the typical values, 1.05 g/cm^3, 0.71 mm, and 0.78 cm/min for particle density, medium size, and pore-water velocity, respectively, the Rajagopalan and Tien trajectory model (corrected) predicted that the minimum theoretical collector efficiency occurs between particle diameters of 1 and 2 μm. For particles with diameters greater than 2 μm, removal efficiency increase rapidly with particle size, indicative of sedimentation and interception mechanisms. For nanoparticles (diameter < 1 μm), the theoretical collector efficiency increases with decreasing particle diameter, which results primarily from the contribution of diffusion to particle deposition.

In a one-dimensional (1-D) porous media system, such as column packed with soil, the transport of colloidal particle is dominated by advection, dispersion, attachment and possible reaction. The mass balance for such a system may be expressed as:

$$\frac{\partial(\theta_w C)}{\partial t} = -(J_H + J_{adv}) - \rho_b \frac{\partial S}{\partial t} + \sum Rx \quad (2.14)$$

where, S refers to the colloid concentration in solid phase, t is the traveling time, ρ_b is the bulk density of the packed porous media, Rx is the general term representing flux caused by reaction, and J_H and J_{adv} are the fluxes due to hydrodynamic dispersion and advection, respectively. Assuming conditions of homogeneity, laminar flow, and negligible particle release or decay during the course of transport, Eq. 2.14 can be written as (Tufenkji et al., 2003):

$$\frac{\partial C}{\partial t}+\frac{\rho_b}{\theta_w}\frac{\partial S}{\partial t}=D_H\frac{\partial^2 C}{\partial x^2}-v_p\frac{\partial C}{\partial x} \tag{2.15}$$

where D_H is the hydrodynamic dispersion coefficient, v_p is the pore velocity and x is the traveling distance at time t. In the conditions where blocking and ripening are not significant and the detachment process is negligible, the term $\frac{\rho_b}{\theta_w}\frac{\partial S}{\partial t}$ can be expressed as (Tufenkji et al., 2003)

$$\frac{\rho_b}{\theta_w}\frac{\partial S}{\partial t}=k_{att}C \tag{2.16}$$

where k_{att} is attachment rate and equal to λv_p. For laboratory column tests, the pulse injection is commonly used. Under such circumstance, the initial and boundary conditions are defined as:

$$C(x,0)=0$$

$$C(0,t)=\begin{cases}C_0 & 0<t\le t_0\\ 0 & t>t_0\end{cases}$$

$$\frac{\partial C(\infty,t)}{\partial x}=0$$

Where t_0 is the injection duration. The colloid concentrations in aqueous and solid phases can be analytically solved as (Tufenkji et al., 2003)

$$C(x,t)=\begin{cases}C_A(x,t)=\frac{C_0}{2}[\exp(\frac{v_p-\sqrt{v_p^2+4k_{att}D_H}}{2D_H})erfc(\frac{v_p-\sqrt{v_p^2+4k_{att}D_H}}{2\sqrt{D_Ht}})+ \\ \qquad \exp(\frac{v_p+\sqrt{v_p^2+4k_{att}D_H}}{2D_H})erfc(\frac{v_p+\sqrt{v_p^2+4k_{att}D_H}}{2\sqrt{D_Ht}})] & 0<t\le t_0\\ C_A(x,t)-C_A(x,t-t_0) & t>t_0\end{cases} \tag{2.17}$$

$$S(x,t)=\frac{\theta_w}{\rho_b}k_{att}\int_0^t C(x,t)dt \tag{2.18}$$

For the even simpler case, where the filtration process reaches steady-state and the hydrodynamic dispersion is not significant, the solutions for colloid concentrations in aqueous and solid phases are:

$$S(x)=\frac{t_0\theta_w k_{att}C_0}{\rho_b}\exp(-\frac{k_{att}}{v}x) \tag{2.19}$$

which predicts a symmetrical effluent breakthrough curve (BTC) and exponentially-decaying retention profile for retained particles with distance.

The mathematical equations and underlying theories described above provide a framework from which to interpret and predict the transport of manufactured nanoparticles in water-saturated porous media. In practice, the basic principles developed for the removal of naturally occurring colloidal particles from drinking water have been extended to nanoparticles without modification or rigorous validation (Cheng et al., 2005; Espinasse et al., 2007; Jaisi et al., 2008; Lecoanet and Wiesner, 2004; Lecoanet et al., 2004). While this is a reasonable first approach, almost no research has been undertaken to critically evaluate the applicability of clean-bed filtration theory to nanoparticle transport and retention. For example, no directly measured nanoparticle retention data have been reported to date.

2.5. TRANSPORT OF CARBON-BASED NANOPARTICLES IN POROUS MEDIA

The transport and filtration of colloidal particles, including latex microspheres, have been extensively studied. As noted above, it may not be appropriate to directly apply the theories developed for colloid to nanoparticles since the retention behavior of particles may dramatically change when the sizes are in nanometer scale. To date, only a limited number of studies have been conducted to study the transport of fullerene nanoparticles in water-saturated porous media (Brant et al., 2005; Cheng et al., 2005; Espinasse et al., 2007; Jaisi et al., 2008; Lecoanet and Wiesner, 2004; Lecoanet et al., 2004). The transport experiments for nC_{60} aggregates have been conducted in either 40-50 mesh glass beads (GB) or a natural soil. The resulting steady-state effluent concentration data were interpreted using clean-bed filtration theory (Yao et al., 1971), where the attachment efficiency factor (α) was calculated from the plateau value of C/C_0 using Eq. 2.10. For an nC_{60} suspension (168-nm dia., C_0 = 10 mg/L) delivered at pore-water velocities (v_p) of ca. 82 and 273 m/d, Lecoanet et al. (2004) obtained steady-state relative effluent concentrations (C/C_0) of 0.56 at an ionic strength of 10 mM NaCl. A value of 0.3 for α was obtained using Eq. 2.10, while a bed length (L) of 10 cm was estimated to achieve a 3-log reduction (99.9% removal) in the influent concentration. At the higher flow rate (v_p = 273 m/d) an unusual drop in effluent concentration was observed after introducing ca. 1.75 pore volumes (PV) of nC_{60} solution, which was attributed to an "affinity transition" that yielded enhanced particle retention (Lecoanet and Wiesner, 2004). However, the flow rate employed in these experiments yields a Reynolds number (Re) of 0.53 ($\mathrm{Re} = \rho_l U d_c / \mu$, where ρ_l is the liquid density, U is the Darcy velocity, and d_c is the mean diameter of sand grain diameter or collector particle), which approaches the limit of laminar flow in porous media (Re < 1-10) (Freeze and Cherry, 1979). Following a similar analytical approach (Eq. 2.10), Espinasse et al. (2007) evaluated the effects of organic macromolecules (tannic acid at 1 mg/L and alginate at 2 mg/L), electrolyte composition ($CaCl_2$ and $MgCl_2$ at 0.01 M; $NaNO_3$ and Na_2SO_4 at 0.01 and 0.1 M; and NaCl at various concentration ranging from 0.01 to 0.6 M), and nC_{60} preparation methods (the benzene-serial dilution and THF methods). The comparison of various α values revealed that transport of nC_{60} was enhanced at low ionic strengths and in the presence of tannic acid, and reduced in the presence of Ca^{2+}, Mg^{2+} and alginate. In addition, the transport of nC_{60} prepared by these two methods differed significantly.

Cheng et al. (2005) conducted the nC_{60} transport experiments in Lula soil, rather than clean glass beads. Using a similar analytical approach (Eq. 2.10), the authors obtained the values of α ranging from 0.005 to 0.01 for an nC_{60} suspension (100 nm dia., C_0 = 48 mg/L) conditioned with 10 mM NaCl and 10 mM NaN_3 applied at pore-water velocities ranging from 0.86 to 28.3 m/d. Based on Eq. 2.10, bed lengths of 31 to 132 cm would be required to achieve 99.9% of nC_{60} removal. At the lowest flow rate (v_p = 0.86 m/d), Cheng et al. (2005) noted that the attachment

efficiency factor approached unity (i.e., all collision result in attachment) after 57 pore volumes of continuous injection, which was attributed to "filter ripening".

Lecoanet and Wiesner (2004) also conducted transport experiments for surfactant modified SWNT (4.5 or 10 mg/L, average length 130 nm and mean diameter 21 nm by DLS) in glass beads at two pore water velocities, ca. 82 and 273 m/d. At the slower flow rate, a bed length (L) of 10 m (Lecoanet et al., 2004) was estimated to achieve a 3-log reduction (99.9% removal) in the influent concentration using Eq. 2.10. At the higher flow rate, a dip was observed in SWNT BTC between 1 and 2 pore volumes, which was attributed to filter ripening. In a recent study, Jaisi et al. (2008) conducted column experiments to investigate effects of electrolyte composition (K^+ and Ca^{2+}) and concentration (0.1 to 55 mM for K^+ and 1 mM for Ca^{2+}) on transport of SWNT in water-saturated quartz sands. The SWNTs (87 mg/L) were functionalized with carboxyl groups and dispersed into water by ultrasonication. Based on the steady-state relative effluent concentrations (C/C_0), α was then calculated by normalizing the obtained attachment rate (k_{att}) to that under favorable condition, where α was equal to 1. Jaisi and co-authors (2008) found that α increased with ionic strength, indicating the retention of SWNT followed clean-bed filtration model (physicochemical filtration). Additionally, the authors observed SWNT retention at very low ionic strength (e.g., DI water) and concluded straining was another contributor to the SWNT retention. However, retention profile data were not reported for any of the nanoparticle transport experiments conducted to date.

An important feature of subsurface aquatic system is the ubiquitous presence of natural organic matter (NOM). Thus, effects of NOM must be considered in order to mimic the real nC_{60} transport conditions. As stated above, the presence of NOM is capable to increase the stability of nC_{60} and its potential to enhance the mobility of nC_{60} in porous media has been proposed. However, the direct observation of enhanced mobility has not been reported. The effect of NOM on the transport of colloidal hematite (Amirbahman and Olson, 1993; Kretzschmar and Sticher, 1997), latex microspheres (Amirbahman and Olson, 1995; Davis et al., 2002; Franchi and O'Melia, 2003), and bacteria (Johnson and Logan, 1996) have been studied. In general, adsorption of NOM onto particles increases the negative surface charge. For positively charged microspheres, 1 mg C/L of NOM was sufficient to reverse the surface charge. Dynamic light scattering (DLS) measurements revealed that the thickness of adsorbed NOM layer was less than 10% of particle radius (Amirbahman and Olson, 1995; Franchi and O'Melia, 2003). Promotion of colloidal particle transport qualitatively agrees with the increase of electrostatic repulsion. Franchi and O'Melia (2003) conducted batch sorption and column experiments to investigate the deposition of sulfate latex microspheres (98 nm) to spherical soda-lime GB under various ionic strengths (NaCl) in the presence of 1 mg C/L of humic acid. Based on DLVO calculations, the authors concluded that, at lower ionic strength (<10 mM), secondary minimum controlled attachment process, while at higher ionic strength, both first and secondary minima contributed to microsphere retention. In the presence of Ca^{2+} at 10 mM, electrophoretic mobilities of microspheres were not dependent on humic acid concentration (Davis et al., 2000). Thus, the enhancement of microsphere transport in presence of both Ca^{2+} and humic acid was attributed to steric repulsion induced by Ca^{2+}.

2.6. PARTICLE RETENTION IN POROUS MEDIA

The retention mechanisms of colloidal particles in porous media have been extensively studied due to the need for controlling or predicting colloid movement in subsurface and water treatment filtration systems. Clean-bed filtration theory has been successfully applied to

interpret particle retention data obtained from laboratory and field experiments (Harvey and Garabedian, 1991; Yao et al., 1971). However, recent column studies have shown that the clean-bed filtration theory is not adequate when a repulsive DLVO energy barrier exists (Bradford et al., 2002; Bradford et al., 2003; Bradford et al., 2009; Li et al., 2004; Tufenkji et al., 2003). Under these conditions, the retention profiles of negatively-charged latex microspheres and certain bacteria deviate from the predictions based on clean-bed filtration theory, yielding a distinct hypo-exponential or non-monotonic profile (Figure 2.2), even though the measured effluent data were fit very well. Subsequent studies of such deviations have revealed that the retention of particles in unfavorable conditions (i.e., presence of repulsive DLVO energy barrier) is governed by hydrodynamic forces (e.g., drag) (Bergendahl and Grasso, 2000; Li et al., 2005), and physical straining (Bradford et al., 2006), in addition physicochemical interactions (e.g., DLVO theory). Compared to colloidal particles (e.g., latex microspheres), almost all fullerene nanoparticles (e.g., nC_{60} and MWNTs) that are capable of forming stable suspensions in water possess a net negative surface charge (Fortner et al., 2005; Saleh et al., 2008), indicating the retention of fullerene nanoparticles will occur under unfavorable conditions. It has also been reported that physicochemical interactions and straining contribute to nanoparticle retention in water-saturated porous media (Brant et al., 2005; Jaisi et al., 2008).

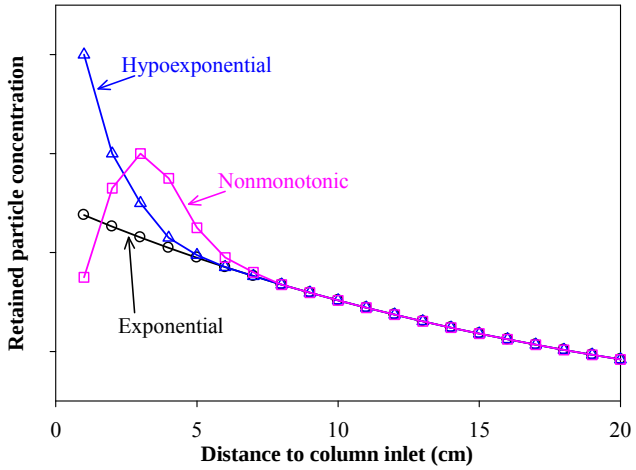

Figure 2.2. Schematic retention profiles of colloidal particles in porous media under unfavorable conditions.

Physicochemical interactions, such as VDW and EDL interactions, are assumed as the primary mechanism for colloidal particle retention in the clean-bed filtration model (Bradford et al., 2009). DLVO theory is commonly used to calculate the interactions between colloidal particles and soil grains, where the particle-solid system is treated as the sphere-plate model (Tufenkji and Elimelech, 2004). Similar to particle-particle systems, the total interaction energy in particle-solid system includes attractive VDW and repulsive EDL interactions. For VDW interaction energy, Lecoanet and Wiesner (2004) calculated the first Hamaker constant for the fullerene-silica-water system to be 2.76×10^{-20} J. Chen and Elimelech (2006) adopted equations from Gregory (1981) for VDW and Gregory (1975) for EDL calculations to describe the deposition of nC_{60} onto silica surface. However, Guzman et al. (2006) realized that the classical DLVO calculations were based on Derjaguin approximation, which was not valid for nanoparticles. These authors proposed the use of a surface element integration technique to avoid the assumptions in Derjaguin approximation.

A typical DLVO interaction energy profile for a nanoparticle-water-solid system under unfavorable conditions consists of an energy barrier, the first energy minimum, and the second energy minimum, as illustrated in Figure 2.3. Transport experiments have revealed that colloidal particles may be retained on solid surfaces by the second energy minimum or the first energy minimum, bypassing the energy barrier (Tufenkji and Elimelech, 2004). The retention of particles by the second energy minimum is considered to be reversible, whereas particles held by the first energy minimum are essentially irreversible, and may not detach even when the ionic strength decreases. Although limitations to DLVO theory have been recognized, many studies have demonstrated that the second energy minimum plays an important role on the retention of colloids at nanometer scale (e.g., 50-200 nm latex microspheres) in water-saturated porous media. For example, Litton and Olson (1996) conducted microsphere (248 nm) detachment experiments and observed that 80% of retained particles were released when the column was flushed with an anionic surfactant (e.g., sodium dodecyl sulfate) solution, which provided evidence for particle retention in the second energy minimum. Hahn et al. (2004) conducted experiments to investigate retention and release of sub-micron size colloids (e.g., 72 nm latex and 80 nm hematite), and observed detachment when the ionic strength was decreased. A related study conducted by Pelley and Tufenkji (2008) reported an increase in particle attachment kinetics with particle size (50 - 1,500 nm). The authors concluded that larger particles (e.g., 1,500 nm) were held by the second energy minimum, while both the first and second energy minimum contributed to the retention of the smallest particles (50 nm). Although the second energy minimum has not been correlated to the retention of nC_{60} in porous media, the detachment experiments conducted by Jaisi et al. (2008) indicated that the second energy minimum contributed to the retention of SWNT in quartz sands.

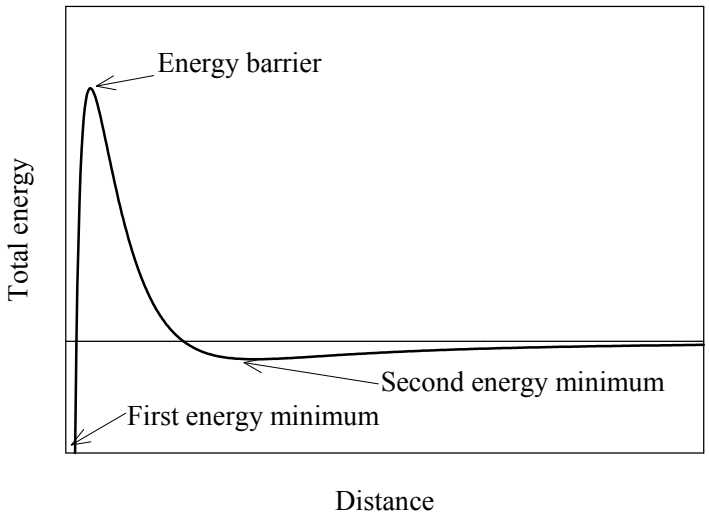

Figure 2.3. A typical DLVO interaction energy profile of colloids in porous media

Physical straining can an important mechanism contributing to particle retention in porous media, which is not accounted for by clean-bed filtration theory (Bradford et al., 2007). Straining is a result of pore geometry, and is defined as the retention of suspended particles in

pore throats and the smallest regions that are too small to permit particle passage (Bradford et al., 2006). Herzig et al. (1970) performed geometrical (triangular constriction) calculations and found physical straining would contribute significantly to particle retention when the particle-grain diameter ratio is less than 0.05. Xu et al. (2006) reported a critical particle-grain diameter ratio of 0.008, while Bradford et al. (2002) observed microsphere retention due to physical straining at a particle-grain diameter ratio of 0.002. A recent study by Shen et al. (2008) observed that the retention due to straining occurred at a particle/grain diameter ratio of 0.0016, when a suspension of 1,156 nm diameter colloids was introduced into a column packed with 0.72 mm glass beads. Although the study on CNT transport (Jaisi et al., 2008) has revealed that physical straining can contributes to nanotube retention due to the large aspect ratio, the contribution of straining to nC_{60} retention has not reported. If 0.0016 is the smallest critical particle-grain diameter ratio, a mean diameter of 410 nm would be required for nC_{60} to allow physical straining to significantly contribute to nC_{60} retention in 40-50 mesh (mean diameter 256 μm) quartz sands. However, several studies suggest that particle straining is dependent upon solution chemistry (Bradford et al., 2007; Shen et al., 2008) and particle concentration.

CHAPTER 3

MATERIALS AND METHODS

The following tex describes the materials and methods used during the completion of this project. The sections are organized by experiment type given that there were slight variations in procedures and analytical protocols between individual experiments.

3.1. MATERIALS

3.1.1. CHEMICALS

Solid C_{60} (99.9%; purified by sublimation) was purchased from the Materials Electronics Research Corp. (Tuscon, AZ) to prepare nC_{60} suspensions. Multi-wall carbon nanobutes (MWNT) at three different lengths, 0.5-2, 10-20, and 50 μm, were purchased from Cheap Tubes Inc. (Brattleboro, VT), Iljin Nanotech Co. (Seoul, Korea), and BuckyUSA (Houston, TX), respectively. The selected properties of MWNT are listed in Table 3.1. THF (99.99%+) was purchased from Fisher Scientific (Fair Lawn, NJ) and used as vehicle solvent during nC_{60} preparation. Optima grade methanol and toluene were obtained from Fisher Scientific for nC_{60} quantification using high performance liquid chromatography (HPLC). Various chemicals, such as calcium chloride, sodium chloride, sodium hydroxide, sodium phosphate monobasic, and calcium bromide, certified ACS or higher grade, were purchased from Sigma-Aldrich (St. Louis, MO). These chemicals were used to obtain specific solution conditions, in addition to being used as non-reactive tracers. Magnesium perchlorate (ACS reagent grade) was purchased from MP Biomedicals, Inc. (Solon, OH) as a destabilizing agent in nC_{60} extraction by toluene. A nonionic surfactant, polyoxyethylene (20) sorbitan monooleate (Tween 80), was purchased from Uniqema (New Castle, DE), as a representative stabilizing agent. Tween 80 was selected due to its relatively low toxicity (Pennell et al., 1993) and wide application in surfactant enhanced aquifer remediation (Pennell et al., 1997; Ramsburg and Pennell, 2001). Tween 80 has an average molecular weight of 1,310 g/mol and the critical micelle concentration (CMC) that is estimated to be 13 mg/L (Pennell et al., 1993; Pennell et al., 1997). The chemical structure of Tween 80 is provided in Figure 3.1. For representative natural stabilizing agents, Suwannee river humic acid (SRHA; standard II) and Suwannee river fulvic acid (SRFA; standard II) were obtained from the International Humic Substances Society (St. Paul, MN). Relevant physical and chemical properties of SRFA and SRHA are summarized in Table 3.2.

Table 3.1. Selected properties of MWNT.

Manufacture	Length (μm)	Purity (wt%)	Inside Diameter (nm)	Outside Diameter (nm)	Other elements
Cheaptubes	0.5-2	>95	5--10	10--20	Cl
Cheaptubes	10-20	>97		10--20	
BuckyUSA	50	95	3--5	8--15	Al, Cl, S

Data provided by manufactures.

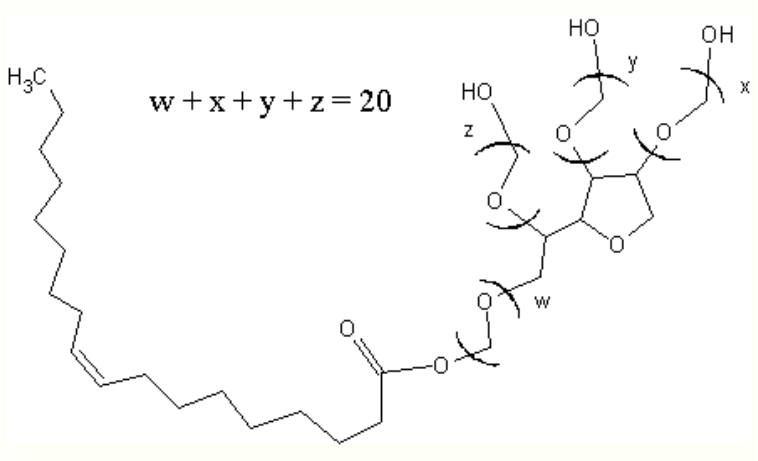

Figure 3.1. Structure of Tween 80.

Table 3.2. Selected properties of Suwannee River humic acid (SRHA) and fulvic acid (SRFA).

Items	SRHA	SRFA
Mw (Da)	1,000-5,000[a]	2,310[b]
Mn (Da)		1,360[b]
C	52.63	52.34
H	4.28	4.36
O	42.04	42.98
N	1.17	0.67
S	0.54	0.46
P	0.013	0.004
carboxylic acidity (meq/g)	4.8	6.6
Carboxyl	15	17
Aromatic	31	22
Acetal	7	6
Heteroaliphatic	13	16
Aliphatic	29	35

[a] from Hong and Elimelech (1997)
[b] from Chin et al. (1994)
Remaining values from International Humic Substances Society (IHSS) (St. Paul, MN)

3.1.2. POROUS MEDIA

In this project four solid phases, glass beads (GB), Ottawa sands (OS), Appling soil and Webster soil, were utilized as porous media. Soda lime glass beads were purchased from International Surface Preparation (Bellaire, TX) and only the size fraction retained between 40 and 50 mesh sieves was used. This material was selected to allow for direct comparison with previous nC_{60} transport studies (Brant et al., 2005; Espinasse et al., 2007; Lecoanet and Wiesner, 2004; Lecoanet et al., 2004). Two size fraction of Ottawa sand (F-42 and F-70) were obtained

from U.S. Silica (Berkeley Springs, WV), and were sieved to obtain four additional size fractions, 20-30, 40-50, 80-100, and 100-140 mesh. Appling soil was collected from the Ap1 and Ap2 horizons (upper 30 cm of the soil profile) at the University of Georgia Agricultural Experiment Station located near Eastville, GA. The soil is classified as a loamy, coarse sand of the Appling series (clayey, kaolinitic, thermic Typic Hapludult). Appling soil consists of approximately 77% sand, 14% silt and 9% clay. Webster soil, a silty clay loam (mixed, mesic Typic Haplaquoll), was collected from upper 30 cm of the soil horizon at the Agricultural Experiment Station located in Ames, IA. The particle size distribution of Webster soil is approximately 23% sand, 44% silt and 33% clay. Selected properties of soils are given in Table 3.3. Prior to use, the glass beads were washed with pure acetone and hexane solution sequentially, and then soaked in concentrated (12.1 M) hydrochloric acid (HCl) for 12 h. The glass beads were rinsed several times with de-ionized (DI) water (>18.0 MΩ·cm, Nanopure Model D4741, Barnstead International, Dubuque, IA) to remove residual HCl, and placed in a series of ultrasonic baths containing 0.01 M sodium hydroxide (NaOH), DI water, and 1.0 M nitric acid (HNO_3), each for 20 minutes at room temperature (ca. 23 ^oC). The glass beads were rinsed with DI water until pH 7 was achieved, and then oven-dried at 70 ^oC for 12 h. Each Ottawa sand size fraction was soaked in a 1.0 M HNO_3 solution, rinsed with DI water, and placed in an ultrasonic bath containing 0.007 M Na_2HPO_4 for at least 10 h, rinsed with DI water until pH 7 was reached, and finally oven-dried at 200 ^oC for 12 h. Air-dried Appling and Webster soils were grounded to pass 10-mesh sieve and packed into the column without any additional pretreatment.

Table 3.3. Selected properties of Appling and Webster soil.

Soil name	Specific surface area (m^2/g)	Organic carbon content (%wt)	Cation exchange capacity (cmol/kg)	Intrinsic permeability (m^2)
Appling soil	3.50	0.75	7.1	1.2×10^{-11}
Webster soil	8.2	3.32	49.4	NA

Values obtained from Karagunduz et al. (2001) and Pennell et al. (1995)
NA = not available

3.2. EXPERIMENTAL PROTOCOLS

3.2.1. PREPARATION OF nC60 SUSPENSIONS

Stable aqueous suspensions of nC_{60} were prepared following previously described procedures (Deguchi et al., 2001; Fortner et al., 2005). At room temperature, THF was saturated with excess C_{60} powder after sparging with N_2 to remove dissolved oxygen. Upon saturation, the supernatant was filtered by vacuum through a 0.22 μm nylon membrane (Osmotics Corp., Minnetonka, MN), sparged with N_2 gas, and stored in a 4L amber glass container. An equal volume (250 mL) of DI water was added to a stirred C_{60}-THF solution at a rate of 1 L/min. The resulting solution (500 mL) was loaded into a rotary evaporator (Rotovapor Model R210, Buchi, New Castle, DE) and heated at 75 ^oC until ca. 200 mL of solution remains. The residual solution was diluted with 100 mL of DI water, and the evaporation process was repeated three times to remove THF. The resulting aqueous C_{60} suspension (ca. 250 mL) will be vacuum-filtered through a 0.22 μm cellulose acetate membrane (Corning Inc., Corning, NY) and stored at 4 ^oC in the dark for subsequent use as the nC_{60} stock suspension.

Influent nC_{60} suspensions for the column transport studies were prepared in degassed DI water to which appropriate amounts of background electrolyte, Tween 80, SRHA, or SRFA stock solutions and nC_{60} stock suspension were added to achieve the desired final concentrations. The background electrolyte stock solution consisted of 0.5 M $CaCl_2$ or 0.1 M NaCl and 0.01 M $NaHCO_3$. The stock solutions of SRHA and SRFA were prepared by dissolving 41.5 mg of SRHA powder and 44.3 mg of SRFA powder, respectively, into 100 mL DI water. After mixing for 24 hrs, both solutions were adjusted to pH 7.0 with 0.1 M NaOH and filtered through a 0.22 μm cellulose acetate membrane.

In the absence of Tween 80, SRHA or SRFA, influent nC_{60} suspensions were prepared by adding 100 mL nC_{60} stock suspension to an equal volume of background electrolyte solution (degassed; with various electrolyte species and concentrations) at a mixing rate of 120 mL/min. To examine potential effects of the suspension preparation method on nC_{60} particle size and stability, additional aqueous nC_{60} suspensions were prepared following the general procedures described above. Several preparation variables were considered, including three electrolyte concentrations (1, 10, 100 mM NaCl or $CaCl_2$), two addition rates (24 and 120 ml/min), two mixing sequences (addition of nC_{60} stock suspension to the electrolyte solution, referred to as E1S2, and addition of the electrolyte solution to the nC_{60} stock suspension, referred to as S1E2), and two final concentrations (~1 and 3 mg/L). For influent nC_{60} suspensions prepared with either Tween 80, SRHA or SRFA, the nC_{60} stock suspension was first mixed with either Tween 80, SRHA or SRFA stock solution in a 200 mL volumetric flask. A predetermined volume of the background electrolyte stock solution (0.5 M $CaCl_2$ and 0.01 M $NaHCO_3$) was introduced to the mixture, and degassed DI water was then added to achieve the desired final concentration of Tween 80, SRHA or SRFA (1,000 mg/L, 20 mg C/L, and 20 mg C/L, respectively) in 1×10^{-3} M $CaCl_2$ and 5×10^{-5} M $NaHCO_3$. At a bicarbonate concentration of 5×10^{-5} M, the pH of nC_{60} influent suspensions before and after the injection period, as well as selected effluent samples, was measured and found to be approximately 7.0. All aqueous nC_{60} suspensions were used within 1 hour of preparation.

3.2.2. Preparation of MWCNT Suspensions

The protocol employed herein to functionalize MWNT by 4-ethoxybenzoic acid (4-EBAc) are described in detail by Lee et al. (2008). Briefly, 4-ABAc (3.65 mM), MWNT, polyphosphoric acid and Phosphorus Pentoxide (P_2O_5) were mixed in a flask at a weight ratio of 1:1:40:10 under the nitrogen atmosphere. The flask was heated sequentially to 80, 100, and 130 ^oC for 1, 1, and 72 h, respectively. De-ionized water was then added to the mixture to obtain the MWNT stock suspension. The resulting suspension exhibited a shiny green-brown color, which was distinct from other dispersed MWNT by sonication. Since no MWNT loss was observed, the concentration of MWNT in stock suspension was calculated based on the mass of MWNT added and the final volume. To obtain MWNT input suspensions for column experiments at the proper concentrations, such as 5 and 90 mg/L, a predetermined amount of MWNT stock suspension was diluted with DI water and the pH was adjusted to 5 using 0.1 or 1 M NaOH solution. A series of MWNT transport experiments was performed at an input concentration of 90 mg/L to allow for comparisons with a previous MWNT study (Jaisi et al., 2008).

3.2.3. Column Experiments

The column apparatus consisted of a Rainin HPLC pump (Dynamix SD-200, Varian, Inc. Palo Alto, CA) equipped with a 25 mL pump head and pulse dampener, a syringe pump (Model

22, Harvard Apparatus, Inc., Holliston, MA), a borosilicate glass column, and an ISCO fraction collector (Teledyne Isco Inc., Lincoln, NE), which is shown schematically in Figure 3-2. The column had dimensions of 2.5 cm inside diameter by 15 cm length for GB and OS studies. For the studies performed with Appling or Webster soil, the column length was shortened to 11 cm to reduce the total bed length, and thus, the volume of nanomaterial suspension that was required. The columns were packed with either GB, Ottawa sand, Appling soil, or Webster soil in 1-cm increments. For nC_{60} transport experiments, each column endplate was fitted with two 40-mesh nylon screens and a 70 μm nylon filter to support the solid phase and promote uniform flow of the aqueous phase, while a 60-mesh stainless steel screen was used for the endplate in MWNT transport experiments to reduce nanotube retention by supporting filter. Prior to water imbibition, the dry packed column was flushed with CO_2 gas for at least 20 min to facilitate dissolution of entrapped gas phase. At least 10 pore volumes (PV) of degassed background electrolyte solution were introduced into the column in an upflow mode at a pore-water (seepage) velocity of either 1 or 8 m/d. After complete saturation of the column with background electrolyte solution, a pulse (e.g., 5 PV) of nC_{60} or MWNT suspension was introduced into the column with the syringe pump, followed by the injection (e.g., 3 PV) of nanoparticle-free solution at the same flow rate. To further investigate the potential effect of sorbed-phase Tween 80 on nC_{60} transport and solid phase interactions, the experimental sequence was modified to include a Tween 80 preflood, which was conducted by injecting 5 PVs of nC_{60}-free Tween 80 solution (1,000 mg/L conditioned with 1×10^{-3} M $CaCl_2$ and 5×10^{-5} M $NaHCO_3$), followed by 3 PVs of background electrolyte solution. Upon completion of the Tween 80 injection sequence, a 5-PV pulse of either a suspension containing nC_{60} alone or a suspension containing Tween 80 mixed with nC_{60} was introduced into the Ottawa sand or Appling soil column at the same flow rate, followed by 3 PVs of background electrolyte solution. Under these flow conditions, the Reynolds number (Re) was equal or less than 0.011, which was several orders-of-magnitude below the limit of laminar flow in a packed bed (Re < 1-10).

Column effluent samples were collected continuously in 15-mL sterile plastic centrifuge tubes (Fisher Scientific, Fair Lawn, NJ). At the conclusion of each transport experiment, the column was dissected into 1.5-cm increments, which were transferred to 30-mL glass vials. The retained nC_{60} aggregates were extracted from GB, OS dissection samples by addition of 10 mL of DI water, agitated for 3 hr (Labquake, Barnstead International, Dubuque, IA), followed by ultrasonication (Model FS20H, Fisher Scientific) for 1 min. For transport experiments conducted in Appling and Webster soils, the sectioned soil samples were oven-dried at 85 ^{o}C over night prior to C_{60} extraction by toluene.

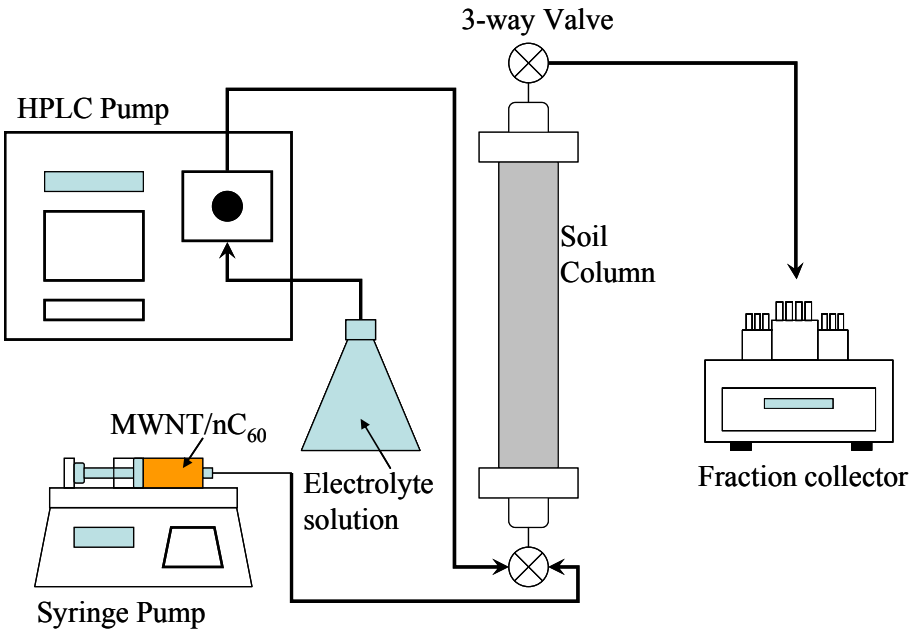

Figure 3.2. Schematic diagram of the experimental apparatus used for the nC_{60} transport and retention studies.

Following complete water saturation of the porous medium, a non-reactive tracer test was conducted in selected columns to assess water flow and hydrodynamic dispersion. Three PVs of a 1 x 10^{-3} M $CaBr_2$ and 5 x 10^{-5} M $NaHCO_3$ solution were introduced at a pore velocity of 1 or 8 m/d, followed by three PV of 1 x 10^{-3} M $CaCl_2$ and 5 x 10^{-5} M $NaHCO_3$ at the same flow rate. Effluent samples were collected continuously in centrifuge tubes using a fraction collector and bromide concentrations were measured using an ion selective bromide electrode (Cole-Parmer Instrument Co., Vernon Hills, IL) connected to an Accumet Model 50 pH meter (Fisher Scientific, Fair Lawn, NJ). The probe was calibrated using bromide standards with concentration spanning from 10 to 200 mg/L.

3.2.4. Batch Retention Experiments

Batch reactor experiments were performed in 30 mL borosilicate glass vials to independently assess the attachment characteristics of nC_{60} particles to glass beads or Ottawa sand. Approximately 13 g of dry OS or GB were combined with 13 mL of nC_{60} suspension at initial concentrations of ranging from 0.08 to 12.78 mg/L, prepared in DI water or 1.0 mM $CaCl_2$ buffered to pH 7 with 0.05 mM $NaHCO_3$. The contents of the batch reactors were mixed on an oscillating shaker for 4 h, which corresponds to approximate duration of an nC_{60} transport experiment.

3.3. ANALYTICAL METHODS

3.3.1. PARTICLE SIZE DISTRIBUTION

The mean diameter and size distribution of nC_{60} aggregates in aqueous suspension were determined using a Zetasizer Nano ZS analyzer (Malvern Instruments Ltd. Southborough, MA) operated in non-invasive back scattering (NIBS®) mode at an angle of 173º. Measurement of particle size distribution by photon correlation spectroscopy, commonly referred to as dynamic light scattering (DLS), is based on the change in scattered light intensity collected over different time intervals. These data are described using an electric field correlation function (*CF*), for which the decay rate (Γ) may be expressed as:

$$\Gamma = q^2 D_m \tag{3.1}$$

where D_m is the mutual diffusion coefficient and q is the scattering vector magnitude, defined as:

$$q = \frac{4n\pi \sin(\theta/2)}{\lambda_0} \tag{3.2}$$

where n is the refractive index of the solution, θ is the scattering angle (173°), and λ_0 is the laser wavelength (532 nm). Assuming that the particles are: (i) in Brownian motion (dilute solution), (ii) spherical in shape with a diameter that is small relative to the molecular dimensions, and that (iii) D_m is approximately equal to the diffusion coefficient extrapolated to infinite dilution (D_0), Stokes' Law can be used to calculate the effective hydrodynamic radius (r) of a particle:

$$r = \frac{k_b T}{6\pi\mu D_0} \tag{3.3}$$

where k_b is the Boltzman constant, T is the temperature in degrees Kelvin, μ is the dynamic viscosity of the solution. Approximately 1 mL of nC_{60} suspension was loaded into a disposable cuvette (DTS0012, Malvern Instruments Ltd., Southborough, MA) and analyzed using a green laser (DPSS source, 50.0mW) at 532 nm and a C_{60} refractive index of 2.20 (Huffman, 1991). A refractive index of 1.33 (water) was used for all aqueous samples. The instrument obtains scattering intensity fluctuation data to obtain a correlation function, which is converted into natural log form and fit to a polynomial function:

$$ln(CF) = a + bt + ct^2 + dt^3 + et^4 + ... \tag{3.4}$$

where the terms a, b, c, d and e are fitting parameters, with the value of b corresponding to the mutual diffusion coefficient (D_m) in eq 3.1, while eq 3.3 was used to obtain the aggregate radius. Based on a measured set of correlation functions, an intensity distribution is generated from which the mean aggregate size is obtained. All DLS measurements were performed in triplicate, and the accuracy of the system was checked using monodisperse polystyrene spheres (3100A, Nanosphere Size Standards, Duke Scientific Corp., Palo Alto, CA), with a mean diameter of 97 ± 3 nm. A typical size distribution (by intensity) of nC60 suspension is shown in Figure 3.3.

The size and shape of the nC_{60} aggregates were further characterized by transmission electron microscopy (TEM) following the procedures of Fortner et al. (Fortner et al., 2005). Briefly, two drops of concentrated (*ca.* 25 mg/L) nC_{60} suspension were placed on a 300-mesh carbon-coated copper grid (Electron Microscopy Sciences, Hatfield, PA), air-dried at room temperature, and imaged using a JEOL 100CX II transmission electron microscope (Peabody,

MA) operated at 100 kV. A representative TEM image of the nC_{60} aggregates is shown in Figure 3.4.

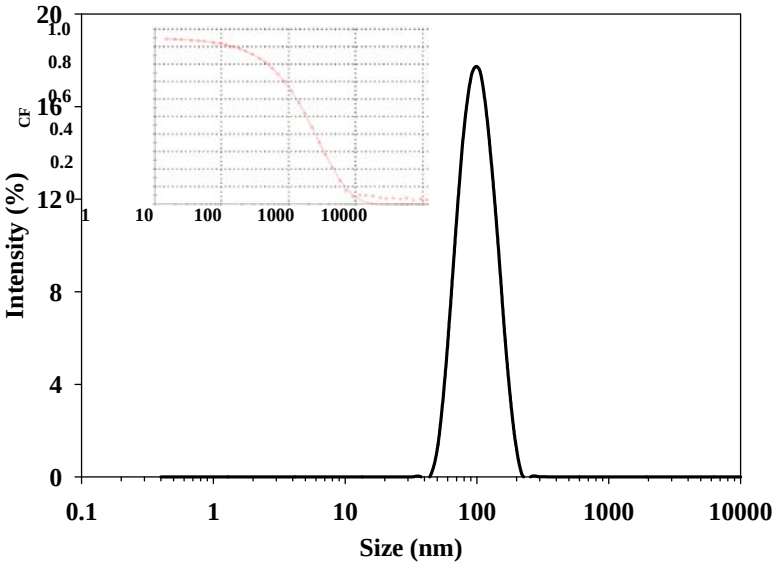

Figure 3.3. Size distribution of an nC_{60} suspension (pH 7, C_{60} concentration = 6.7 mg/L, DI water) determined by dynamic light scattering. The inset shows the corresponding correlation function (*CF*).

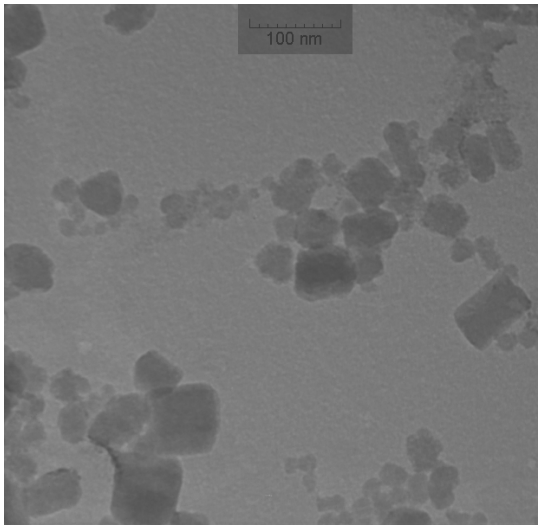

Figure 3.4. Transmission electron micrograph (TEM) image of nC_{60} aggregates dried on a 300-mesh carbon-coated copper grid.

3.3.2. ELECTROPHORETIC MOBILITY

The electrophoretic mobility of nC_{60} aggregates or MWNT in aqueous samples was determined using a Zetasizer Nano ZS analyzer. The instrument monitored the direction and velocity of particles (i.e., electrophoretic mobility) in response to an applied electric field. Particle movement was tracked using a combination of laser doppler velocimetry (LDV) and phase analysis light scattering (PALS), which enabled detection of particles with diameters ranging from 5 nm to 10 μm. For nC_{60}, the electrophoretic mobility was converted to a zeta potential using Eq. 2.8.

3.3.3. AQUEOUS PHASE CONCENTRATIONS

The aqueous phase concentration of nC_{60} in the absence of SRHA or SRFA was determined using a Cary 3E UV-Vis spectrophotometer (Varian Inc., Palo Alto, CA) scanned over wavelength range of 190 to 500 nm. The absorbance response at a wavelength of 344 ± 1 nm was used for nC_{60} quantification based on a 5-point calibration curve prepared by serial dilution of a known C_{60} stock solution (9.5 mg/L). Concentrations of nC_{60} in stock solution and samples in presence of SRHA or SRFA were determined using a liquid-liquid extraction process (Fortner et al., 2005; Xia et al., 2006). An aliquot (2 mL) of aqueous sample was destabilized with 0.8 mL of 0.1 M $Mg(ClO_4)_2$, to which 2.0 mL of neat toluene were added to extract C_{60} from the aqueous phase. The extraction vials were placed on a table shaker and mixed at 400 rpm for 10 min, followed by mixing at 250 rpm for 12 h (Innova 2100, New Brunswick Scientific Co., Inc., Edison, NJ). After mixing, the toluene phase was transferred to a 1.5 mL centrifuge tube (VWR International, West Chester, PA) and spun at 5000 rpm for 10 min (Eppendorf centrifuge 5415D, Brinkmann Instruments Inc., Westbury, NY). An aliquot (0.3 mL) of toluene was transferred into 1.2 mL methanol and the combined solution was loaded onto an high performance liquid chromatograph (HPLC) after mixing for 1 min on a vortex (Touch mixer model 232, Fisher Scientific).

Quantitative analysis of C_{60} in the toluene-methanol solution was performed using an Agilent model 1100 HPLC equipped with an Altima C18 column (150 mm length x 4.6 mm i.d., 5 um particle size) and a diode array detector (DAD) monitored at a wavelength of 334 nm. The HPLC was operated at a constant flow rate of 1 mL/min with an isocratic mobile phase consisting of 55% toluene and 45% methanol (Isaacson et al., 2007). Reference C_{60} standards were prepared by placing 2 mg of fullerene powder into an amber vial containing 10 mL of toluene, which was placed in a sonication bath for 3 hrs, and then diluted to prepare a calibration curve.

The concentration of MWNT in input suspensions and effluent samples from experiments with 90 mg/L as input concentration were determined using a Cary 3E UV-Vis spectrophotometer at 450 nm, where an absorbance shoulder was constantly observed, a Shimadzu spectrofluorometer (Shimadzu Scientific Instruments, Columbia, MD) operated with an excitation wavelength of 450 nm was used to quantify MWNT concentrations of those from experiments with 5 mg/L as input concentration. The fluorescence was scanned from 400 to 700 nm and the intensity at 515 ± 5 nm was employed herein.

To quantify the concentration of SRHA or SRFA, the aqueous phase from the extraction vial was analyzed using the Cary 3E UV-Vis spectrophotometer at a wavelength of 290 nm, where the minimum interference of magnesium perchlorate was observed. To determine the concentration of Tween 80 in the presence of nC_{60}, effluent samples was filtered through 0.02 μm membrane filter (Whatman International Ltd., Maidstone, Kent, UK) to remove nC_{60}. The

filtrate was then analyzed using the Cary 3E UV-Vis spectrophotometer operated at a wavelength of 234 nm. Quantification of Tween 80 was obtained using a 5-point calibration curve prepared over a concentration range of 10 to 1,500 mg/L.

Analysis of THF and a toxic daughter product, GBL, in aqueous samples was performed using an Agilent 6890 gas chromatograph (GC) equipped with a DB-1ms column (30 m length × 0.25 mm outside diameter × 0.25 um film thickness, J&W Scientific Inc., Folsom, CA) connected to an Agilent Model 5975 mass selective detector (MSD). Approximately 2 mL of effluent sample were treated with 2 g of NaCl before loading onto an HT3 headspace autosampler (Teledyne-Tekmar, Mason, OH) that was connected to the GC-MS system. To measure the concentration of GBL, a separate aliquot (1 mL) of aqueous samples was mixed with equal volume of methylene chloride for 30 min on an oscillating shaker. After extraction, GBL in methylene chloride was analyzed using GC-MS system. GBL standards were pretreated and analyzed using the same protocol.

3.3.4. Solid Phase Concentrations

In order to determine amount of nC_{60} retained by the Appling or Webster soil, nC_{60} was extracted from oven-dried (85 ^{o}C) dissection samples by adding 20 mL of neat toluene. The extraction vials were then placed in an ultrasonication bath for 4 hr and mixed at 250 rpm for 12 hours at 30 ^{o}C. The C_{60} concentration in toluene phase was determined using the same HPLC method described in liquid-liquid extraction above. A five-point calibration curve over a concentration range of 1 to 100 µg nC_{60} per 13 g Appling or 11 g Webster soil was prepared following similar sample drying and toluene extraction processes. The detection limit of the solid-phase extraction method was 0.35 and 0.11 µg/g for Appling and Webster soil, respectively.

3.4. Mathematical Modeling

3.4.1. Simulation of Non-Reactive Tracer Transport

The resulting non-reactive tracer BTCs were fit to a one-dimensional form of the advective-dispersive reactive (ADR) transport equation using CXTFIT ver 2.0 (Toride et al., 1999):

$$R_F \frac{\partial C^*}{\partial t^*} = \frac{1}{P_e}\frac{\partial^2 C^*}{\partial X^2} - \frac{\partial C^*}{\partial X^*} \tag{3.5}$$

$$R_F = 1 + \frac{\rho_b K_D}{\theta_w}; \quad C^* = \frac{C}{C_0}; \quad t^* = \frac{v_p t}{L}; \quad P_e = \frac{v_p L}{D_H}; \quad X^* = \frac{x}{L} \tag{3.6}$$

where R_F was the retardation factor, K_D was the solute distribution coefficient; t^* was dimensionless pore volumes, P_e was the Peclet number, and X was dimensionless distance. In the absence of physical nonequilibrium (e.g., immobile water), the value of $R_F = 1$ for a non-reactive tracer, and hence, the only parameter that was fit was the Peclet number (*Pe*), from which the hydrodynamic dispersion coefficient (D_H) was obtained.

3.4.1. SIMULATION BASED ON CLEAN BED FILTRATION THEORY

According to clean-bed filtration theory (Yao et al., 1974), the transport of colloidal particles through a water-saturated homogeneous porous medium can be described by advection, hydrodynamic dispersion, and retention (filtration) processes. A one dimensional advection-dispersion equation with first-order particle retention kinetics is typically employed to simulate particle transport:

$$\frac{\partial C}{\partial t} + \frac{\rho_b}{\theta_w}\frac{\partial S}{\partial t} = D_H \frac{\partial^2 C}{\partial x^2} - v_p \frac{\partial C}{\partial x} \qquad 3.7$$

$$\frac{\rho_b}{\theta_w}\frac{\partial S}{\partial t} = k_{att} C \qquad 3.8$$

where, S is the attached or solid-phase concentration and k_{att} is the rate of particle attachment. Steady-state filtration and negligible hydrodynamic dispersion effects are often assumed in applications of colloid filtration theory (Elimelech and O'Melia, 1990; Harvey and Garabedian, 1991; Tufenkji and Elimelech, 2004). For a continuous colloid injection at concentration C_0 over a fixed time period of t_0, the analytical solutions to eqs 3.7 and 3.85 suggest exponential decay of concentrations of suspended and retained particles with distance:

$$C(x) = C_0 \exp\left(-\frac{k_{att}}{v} x\right) \qquad 3.9$$

$$S(x) = \frac{t_0 \theta_w k_{att} C_0}{\rho_b} \exp\left(-\frac{k_{att}}{v} x\right) \qquad 3.10$$

In this work, the applicability of clean-bed filtration theory to nC_{60} aggregate transport in water-saturated columns packed with glass beads was evaluated. The attachment rate k_{att} was estimated by minimizing the difference between measured effluent concentration data and calculated values obtained from the solution to eqs 3.9 and 3.10.

3.4.3. SIMULATION OF NANOPARTICLE TRANSPORT AND RETENTION

The transport and retention of nC_{60} aggregates was modeled using a modified version of the traditional one-dimensional (1-D) advective-dispersive reactive (ADR) transport equation:

$$\frac{\partial C}{\partial t} + \frac{\rho_b}{\theta_w}\frac{\partial S}{\partial t} = D_H \frac{\partial^2 C}{\partial x^2} - v_p \frac{\partial C}{\partial x} \qquad (3.11)$$

where, C is the concentration of nC_{60} in solution, S is the concentration of nC_{60} associated with the solid phase, t is time, x is the distance parallel to flow, ρ_b is the soil bulk density, and D_H is the hydrodynamic dispersion coefficient. The kinetics of nC_{60} aggregate attachment was expressed as (Saiers et al., 1994):

$$\frac{\rho_b}{\theta_w}\frac{\partial S}{\partial t} = k_{att}\psi C - \frac{\rho_b}{\theta_w}k_{\det}S \tag{3.12}$$

where k_{att} is the rate of nC_{60} attachment, k_{det} is the rate of nC_{60} detachment, and ψ is related to the maximum nC_{60} retention capacity S_{max} by (Johnson and Elimelich, 1995):

$$\psi = \frac{S_{\max} - S}{S_{\max}} \tag{3.13}$$

When S_{max} is much larger than S, eq 3.13 reduces to unity and the model will converge to the clean-bed filtration model. The rate of nC_{60} attachment k_{att} can be expressed as (Yao et al., 1971):

$$k_{att} = \frac{3(1-\theta_w)v_p}{2d_c}\alpha\eta_0 \tag{3.14}$$

where the collision efficiency factor (α) represents the fraction of nC_{60} that remain attached after collision and the single collector efficiency (η_0) represents the frequency of nC_{60} collisions with the porous medium grain surfaces, which can be calculated using the correlation (Tufenkji and Elimelich, 2004):

$$\eta_0 = 2.4A_s^{1/3}N_R^{-0.081}N_{Pe}^{-0.715}N_{vdw}^{0.052} + 0.55A_sN_R^{1.675}N_A^{0.125} + 0.22N_R^{-0.24}N_G^{1.11}N_{vdw}^{0.053} \tag{3.15}$$

where A_s is the Happel correction factor, N_R is the interception number, N_{Pe} is the Peclet number, N_{vdw} is the London-van der Waals attractive forces number, N_A is the attraction number, and N_G is the gravitational number. The three terms in eq 6 represent the contributions of diffusion, interception and sedimentation processes, respectively, to particle collision. A modified version of the HYDRUS-1D model (Simunek et al., 2003) was used to solve eqs 3.11-3.15.

CHAPTER 4

RESULTS AND DISCUSSION

4.1 MOBILITY OF nC_{60} IN WATER-SATURATED GLASS BEADS AND QUARTZ SAND

The objective of this work was to investigate the transport and retention of nC_{60} particles in water-saturated porous media through a combination of laboratory-scale experiments and mathematical modeling. Eight nC_{60} transport experiments were conducted in glass columns packed with either glass beads or Ottawa sand, which were sectioned and extracted to obtain particle retention profiles following a pulse injection of nC_{60} suspension. Batch sorption experiments were performed to corroborate nC_{60} column retention data, and aqueous solutions were prepared with either 1.0 mM $CaCl_2$ or DI water to evaluate the effect of ionic strength on nC_{60} transport. A one-dimensional (1D) particle transport simulator, based on the HYDRUS 1D code described in Chapter 3, was developed and evaluated by comparison of model predictions to experimentally measured nC_{60} transport and retention data.

4.1.1. nC_{60} TRANSPORT AND RETENTION

A total of eight individual column experiments were conducted in water-saturated 40-50 mesh glass beads (GB) or Ottawa sand (OS) at a single flow rate. The conditions of each experiment, including the aqueous phase pore volume (PV), volumetric water content (θ_w), input concentration (C_0), pulse width (PW) and ionic strength (IS) are given in Table 4.1. The total C_{60} mass balance, based on the amount recovered in column effluent and extracted from the solid phase, relative to the amount injected ranged from 95 to 102%.

Table 4.1. Experimental conditions of nC_{60} transport studies conducted in water-saturated glass columns packed with either 40-50 mesh glass beads (GB) or Ottawa sand (OS).

Column	PV[a] (mL)	θ_w[b]	C_0[c] (mg/L)	PW[d] (pv)	IS[e] (mM)	MB[f] (%)
GB-1	28.0	0.38	2.44	3.0	3.065	95.8
GB-2	28.0	0.38	1.34	3.0	3.065	100.5
GB-3	28.0	0.38	1.34	3.0	3.065	94.6
GB-4	28.0	0.38	3.06	3.0	0.0	100.6
OS-1	26.5	0.36	2.33	3.0	3.065	98.4
OS-2	27.2	0.37	2.25	4.56	3.065	97.6
OS-3	27.2	0.37	1.34	3.0	3.065	102.2
OS-4	25.8	0.35	2.31	3.45	0.0	100.2

[a] aqueous phase pore volume. [b] volumetric water content. [c] influent nC_{60} concentration. [d] pulse width expressed in dimensionless pore volumes. [e] ionic strength. [f] mass balance of nC_{60}.

Effluent breakthrough curves (BTCs), obtained for nC_{60} aggregate transport through water-saturated columns packed with either 40-50 mesh glass beads or Ottawa sand, are shown in Figures 4.1A and 4.1B, respectively. Pulse injections (3 or 5 PV) of the nC_{60} suspensions containing 1.0 mM $CaCl_2$ as a background electrolyte yielded asymmetrical BTCs that gradually

increased to a maximum value before declining sharply to relative concentrations (C/C_0) approaching zero. For the glass bead columns, nC_{60} appeared in the column effluent after injecting approximately 1.1 PVs of suspension, while in columns packed with Ottawa sand nC_{60} breakthrough occurred at approximately. 1.8 PVs. These data indicate that Ottawa sand had a greater capacity to retain nC_{60} aggregates relative to glass beads of the same size. During the initial breakthrough period, the area above the nC_{60} BTC (i.e., the region between the measured data points and a relative concentration (C/C_0) of 1.0) corresponds to the mass of nC_{60} particles retained by the solid phase. Under ideal conditions (i.e., reversible, equilibrium) this retained mass would be eluted from the column upon the re-introduction of nC_{60}-free water, and would appear in the BTC as gradual decline in effluent concentration. However, the sharp reduction in relative concentration observed in the distal portion of the BTCs indicates that retained nC_{60} aggregates were not released from the solid phase and suggests that the detachment coefficient (k_{det}) approaches zero under these experimental conditions. Such irreversible attachment is consistent with the findings of Chen and Elimelech (2006), who reported that nC_{60} aggregates deposited on a silica-coated quartz surface in a 0.6 mM $CaCl_2$ solution at pH 5.2 were not released until the rinse solution contained DI water adjusted to pH 12.3.

For comparison purposes, representative BTCs obtained for 3 PV pulse injections of non-reactive tracer (Br^-) are shown as dotted lines in Figures 4.1A and 4.1B. As anticipated, the fitted retardation factors (R_F) for all of the tracer studies were equal to 1.0 ± 0.02, while the Peclet numbers (N_{Pe}) for the glass bead and Ottawa sand columns were approximately 230 and 180, respectively (see Supporting Information). The Peclet numbers correspond to hydrodynamic dispersivity values ($\alpha_D = D_H / v_p$) of 0.065 and 0.084 cm, respectively, which are consistent with the relatively small values of α_D reported for laboratory-scale columns packed with uniform sand (Pennell et al., 1993). Additionally, the symmetrical shape and absence of tailing in the non-reactive tracer BTCs indicate that physical nonequilibrium processes, such as rate-limited mass transfer into regions of immobile water and preferential flow paths, did not contribute to retention of nC_{60} aggregates or the observed asymmetry in the nC_{60} BTCs (see Figure 4.2).

A nearly 2-fold increase (1.34 to 2.44 mg/L) in the concentration of nC_{60} injected into the glass bead columns (exp. GB-1) resulted in a steeper rise to a maximum relative concentration. At the lower concentration of 1.34 mg/L, the maximum or plateau concentration was not achieved after injecting 3 PV of nC_{60} suspension (exps. GB-2 and GB-3). However, the distal portion of the BTCs exhibited an identical shape irrespective of input concentration, suggesting that the capacity of the solid phase to retain nC_{60} had not been exceeded. For the Ottawa sand columns, increasing the input concentration did not yield a discernable change in the shape of the nC_{60} BTCs. At the higher input concentration of 2.44 mg/L, a 5 PV pulse of nC_{60} was required to reach a maximum relative effluent concentration of ca. 0.85 (exp. OS-2). The larger applied volume of nC_{60} (5 PV vs. 3 PV) required to reach a maximum effluent concentration indicates that Ottawa sand possesses a greater capacity to retain nC_{60} aggregates relative to glass beads, which is consistent with the delayed nC_{60} breakthrough observed in the Ottawa sand columns.

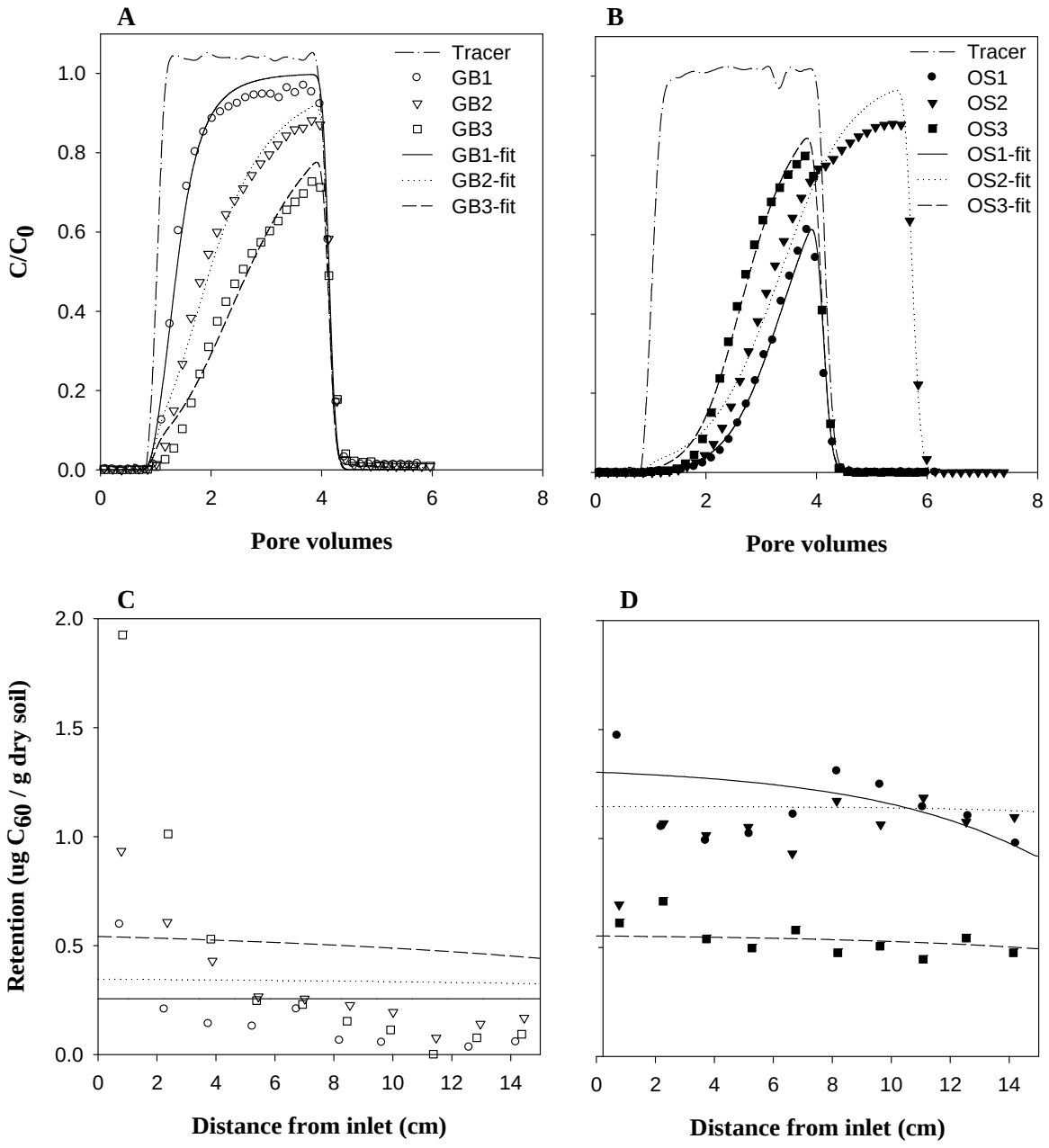

Figure 4.1. Measured and simulated nC_{60} breakthrough curves (A and B) and retention profiles (C and D) in water-saturated columns packed with either 40-50 mesh glass beads (open symbols) or Ottawa sand (solid symbols), respectively. Aqueous nC_{60} suspensions contained 1.0 mM $CaCl_2$, buffered to pH 7 with 0.065 M $NaHCO_3$, applied at a Darcy velocity of 2.8 m/d. .

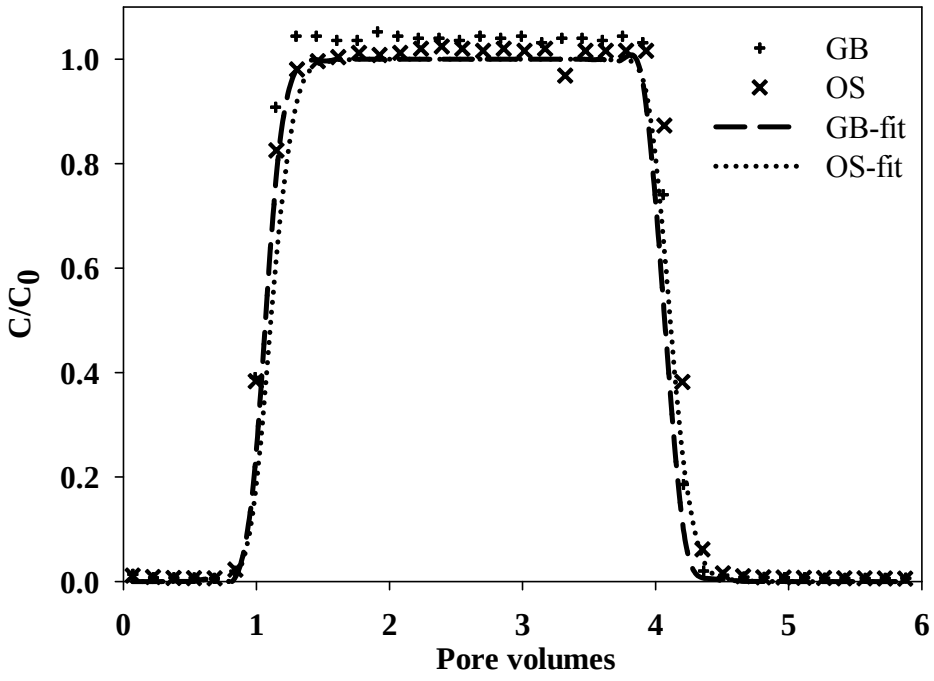

Figure 4.2. Measured and simulated non-reactive tracer breakthrough curves (BTCs) in columns packed with either 40-50 mesh glass beads (GB) or Ottawa sand (OS).

4.1.2. ELECTROSTATIC INTERACTIONS

Interaction energies between nC_{60} aggregates and the solid surface were calculated based on the Derjaguin-Landau-Verwey-Overbeek (DLVO) theory (Guzman et al., 2006), assuming a value of 2.76×10^{-20} J for the Hamaker constant (Lecaonet et al., 2004) and zeta potentials of -55 mV (Tufenkji and Elimelech, 2005) and -30 mV (Kara and Yukselen, 2005) for glass beads and Ottawa sand, respectively. The resulting DLVO energy profiles indicate that a sizable repulsive energy barrier of ca. 30.9 kT and 16.4 kT existed between nC_{60} aggregates and glass beads and Ottawa sand, respectively (Figure 4.3), consistent with the lower nC_{60} retention observed in the glass bead columns. The large primary electrostatic energy barrier should, in theory, prevent deposition of nC_{60} aggregates. However, divalent cations are known to form complexes with negatively charged surface sites, thereby reducing the repulsive surface charge (Kara and Yukselen, 2005; Ko and Elimelech, 2000), an effect not accounted for in DLVO theory. A small secondary minimum attractive region was calculated for both Ottawa sand and glass beads, with depths of -0.31 kT and -0.25 kT at 33.5 and 38.7 nm from surface, respectively, which could have also contributed to nC_{60} deposition. In addition, differences in surface roughness and mineral structure, which are not accounted for in DLVO theory, may have contributed to the greater nC_{60} retention observed in Ottawa sand columns.

Two additional column experiments (GB-4 and OS-4) were performed with DI water alone (i.e., no background electrolyte or pH buffer) to further investigate the role of electrostatic interactions in nC_{60} aggregate retention. The resulting nC_{60} effluent BTCs obtained at a Darcy velocity of 2.8 m/d are shown in Figure 4.4. In contrast to the column experiments conducted at an ionic strength of 3.065 mM, nC_{60} effluent BTCs for both the glass bead and Ottawa sand

columns coincided with non-reactive tracer (Br^-), indicating that there was minimal retention of nC_{60} aggregates by the solid phases. Subsequent column extraction revealed that no measurable amounts of nC_{60} were retained by the glass beads, while less than 5% of the injected mass was recovered from the Ottawa sand column (Figures 2C and 2D). The observed enhancement in nC_{60} transport coincided with the larger absolute value of the zeta potential in water alone (-64.0 ± 2.0 mV) compared to that in 1.0 mM $CaCl_2$ (-23.9 ± 3.1 mV). These data are consistent with the reported increase in nC_{60} aggregate mobility when the ionic strength was reduced from 100 mM NaCl to 1 mM (Brant et al., 2005), and further support the importance of electrostatic interactions in nC_{60} retention.

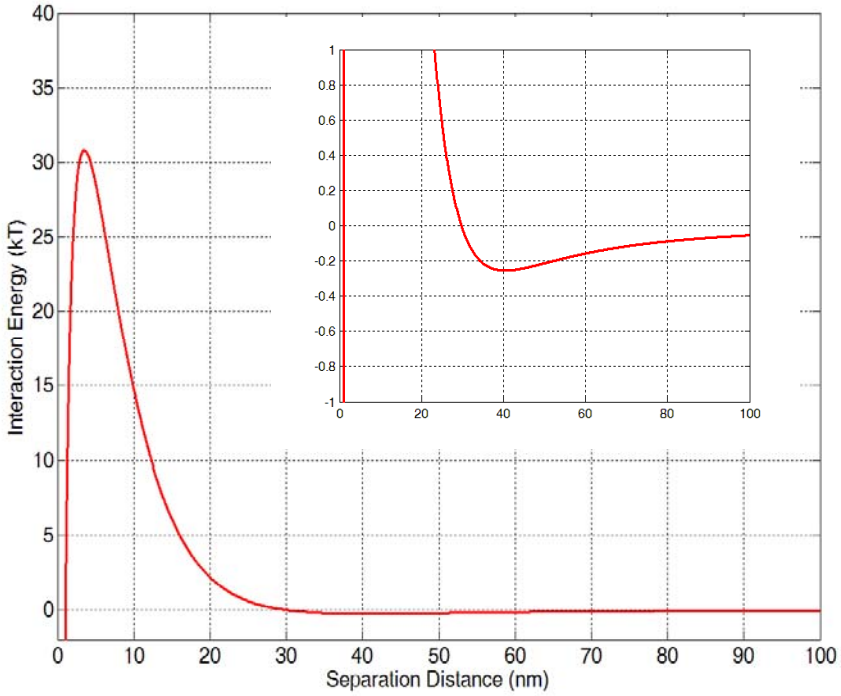

Figure 4.3. DLVO interaction energy plots between an nC_{60} aggregate and a glass bead surface. The inset shows an enlargement of the secondary energy minimum region.

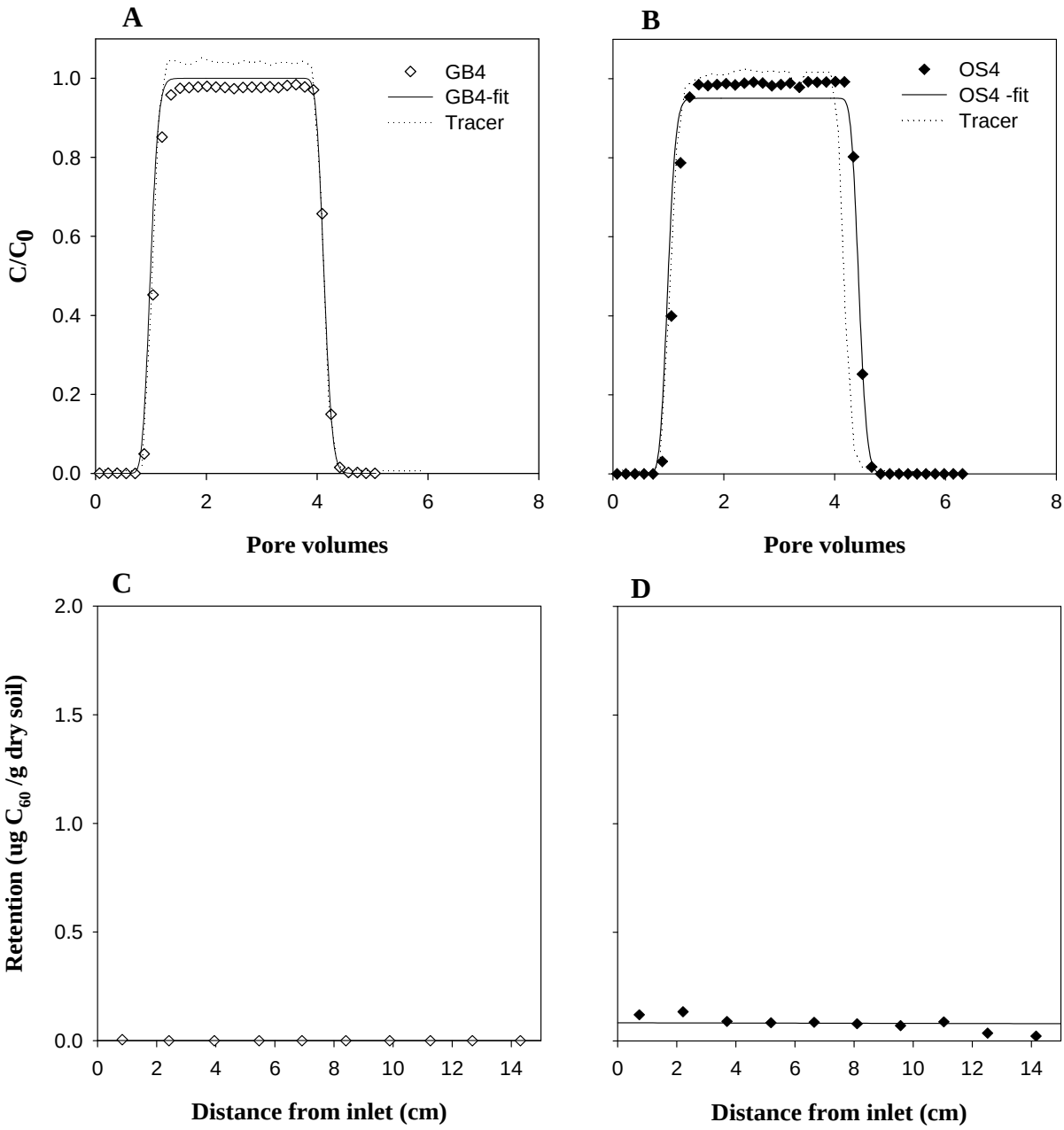

Figure 4.4. Measured and simulated nC_{60} breakthrough curves (A and B) and retention profiles (C and D) in water-saturated columns packed with either 40-50 mesh glass beads (open symbols) or Ottawa sand (solid symbols), respectively. Aqueous nC_{60} suspensions were prepared in DI water, and were applied at a Darcy velocity of 2.8 m/d.

4.1.3. RETENTION OF nC_{60} AGGREGATES

Immediately following each transport experiment, the columns were sectioned into ten 1.5-cm increments and nC_{60} aggregates were extracted from the solid phase by sonication in DI water. The resulting nC_{60} retention profiles for the glass bead and Ottawa sand columns are plotted in Figures 4.1C and 4.1D, respectively, where a distance of 0 cm corresponds to the column inlet. Overall mass balance recoveries were computed from the ratio of the nC_{60} mass injected and the sum of the mass recovered from the column effluent and solid phase extraction, and ranged from 95 to 102%. For the glass bead columns, nC_{60} aggregate retention decreased with distance from the column inlet. In contrast, the retention of nC_{60} in the Ottawa sand columns was relatively uniform over the entire length of the column, and was similar in magnitude regardless of the input concentration (Table 4.1). The relatively constant deposition profile in the Ottawa sand columns suggests that nC_{60} deposition approached a limiting capacity.

To independently assess nC_{60} retention behavior, batch reactor experiments were conducted in which aqueous suspensions of nC_{60} were gently mixed with Ottawa sand and glass beads for a period of 3h. The resulting nC_{60} retention data are plotted in Figure 4.5 as concentration of nC_{60} associated with the solid phase (S) versus the final aqueous phase concentration (C). In the presence of 1.0 mM $CaCl_2$, Ottawa sand exhibited the greatest retention capacity, approaching 4 μg/g at an nC_{60} concentration of approximately 9.0 mg/L. When DI water alone was used as the aqueous phase, retention of nC_{60} by Ottawa sand decreased substantially, yielding a solid phase concentration of 0.07 μg/g, consistent with the trends in observed in column experiment OS-4 (Figure 4.4D). As was anticipated from the column results, batch retention of nC_{60} by glass beads was considerably less than that measured for Ottawa sand. In the presence of 1.0 mM $CaCl_2$, nC_{60} retention by glass beads approached a maximum value of ca. 0.9 μg/g. In DI water alone, retention nC_{60} by glass beads was negligible, consistent with the retention profile observed in column experiment GB-4 (Figure 4.4C).

4.1.4. MATHEMATICAL MODELING

The mathematical model successfully captured the gradual increase and sharp decline of the nC_{60} BTCs observed with columns packed with either 40-50 mesh glass beads or Ottawa sand in the presence of 1.0 mM $CaCl_2$ (Figures 1A and 1B). Soil bulk density (ρ_b) and volumetric water content (θ_w) were determined independently from physical measurements of the column, while the hydrodynamic dispersion coefficient (D_H) was obtained from the non-reactive tracer BTCs (Figure 4.2). Based on preliminary simulations, the particle detachment rate coefficient (k_{det}) was found to be negligible (ca. 1×10^{-4} 1/h), consistent with the sharp reduction in effluent nC_{60} concentrations upon re-introduction of the nC_{60} free solution. These findings indicate that upon retention by the solid phase, nC_{60} particles are not subsequently released under constant flow and background electrolyte conditions. Thus, only two parameters, the particle attachment rate (k_{att}) and retention capacity (S_{max}), were obtained by an optimization procedure that minimized the difference between the simulated and measured effluent concentration data (Simunek et al., 2005). In the presence of 1.0 mM $CaCl_2$, values of k_{att} for the glass bead and Ottawa sand columns ranged from 3.6 to 4.4 1/h and from 7.3 to 9.2 1/h, respectively. The larger values of k_{att} and S_{max} obtained for Ottawa sand relative to glass beads are consistent with the nearly two-fold later breakthrough of nC_{60} particles observed in the column effluent (Figures 4.1A and 4.1B) and the greater retention capacity of Ottawa sand obtained in batch experiments (Figure 4.5).

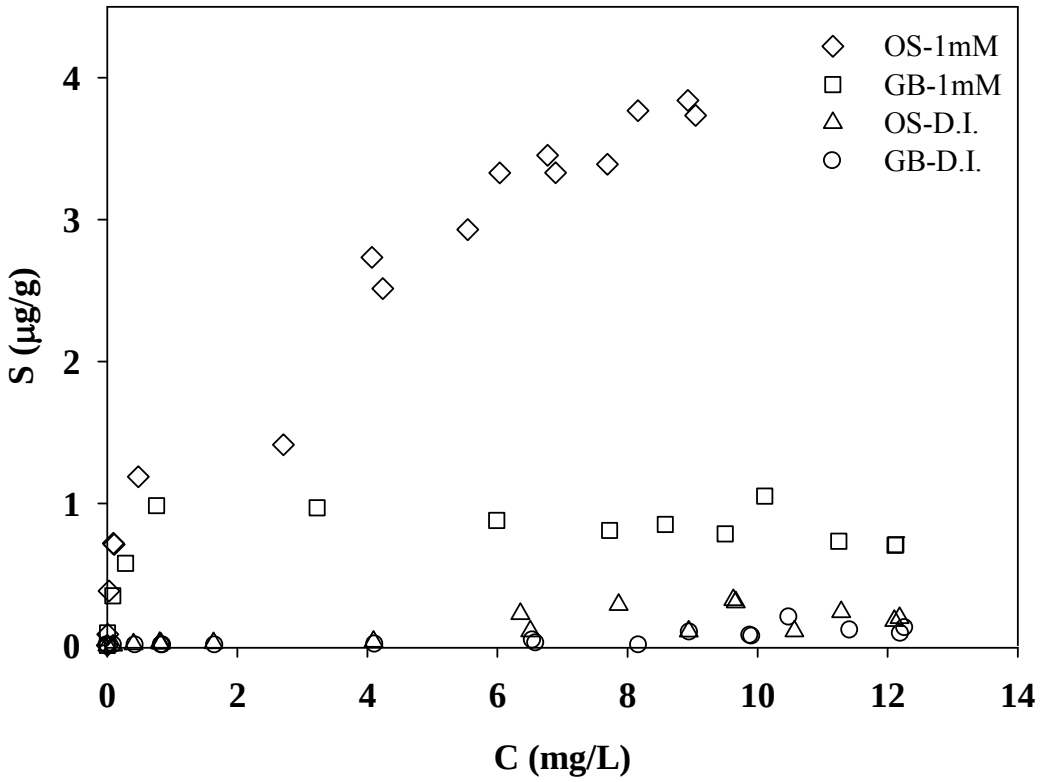

Figure 4.5. Retention of nC_{60} aggregates in batch reactors containing either glass beads (GB) or Ottawa sand (OS) in 1.0 mM $CaCl_2$ aqueous solution or DI water.

Collision efficiency factors (α) were calculated using eq 5 based on the measured values of k_{att}, known column parameters (i.e., d_c, v_p, and θ_w), and the single collector efficiency (η_0) calculated using eq 3.11. The resulting collision efficiency factors ranged from 0.066 to 0.079 for glass beads and from 0.122 to 0.153 for Ottawa sand (Table 4.2), which are in close agreement with the value of 0.05 reported by (Espinasse et al., 2007) for a continuous injection of THF-prepared nC_{60} aggregates (92 nm dia.) in columns packed with 40-50 mesh glass beads at an ionic strength of 5 mM (NaCl). Collision efficiency factors of less than 1 are considered to be unfavorable, indicating a net repulsive force between the nC_{60} aggregates and the solid surface. The two-fold smaller collision efficiency factors obtained for glass beads compared to Ottawa sand are consistent with the nC_{60} transport and retention behavior observed in the column experiments. Calculated values of the single collector efficiency (η_0) were approximately 0.06 for all column experiments (Table 4.2). The first term in eq 3.11 accounted for 99.9% of the calculated η_0 value, suggesting that diffusion was the dominant mechanism governing the nC_{60} aggregate collisions with the porous media.

The values of S_{max} obtained from model simulations ranged from 0.56 to 1.31 µg/g for Ottawa sand and from 0.25 to 0.56 µg/g for glass beads, and are in general agreement with values estimated from the batch retention experiments (Table 4.2). Using the S_{max} value of 1.13 µg/g obtained in column experiment OS2, the fractional surface coverage (θ_s) is 1.9×10^{-3}, based

on the theoretical specific surface area of Ottawa sand (6.4×10^{-3} m^2/g) and the nC_{60} aggregate diameter (100 nm). The fractional collector surface coverage can also be estimated from the effluent BTC (Ko and Elimelech, 2000):

$$\theta_s = \frac{\pi r_a^2 r_c q N_0 \int_0^t (1 - N/N_0)dt}{3L(1-\theta_w)} \quad (4.1)$$

where r_a is the radius of the aggregate, r_c is the radius of the collector or porous medium, q is the Darcy velocity, N_0 is the influent particle concentration, and N is the effluent particle concentration. For column experiment OS2, the fractional surface coverage obtained from eq 7 is 2.4×10^{-3}. Thus, S_{max} represents a maximum retention capacity, rather than monolayer coverage, which is very small due to the repulsive force between nC_{60} aggregates at low ionic strength.

Table 4.2. Simulation parameters used to fit nC_{60} breakthrough curves in water-saturated columns packed with either 40-50 mesh glass beads (GB) or Ottawa sand (OS).

Column	Measured Retention (%)	Simulated Retention (%)	Measured S_m [a] (μg/g)	Simulated S_{max} (μg/g)	k_{att} [b] (1/h)	α [c]	η_0 [d]
GB-1	8.6	13.1	0.83	0.247	3.52	0.066	0.061
GB-2	33.8	35.1	0.80	0.353	3.63	0.066	0.060
GB-3	48.9	43.7	0.80	0.564	4.41	0.079	0.060
GB-4	0.0	0.018	6.6×10^{-3}	4.0×10^{-4}	0.09	5.0×10^{-4}	0.060
OS-1	77.0	72.5	2.02	1.313	9.19	0.153	0.059
OS-2	48.1	46.3	1.98	1.13	7.23	0.122	0.060
OS-3	59.7	55.4	1.57	0.561	7.27	0.128	0.060
OS-4	4.8	4.67	0.07	4.97×10^{4}	0.11	5.7×10^{-3}	0.058

[a] estimated retention capacity based on batch experiments, [b] attachment rate, [c] collision efficiency factor, [d] single collector efficiency.

While the numerical model captured the relatively constant nC_{60} retention profiles obtained for Ottawa sand, simulated nC_{60} retention profiles for the glass bead columns failed to mimic the observed retention, which was greatest near the column inlet and approached zero at the column outlet (Figure 4.1C). Use of a classical clean-bed filtration model to simulate nC_{60} transport and retention in the glass bead columns yielded relatively poor fits to the effluent BTC data and provided only minimal improvements in predictions of nC_{60} retention near the column inlet (Figure 4.6). Thus, the elevated retention of nC_{60} in the glass bead columns may have been due to nC_{60} interactions with previously deposited aggregates near the column inlet, which were not considered in the models employed herein. In presence of water alone, nC_{60} aggregate transport and retention in glass beads and Ottawa sand was accurately captured by the numerical model (Figure 4.4). Simulated k_{att} values were 0.09 and 0.11 1/h for glass beads and Ottawa sand, respectively, which yielded extremely small collision efficiency factors, consistent with a strong

net repulsive force between the solid surface and nC_{60} aggregates under these conditions. Taken in concert, the experimental and mathematical modeling studies demonstrate the importance of electrostatic interactions in nC_{60} aggregate transport and deposition in water-saturated porous media, and the existence of a maximum or limiting nC_{60} retention capacity in quartz sands.

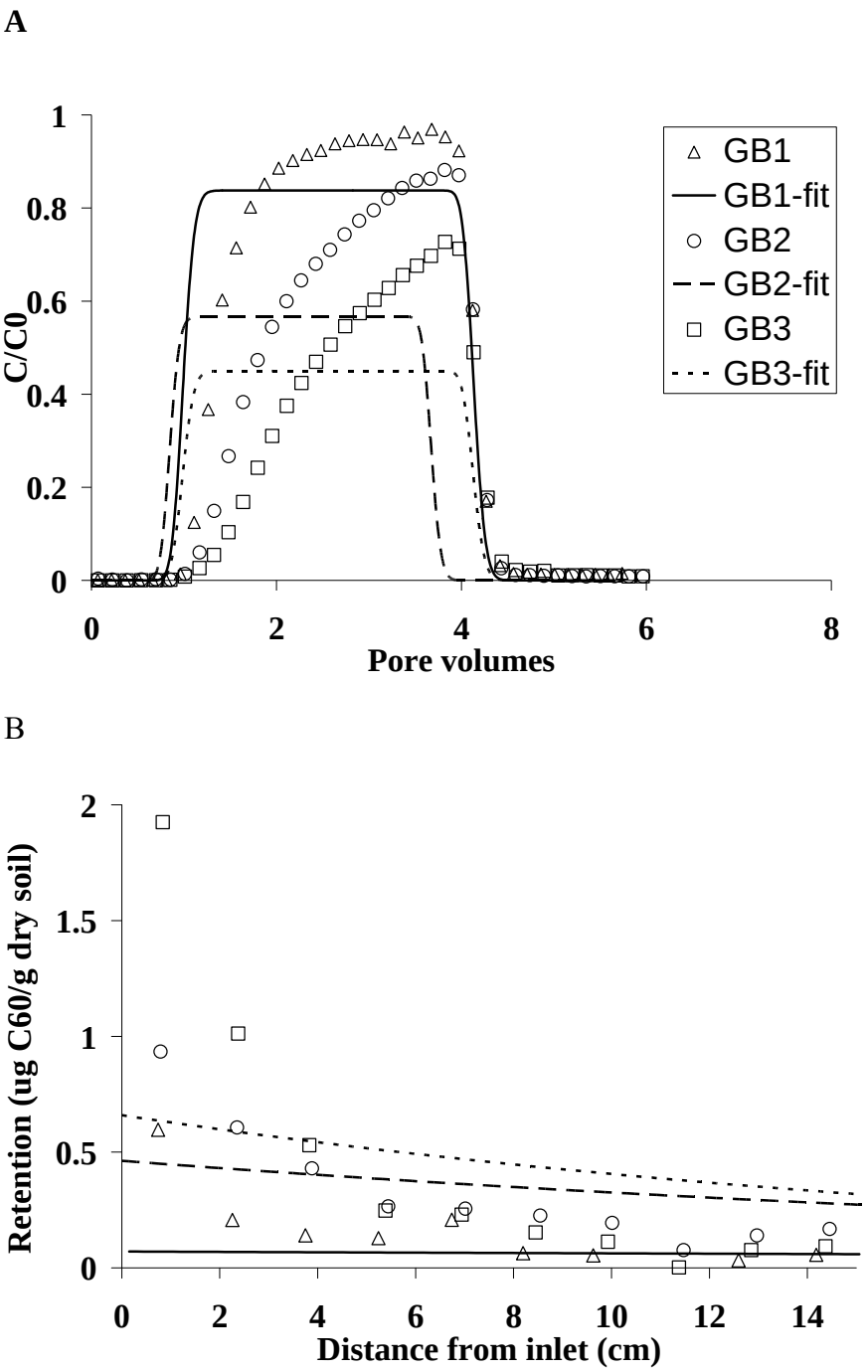

Figure 4.6. Comparison of filtration model simulations and measured nC_{60} breakthrough curves (A) and retention profiles (B) for columns packed with glass beads (GB) in the presence of 1.0 mM $CaCl_2$.

4.2. EFFECTS OF SOLUTION CHEMISTRY ON nC_{60} AGGREGATION AND TRANSPORT

The influence of electrolyte species and concentration on the aggregation and transport of nC_{60} in water-saturated sands was investigated through a combination of batch and column experiments. The mean diameter, size distribution and surface charge of nC_{60} particles were quantified in aqueous suspensions containing either NaCl or $CaCl_2$ as a background electrolyte. A series of one-dimensional column studies was performed to assess the transport, deposition and recovery of nC_{60} particles in either 40 to 50 mesh (d_{50} = 0.335 mm) or 100 to 140 mesh (d_{50} = 0.125 mm) quartz sand. Effluent concentration data and solid-phase retention profiles were obtained following pulse injections (five pore volumes) of nC_{60} suspensions prepared with either NaCl or $CaCl_2$ at ionic strengths of 3.05 and 30.05 mM. For conditions yielding near complete retention of the introduced nC_{60} particles, a prolonged elution phase was conducted to evaluate the ability of increased flow rate, reduced ionic strength, increasing pH, and the addition of a cosolvent or surfactant to recover deposited nC_{60} particles. Experimental data are interpreted within the context of particle-particle and particle-surface electrostatic interactions, providing a mechanistic framework to explain the transport, deposition and release of nC_{60} in water-saturated quartz sands.

4.2.1. EFFECTS OF SOLUTION PROPERTIES ON NC60 AGGREGATION

The mean diameter and size distribution of nC_{60} particles in aqueous suspension was systematically studied in batch experiments as a function of electrolyte species and concentration, solution addition rate, mixing sequence and final nC_{60} concentration. In general, the diameter of nC_{60} particles increased with electrolyte concentration (Figure 4.7A), in agreement with previous reports of nC_{60} particle formation and stability behavior (Fortner et al., 2005; Brant et al., 2005; Chen and Elimelech, 2006). At low electrolyte concentrations (≤ 1.0 mM), the diameter of nC_{60} particles was consistent with the initial stock suspension value of 92 nm regardless the electrolyte species, solution addition rate, or mixing sequence. At electrolyte concentrations greater than 1.0 mM, however, nC_{60} particle size was dependent upon electrolyte species and solution addition sequence, especially in the presence of $CaCl_2$. For example, when the concentration of $CaCl_2$ was increased from 1 to 100 mM the mean nC_{60} particle diameter increased from 92 nm to more than 500 nm regardless of mixing rate and sequence (Figure 4.7A). The corresponding nC_{60} growth factors, defined as the ratio of the particle diameter measured in the prepared aqueous suspension to that of the initial stock suspension, ranged from 5.3 to 7.3 in the presence of 10 and 100 mM $CaCl_2$. The nC_{60} particle diameter in aqueous suspension was dependent upon the mixing sequence; with addition nC_{60} stock suspension to aqueous $CaCl_2$ solutions (referred to as E1S2) resulting in an nC_{60} particle diameter that was approximately 25% greater than when the addition sequence was reversed (referred to as S1E2). In the presence of NaCl, changes in nC_{60} particle diameter as a function of electrolyte concentration and mixing condition were relatively minor (Figure 4.7A). Over the range of NaCl concentrations considered (1-100 mM), the mean nC_{60} particle diameter increased from 92 to 135 nm, corresponding to growth factors of less than 1.4.

Representative intensity-weighted nC_{60} particle size distributions are shown in Figure 4.7B for suspensions prepared by addition of nC_{60} stock suspensions to aqueous solutions (E1S2 sequence) containing either NaCl or $CaCl_2$ at an ionic strength of 30.05 mM and an addition rate

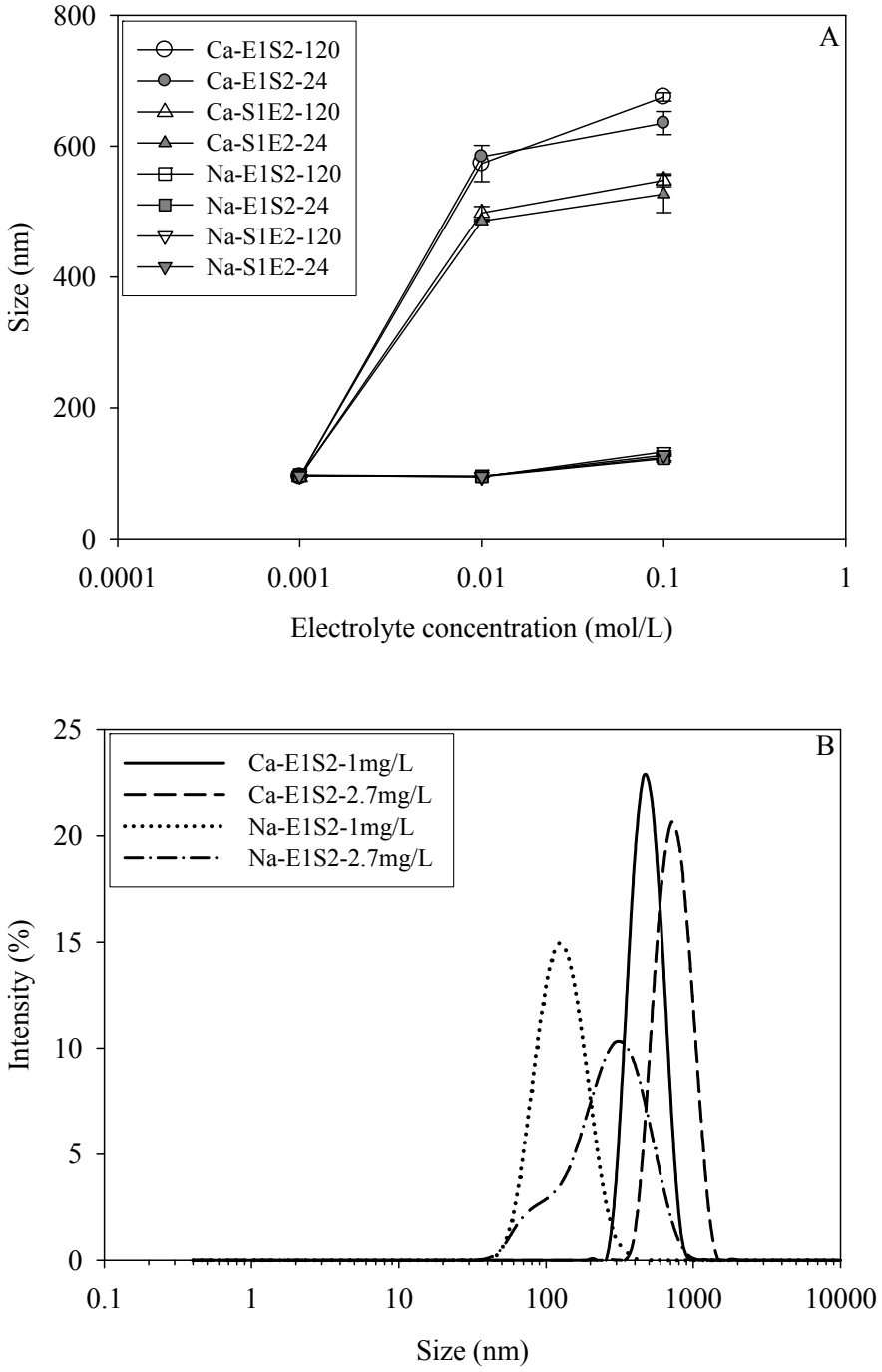

Figure 4.7. Effect of electrolyte concentration, suspension addition rate (24 or 120 ml/min), and dilution sequence (E1S2 or S1E2) on (A) the mean nC_{60} particle diameter at a final concentration of 1.0 mg/L and (B) intensity-weighted size distribution of nC_{60} particles as a function of final concentration at a mixing rate of 120 ml/min and ionic strength of 30.05 mM. E1S2 refers to the sequence of adding the electrolyte solution to the nC_{60} stock suspension, while S1E2 refers to the sequence of adding the nC_{60} stock suspension to the electrolyte solution. Error bars represent the standard deviation of duplicate or triplicate measurements.

of 120 ml/min. Interestingly, the mean particle diameter was dependent upon the final nC_{60} concentration (either 1.0 or 2.7 mg/L), with a shift toward larger particle sizes at the higher final concentration. These trends were less pronounced at lower ionic strength, but nevertheless, demonstrate the sensitivity of the aggregation process to different suspension preparation methods. The shoulder observed in the size distribution of nC_{60} particles in NaCl at a final concentration of 2.7 mg/L is indicative of a bimodal distribution, with two distinct particle diameters of approximately 100 nm and 300 nm (Figure 4.7B). These findings suggest that the initial 100-nm diameter particles formed larger nC_{60} clusters or agglomerates in the presence of higher electrolyte and nC_{60} concentrations. Here, we hypothesize that the nC_{60} aggregation or agglomeration process was enhanced at higher nC_{60} concentrations due to greater collision efficiency, consistent with the findings of Chen and Elimelech (2006), who concluded that nC_{60} aggregation is a diffusion-controlled process.

The role of electrolyte species and concentration on nC_{60} aggregation behavior was evaluated using Derjaguin-Landau-Verwey-Overbeek (DLVO) theory. According to DLVO theory, the interaction energy (E_i) between two particles is composed of the electrical double layer repulsion energy (E_{edl}) and the van der Waals attraction energy (E_V). The value E_{edl} can be calculated from the equation of Gregory (1975):

$$E_{\text{edl}} = \frac{64\pi nkTa}{\kappa^2}\tanh^2\left(\frac{ze\psi}{4kT}\right)e^{(-\kappa d)} \tag{4.2}$$

where n is the number concentration of cations, k is Boltzmann constant, T is the absolute temperature, a is the particle radius (e.g., 47.5 nm), κ is the Debye-Huckel reciprocal length parameter, z is the charge number, e is the electron charge, ψ is the surface potential of the particle, and d is the surface to surface distance. The Debye-Huckel reciprocal length parameter (κ) can be calculated as $\kappa = \left(\frac{2000e^2 N_A I_c}{\varepsilon_0 \varepsilon_r kT}\right)^{1/2}$, where ε_0 is the permittivity of a vacuum, ε_r is the relative dielectric constant of water (78.54), N_A is Avogadro's number, and I_c is the ionic strength. Under low ionic strengths, the thickness of particle stern layer is relatively small and therefore, the surface potential is approximately equal to the zeta potential. The value of E_V was computed as (Gregory, 1981):

$$E_V = -\frac{Aa}{12d}\left(1 - \frac{bd}{\lambda}\ln\left(1 + \frac{\lambda}{bd}\right)\right) \tag{4.3}$$

where A is the Hamaker constant (4.71×10^{-21} J [16]), b is a constant with the value of 5.32, and λ is the characteristic wavelength of the interaction, assumed to be 100 nm (Schenkel and Kitchener, 1960). The resulting interaction energies between two nC_{60} particles as a function of distance are presented in Figure 4.8 for suspensions containing either NaCl or $CaCl_2$. Here, negative values represent a net attractive force, while positive values correspond to a net repulsive force. In the presence of $CaCl_2$ (Figure 4.8A), the energy minimum became more negative and approached the surface as the electrolyte concentration was increased, consistent with strong suppression of the electrical double layer by divalent cations. Under these conditions, van der Waals attractive forces dominate, which lead to the formation of agglomerates consisting of multiple n-scale particles as shown in Figure 1. In the presence of NaCl, a large positive interaction energy minimum was maintained for all but the highest concentration considered (100 mM), while a small secondary minimum was observed at a

separation distance of approximately 10 nm (Figure 4.8B). These findings indicate that a strong repulsive force existed between nC_{60} particles, consistent with the suspension stability and relatively constant diameter of nC_{60} particles observed over the range of NaCl concentrations considered (Figure 4.7).

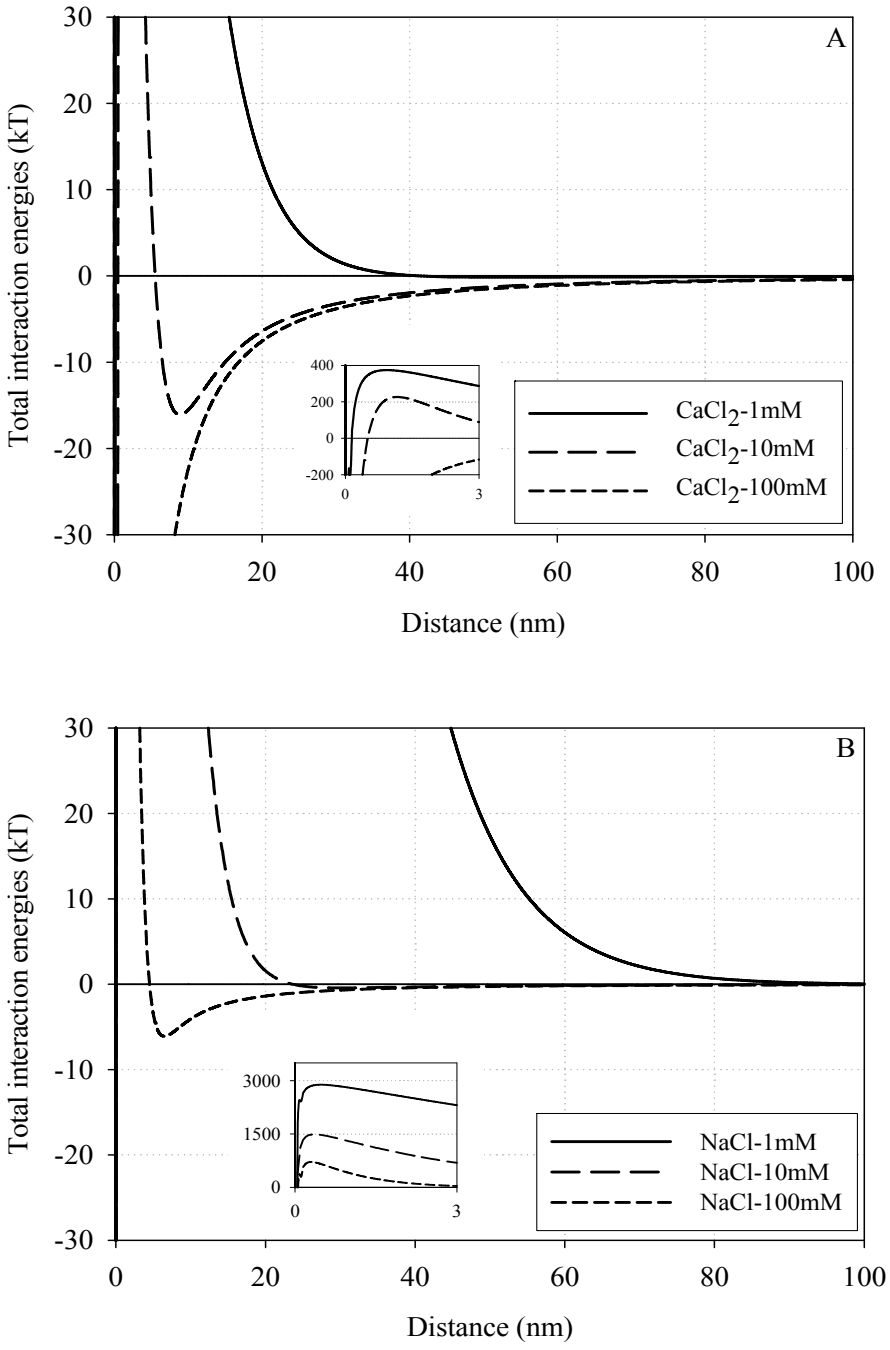

Figure 4.8. Interaction energies (E_i) between two nC_{60} particles as a function of (A) $CaCl_2$ and (B) NaCl concentrations at pH 7.

4.2.2. EFFECTS OF IONIC STRENGTH ON nC60 TRANSPORT AND RETENTION

Concentrations of nC_{60} particles transported through 40 to 50 mesh and 100 to 140 Ottawa sand (OS) in the presence of $CaCl_2$ at two ionic strengths (3.05 and 30.05 mM) are shown in Figure 4.9A. The data are expressed as effluent breakthrough curves (BTCs), where the relative concentration (C/C_0) is plotted against the number of PV introduced. For comparison purposes, a representative BTC obtained for a non-reactive tracer (bromide) is also shown in Figure 4.9A. In the experiments conducted with 40 to 50 mesh OS at the lower ionic strength (Ca-MS-3a,b), nC_{60} particles appeared in the column effluent after approximately 1.4 PV and gradually increased to a maximum relative concentration of approximately 0.9 after introduction of 2.5 to 3.0 PV of the nC_{60} suspension. The small decline in effluent concentration observed in experiment Ca-MS-3b at approximately 5 PV occurred following a 12-h period of flow interruption. Such behavior is characteristic of a rate-limited deposition or retention process, indicating that a local equilibrium assumption is not valid for these experimental conditions. Following reintroduction of nC_{60}-free solution, the effluent concentration of nC_{60} declined sharply, approaching a value of zero at approximately 6.5 PV. The asymmetric shape of the BTC indicates that deposited nC_{60} particles were not released from the Ottawa sand. This irreversible attachment of nC_{60} particles is consistent with the findings of Chen and Elimelech (2006). In contrast to the experiments discussed above, when either the ionic strength was increased from 3.05 to 30.05 mM or the sand grain size was decreased from 0.335 to 0.125 mm, virtually no nC_{60} particles were detected in the column effluent (Figure 4.9A). At the conclusion of each column experiment, sand was removed in 1.5-cm increments and extracted with DI water to obtain nC_{60} particle deposition profiles (Figure 4.9B). As anticipated, nC_{60} particle retention was greatest near the column inlet and declined rapidly with distance for the column experiments conducted in 40 to 50 mesh Ottawa sand at an ionic strength of 30.05 mM. When the ionic strength was increased from 3.05 to 30.05 mM ($CaCl_2$), the mean diameter of the nC_{60} particles in the influent suspension increased from approximately 120 nm to 817 and 989 nm. For 100-140 mesh Ottawa sand at an ionic strength of 3.05 mM, a more gradual decrease in nanoparticle retention with distance from the column inlet was observed. In contrast, the deposition profile obtained in 40 to 50 mesh Ottawa sand at an ionic strength of 3.05 mM was essentially flat, indicating that a limiting retention capacity was achieved throughout the column, similar to the findings of shown in Section 4.1.

When NaCl was employed as the background electrolyte, much greater transport of nC_{60} particles was observed through Ottawa sand compared similar experimental conditions with $CaCl_2$ (Figure 4.10A). For example, in both 40 to 50 and 100 to 140 mesh Ottawa sand at an ionic strength 3.05 mM (experiments Na-MS-3 and Na-FS-3), nC_{60} particles appeared in the column effluent at approximately 1 PV, rapidly increased to relative concentration of 0.8, and then gradually approached a relative concentration of 1.0 after 6 PV. Thus, the nC_{60} effluent BTCs under these conditions nearly coincided with the non-reactive tracer BTC (dashed line, Fig. 5a). When the ionic strength was increased to 30.05 mM (NaCl), a small amount ($C/C_0 <$ 0.1) of nC_{60} still appeared in the column effluent over the duration of the pulse injection. As anticipated from the BTCs, the retention on nC_{60} particles in experiments conducted at ionic strength of 3.05 mM (NaCl) were minimal, while the experiment conducted at the higher ionic strength (30.05 mM) exhibited considerable retention near the column inlet, and decreased rapidly with distance from the column inlet (Figure 4.10B). For all of the nC_{60} column experiments, the total mass balance recovery, that is, the sum of mass retained and in column influent versus the introduced mass,

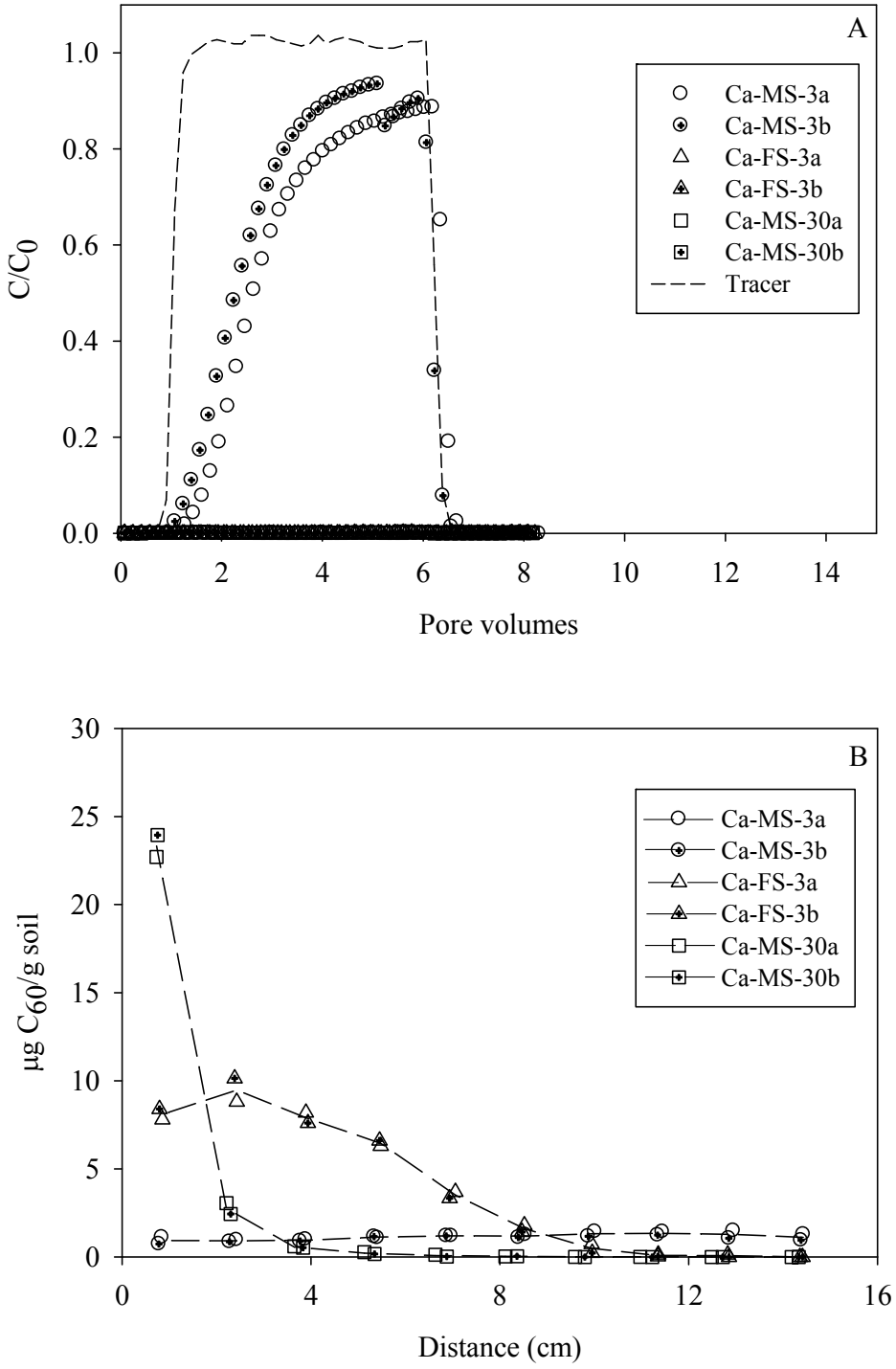

Figure 4.9. Effluent concentrations (A) and retention profiles (B) after pulse injections of nC_{60} particle suspensions in columns packed with either 40-50 mesh or 100-140 mesh Ottawa sand with $CaCl_2$ as the background electrolyte.

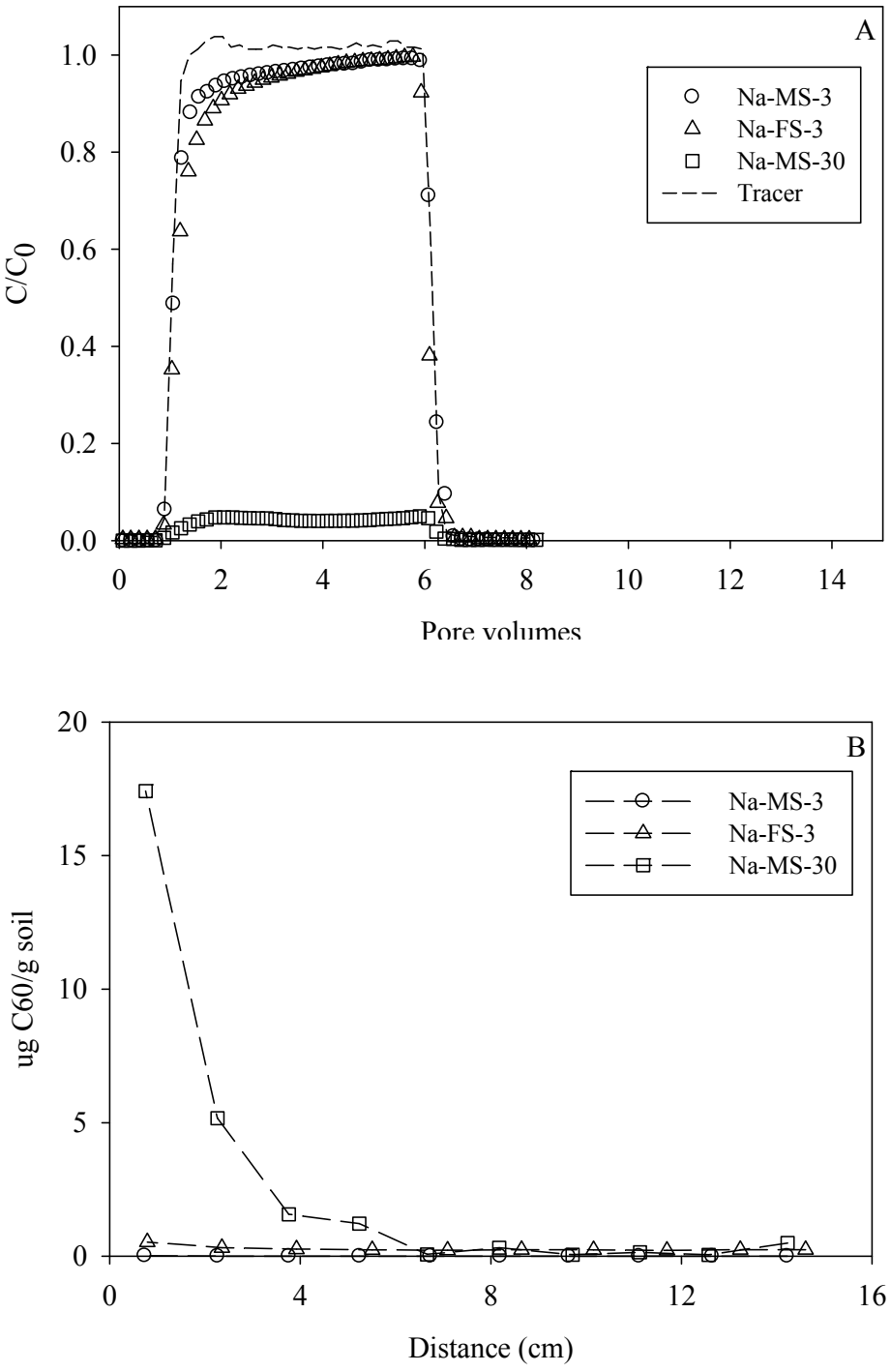

Figure 4.10. Effluent concentrations (A) and retention profiles (B) after pulse injections of nC_{60} particle suspensions in columns packed with either 40-50 or 100-140 mesh Ottawa sand with NaCl as the background electrolyte.

ranged from 88 to 105%, with the majority of experiment yielding recoveries of greater than 95%.

The sharp decrease in the distal portion of the nC_{60} BTCs is indicative of irreversible particle attachment (Figures 4.9A and 4.10A). To further investigate nanoparticle detachment, a series of recovery experiments were conducted in which nC_{60} particles were deposited in columns packed with 100 to 140 mesh Ottawa sand with 1.0 mM $CaCl_2$, followed by changes in flow rate, ionic strength or solution pH, addition of cosolvent or surfactant. Approximately 1% of the deposited nC_{60} particles were removed when the column was flushed with DI water (ionic strength ~ 0) or 50% ethanol, while doubling the flow rate or flushing with 0.1% Tween 80 resulted in negligible recovery of deposited nC_{60} particles (Experiments Ca-FS-3a,b). In contrast, injection of DI water (3 PV) adjusted to pH 10.0 and 12.0 (containing no background electrolyte) resulted in substantial increases in nC_{60} effluent concentration, corresponding to 17.2 and 27.6% of deposited mass, respectively (Figure 4.11). The final nC_{60} retention profile indicates a maximum solid phase concentration of approximately 3.5 μg/g compared to a maximum value of approximately 10 μg/g for the analogous deposition experiments (Figure 4.9B, Experiments Ca-FS-3a,b). Overall, the sequential injection of DI water at increasing pH resulted in the recovery of more than 50% of deposited nC_{60} particles. These data are consistent with the behavior of C_{60} nanoparticles deposited on a silica-coated quartz surface, which were not released until the pH of DI rinse water was raised from 5.2 to 12.3 (Chen and Elimelech, 2006). These findings indicate that upon deposition, nC_{60} particles are strongly retained by porous media, consistent with a primary energy minimum interaction. In order for these deposited nC_{60} particles to be released, a substantial change in the zeta potential of either the sand surface or nC_{60} particle is required. These findings demonstrate that both the aggregation and transport of C_{60} nanoparticles in quartz sand are strongly dependent upon the electrolyte properties of the aqueous phase, and that once deposited, C_{60} nanoparticles are relatively stable.

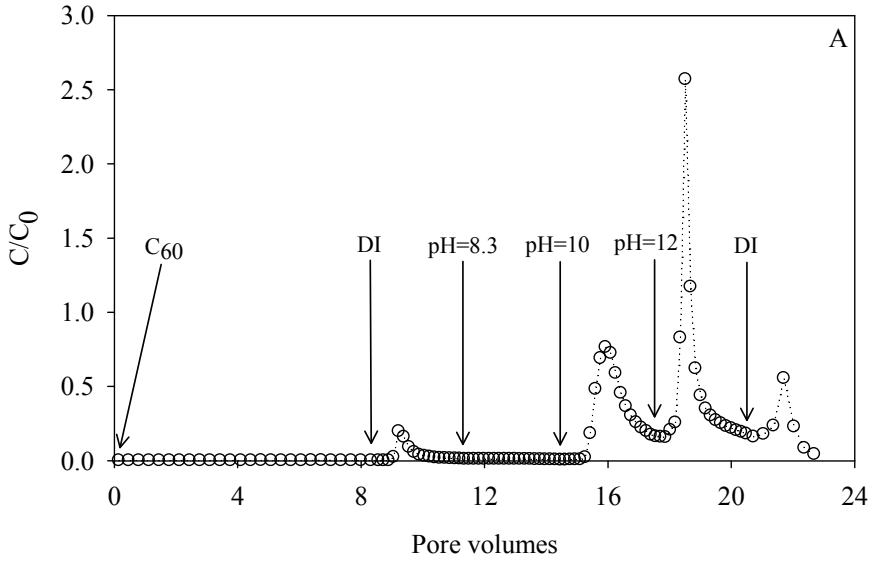

Figure 4.11. Effluent concentrations of nC_{60} after introducing an nC_{60} particle suspension containing 3.05 mM $CaCl_2$, followed by sequential injections of DI water at pH 7.0, 8.3, 10.0, 12.0 and 7.0.

4.3. MATHEMATICAL MODELING OF nC60 TRANSPORT AND RETENTION UNDER VARYING FLOW CONDITIONS

A modified filtration modeling approach, that incorporates nanoparticle attachment kinetics (k_{att}) and a maximum retention capacity (S_{max}), was developed and shown to successfully simulate measured nC_{60} transport and retention characteristics under a limited set of conditions (see Section 4.1). In this work, the ability of the mathematical model to predict nC_{60} transprot behavior is evaluated for a broader range of quartz sands and flow rates. In the model simulations, the hydrodynamic dispersion coefficient, D_H, was obtained independently by fitting the measured non-reactive tracer BTCs to a one-dimensional (1-D) form of the advective-dispersive reactive (ADR) transport equation (Toride et al., 1999). The attachment rate coefficient, k_{att}, and maximum retention capacity, S_{max}, were obtained by minimizing the sum of the squares residuals between measured and modeled effluent concentration and retention profile data using a nonlinear least-squares optimization function provided by MATLAB R2007b. The physical meaning of k_{att} and S_{max} values, obtained by fitting the model to measured nC_{60}effluent breakthrough curve and retention profile data, were then evaluated in the context of DLVO theory and mass flux in the vicinity of the grain surface.

4.3.1. EFFECTS OF FLOW RATE AND GRAIN SIZE ON nC_{60} TRANSPORT AND RETENTION

A total of nine nC_{60} transport experiments were conducted in four size fractions of Ottawa sand (20-30, 40-50, 80-100, and 100-140 mesh) and two pore-water (seepage) velocities (ca. 1 and 8 m/d) following the general experimental procedures described in Section 3.2.3. The influent concentration of the nC_{60} suspension was approximately 3.0 m/gL in all experiments, which was applied as a single pulse (3 PVs) injection, followed by the reintroduction of background electrolyte solution. All of the experiments were conducted in an aqueous solution consisting of 1.0 mM $CaCl_2$ and 0.065 mM $NaHCO_3$ as a pH buffer (pH 7.0, total ionic strength of 3.065 mM), with the exception of the last experiment listed in Table 4.3, which was conducted with DI water.

Effluent BTCs obtained for nC_{60} applied at the two flow rates in four size fractions of Ottawa sand are shown in Figures 4.12A and 4.12B. Here, it can be clearly seen that more nC_{60} passed through the column at the higher flow rate (Figure 4.12A), and that almost complete breakthrough was observed in 20-30 mesh Ottawa sand, whereas no breakthrough was observed in 100-140 mesh Ottawa sand. These trends were accentuated at the lower flow rate (Figure 4.12B). The corresponding retention profiles are shown in Figures 4.12C and 4.12D. The mass balance (sum of effluent and retained nC_{60} mass) ranged from 94 to 103% of the applied mass (Table 4.3).

4.3.2. NUMERICAL SIMULATIONS OF nC_{60} TRANSPORT AND RETENTION

The quality of the model fits are illustrated in Figures 4.12A and 4.12B, which present comparisons of measured (symbols) and simulated (solid lines) nC_{60} effluent BTCs for representative column experiments at two different flow velocities. Values of the two fitted parameters, k_{att} and S_{max}, and their standard errors (obtained from replicate column experiments) are listed in Table 4.3 for the various experimental conditions. At the higher flow rate, nC_{60} breakthrough was observed in all columns except those packed with 100-140 mesh Ottawa sand (d_{50} = 0.125 mm). At the lower flow rate (ca. 1 m/d) breakthrough of nC_{60} aggregates was only observed in the columns packed with 20-30 and 40-50 mesh Ottawa sand (d_{50} = 0.71 and 0.335 mm, respectively).

Table 4.3. Experiment conditions of nC_{60} transport studies conducted in water-saturated columns packed with four different size fractions of Ottawa sand.

Column[a]	d_c[b] (mm)	v_p[c] (m/d)	C_0[d] (mg/L)	Retained (%)	MB[e] (%)	k_{att}[f] (h^{-1})	α[g]	S_{max}[f] (µg/gsand)	λ[h] (%)	R-square
20-30F	0.710	8.34	3.00	14.3	100.3	3.21 (0.09)[i]	0.150 (0.005)	0.44 (0.06)	13.8 (0.48)	0.95
20-30S	0.710	1.10	3.34	26.2	98.3	1.54 (0.04)	0.142 (0.003)	0.83 (0.04)	12.8 (0.26)	0.95
40-50F	0.335	7.88	3.03	36.2	103.8	7.46 (0.36)	0.142 (0.004)	1.13 (0.18)	12.9 (0.42)	0.90
40-50S	0.335	1.03	3.01	91.0	101.3	3.98	0.140	3.27	12.1	0.94
80-100F	0.165	8.06	3.10	66.5	93.7	11.05 (1.92)	0.07 (0.01)	2.78 (0.14)	5.51 (1.03)	0.85
80-100S	0.165	1.04	2.95	100.0	93.8	11.40 (0.85)	0.128 (0.007)	6.41 (0.43)	11.5 (0.69)	0.98
100-140F	0.125	8.01	3.27	99.9	101.6	33.60 (1.70)	0.134 (0.004)	11.45 (0.14)	12.1 (0.45)	0.99
100-140S	0.125	1.03	3.26	99.9	92.6	18.0	0.13	13.99	11.8	0.99
100-140F0[j]	0.125	8.1	3.0	6.6	102.6	-	-	-	-	-

[a] Column name is defined by the sand mesh size and flow rate, F representing fast flow and S representing slow flow, [b] mean sand grain diameter, [c] pore water velocity, [d] influent n-C_{60} concentration, [e] mass balance, [f] averaged k_{att} and S_{max} values for replicate column experiments, [g] experimentally estimated collision efficiency factor, [h] fraction of favorable surface area, [i] values in parentheses represent the standard error of replicates, [j] conducted with DI water.

The mathematical model successfully captured the initial rise and subsequent sharp decline in effluent nC_{60} concentrations for all of the experimentally-measured BTCs (Figures 4.12A and 4.12B). Columns packed with coarser sands (20-30 and 40-50 mesh) generally exhibited a steeper initial rise, representing slower attachment, than columns packed with finer sands (80-100 and 100-140 mesh). This behavior was also reflected in the trend of the fitted attachment rate coefficient, k_{att}, which exhibited a marked decrease in value as the grain size increased, from 33.6 h^{-1} to 3.2 h^{-1} at the higher pore-water velocity (ca. 8 m/d) and from 18.0 h^{-1} to 1.54 h^{-1} at the lower pore-water velocity (ca. 1 m/d) (Figure 4.13A). For a particular size fraction of Ottawa sand, the value of k_{att} was larger at the higher pore-water velocity (ca. 8 m/d), with the exception of the column packed with 80-100 mesh Ottawa sand (Figure 4.13A).

The retention of nC_{60} aggregates, expressed as the retained nC_{60} mass per gram of dry soil, is presented in Figures 4.12C and 4.12D as a function of distance from the column inlet. Relatively flat retention profiles were observed for experiments in which effluent breakthrough occurred. For those experiments without breakthrough, solid-phase nC_{60} concentrations were generally higher close to the column inlet and then sharply declined to lower values near the column outlet, which indicates that S_{max} has not been reached throughout the entire column. At both pore-water velocities, the fitted value of S_{max} decreased rapidly with increasing mean grain size from 0.125

to 0.165 mm, and then steadily declined as the grain size was further increased to 0.71 mm. For a particular size fraction of Ottawa sand, the fitted value of S_{max} was greater at the lower pore-

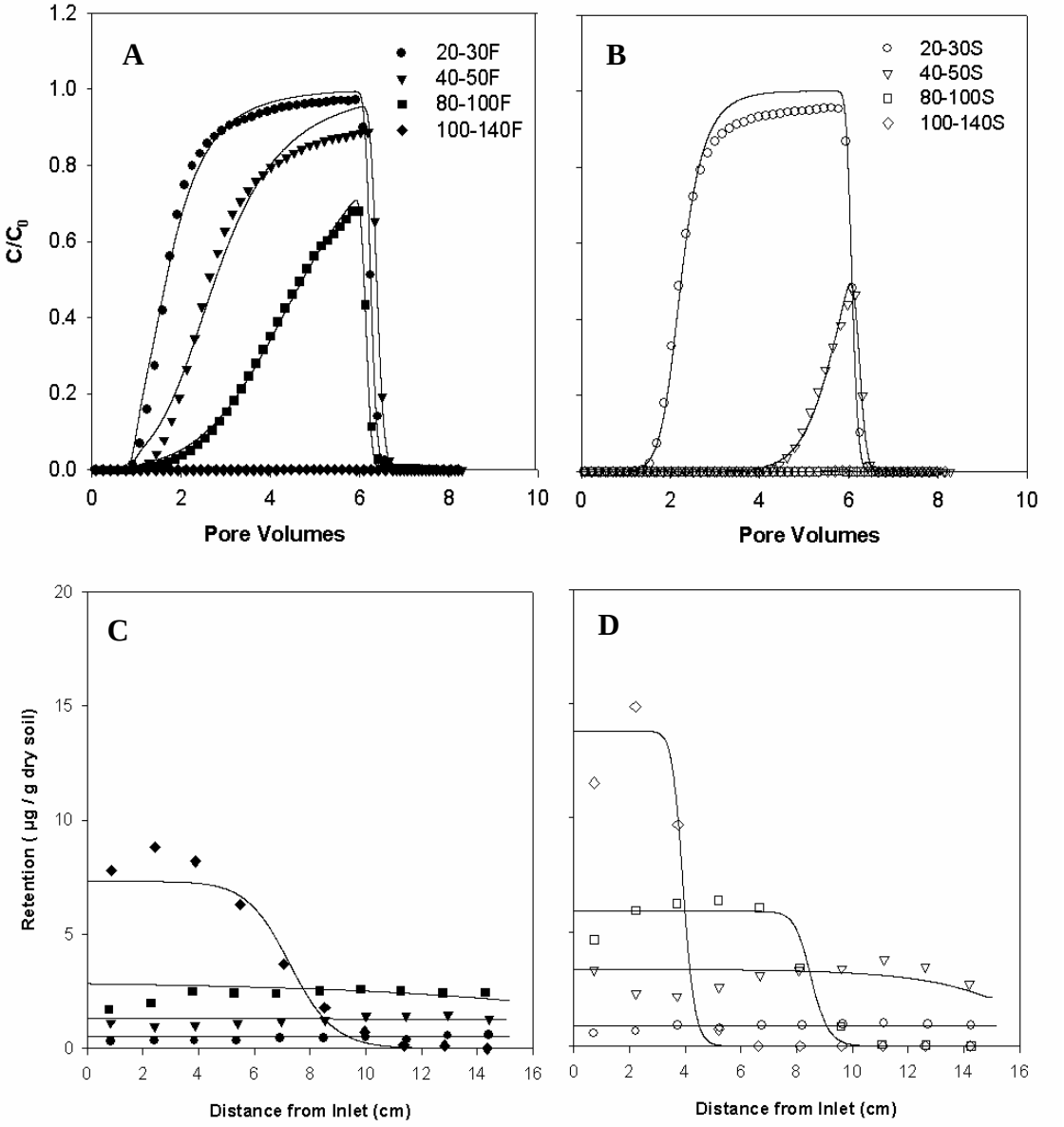

Figure 4.12. Measured and simulated breakthrough curves (A and B) and retention profiles (C and D) for representative nC_{60} transport experiments at pore-water velocities of ca. 8 m/d and 1 m/d in water-saturated columns packed with four different size fractions of Ottawa sand.

Aqueous nC_{60} suspensions contained 1.0 mM $CaCl_2$ as a background electrolyte, buffered to pH 7 with 0.065 M $NaHCO_3$.

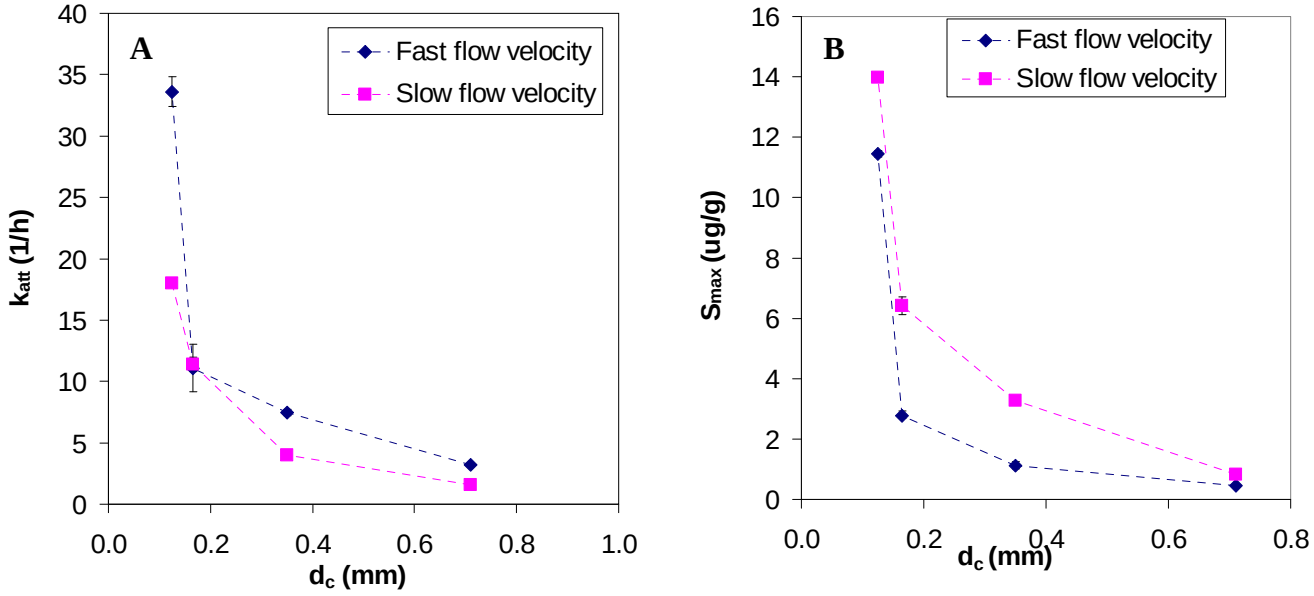

Figure 4.13. Comparison of simulated attachment rate coefficients, k_{att} (A), and maximum retention capacities, S_{max} (B) as a function of sand grain size at two flow velocities, ca. 1 m/d (square symbols) and 8 m/d (diamond symbols). Symbols indicate the average value obtained from duplicate experiments, while error bars represent the standard error of duplicate values.

water velocity (Figure 4.13B), consistent with the observed delay in initial breakthrough at the lower flow rate. For example, in columns packed with 40-50 mesh Ottawa sand, the initial breakthrough of nC_{60} occurred at ca. 1.3 PV at a pore-water velocity of 7.88 m/d; whereas, breakthrough did not occur until 4.4 PV at a pore-water velocity of 1.03 m/d.

4.3.3. Simulation of Maximum Retention Capacity

The value of S_{max} represents the maximum attainable particle concentration on the sand surface. Previous studies on the deposition of latex colloid particles (diameter of ca. 478 nm) on glass beads found that S_{max} was influenced by electrostatic interactions between the particle and collector surfaces (Johnson and Elimelech, 1995). More recent studies (Ko et al., 2000; Ko and Elimelich, 2000) have suggested that S_{max} is affected not only by electrostatic interactions but also hydrodynamic factors, such as flow velocity, particle size, collector size, and grain geometry. In this study, S_{max} was also found to decrease with increasing pore-water velocity and sand grain size for stable suspensions of nC_{60} aggregates (Figure 4.13B). Hydrodynamic interactions are often assessed using a particle Peclet number P_{ep} (Ko and Elimelich, 2000):

$$P_{ep} = \frac{v_p \, d_p}{D_l} \tag{4.2}$$

where, d_p is the particle diameter and D_l is the free liquid molecular diffusion coefficient. Hydrodynamic processes may be significant in the diffusion boundary layer if P_{ep} approaches 1.

The P_{ep} of nC_{60} is estimated to range from 0.4 to 3.2 for the experimental conditions employed in this study, based on a D_l of 4×10^{-12} m^2/s calculated from the Stokes-Einstein equation.

To further explore the relationship between S_{max} and hydrodynamic processes, an expression for the mass transport of nC_{60} toward a sand surface was derived by solving the advection-diffusion transport equation in the diffusion boundary layer. The diffusion boundary layer represents a very thin liquid layer, across which the particle concentration changes rapidly in the immediate vicinity of the sand surface (Levich, 1962) and within which molecular diffusion is typically taken into account. Assuming a perfect sink boundary condition at the sand particle surface ($C = 0$) and a constant concentration of nC_{60} aggregates in the bulk suspension ($C = C_0$), an analytical solution for the mass flux of nC_{60} (I_{diff}) within the diffusion boundary layer can be expressed as (Levich, 1962):

$$I_{diff} = 3.16 C_0 D_l^{2/3} v_p^{1/3} d_c^{4/3} \tag{4.3}$$

here d_c is the mean diameter of sand packed in the column. I_{diff} can be normalized to a dimensionless form by dividing eq 4.3 by $D_l C_0 d_M$:

$$\Lambda \sim P_e^{1/3} \frac{d_c}{d_M} \tag{4.4}$$

where d_M is the mean diameter of a medium sand (0.5 mm), and $P_e = \frac{v_p d_c}{D}$ is the Peclet number. An empirical correlation between the simulated retention capacity (S_{max}) and the normalized mass flux (Λ) for all nC_{60} column experiments (Table 4.3) was developed using SigmaPlot 9 (Systat Software, Inc). The resulting correlation,

$$S_{\max} = 25.39 \Lambda^{-1.23}, \quad R^2 = 0.95 \tag{4.5}$$

provided an excellent fit of S_{max} to the normalized mass flux Λ, as illustrated in Figure 4.9.

This finding supports the hypothesis that hydrodynamic processes are strongly correlated with the maximum retention capacity, and is consistent with the concept of a "shadow zone" as proposed by Ko and Elimelech (2000). The shadow zone refers to the down-gradient area on the grain surface where particle deposition is limited due to the interplay among particle size, approach velocity, and electrostatic forces. Higher pore-water velocity and larger sand grain size will create a larger shadow zone, corresponding to a reduced S_{max}. Conversely, a larger diffusion coefficient and lower pore-water velocity will result in greater diffusive transport and, hence, a smaller shadow zone. The correlation presented in eq 4.5 provides a means to relate these hydrodynamic effects to the magnitude of S_{max} for the experimental conditions considered herein.

4.3.4. Experimental and DLVO-Based Collision Efficiency Factors

According to clean-bed filtration theory, the particle attachment rate (k_{att}) can be related to the single collector efficiency (η_0) and the collision efficiency factor (α) by Yao et al., (1971):

$$k_{att} = \frac{3(1-\theta_w) v_p}{2 d_c} \alpha \eta_0 \tag{4.6}$$

Experimental collision efficiency factors can be calculated using eq 4.6 based the fitted k_{att}. As shown in Table 4.3, the α values are consistent for grain diameters ranging from 0.13 to 0.71

mm, which indicates that the attachment process itself is not sensitive to changes in physical properties, such as flow velocity and grain size.

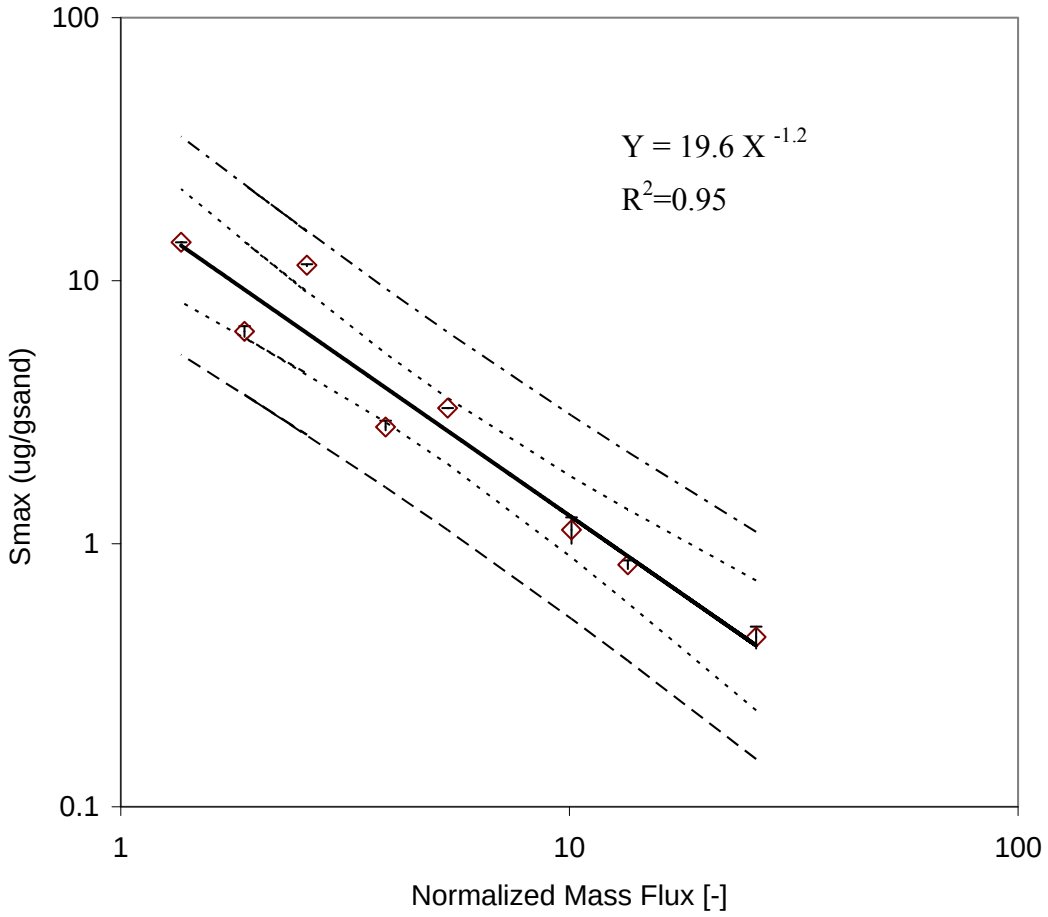

Figure 4.14. Relationship between the maximum retention capacity (S_{max}) and the normalized mass flux through diffusion boundary layer (Λ), where $\Lambda = P_e^{1/3}(d_c/d_m)$. Symbols indicate the averaged k_{att} values of duplicate experiments; error bars represents the standard error of duplicate values. The dashed lines and the center dashed line represent 95% confidence interval and 95% prediction interval generated by Sigmaplot.

A theoretical collision efficiency factor can be estimated based on the DLVO theory, which assumes that the total interaction energy (Φ) consists of the van der Waals attraction (Φ_v) and the electrical double layer (EDL) repulsion (Φ_{EDL}). Most approaches used to calculate these components assume that the separation distance between particles and the sand surface is less than 10% of the particle radius (Elimelech et al., 1995), which is not valid for the system considered herein due to the small size of nC_{60} aggregates (ca. 120 nm). Recently, Guzman et al. (2006) derived expressions for Φ_v and Φ_{EDL} using a surface element integration technique Bhattacharjee and Elimelech (1997), which is applicable to small particles when the separation distance is the same order-of-magnitude as the particle radius:

$$\Phi_v = -\frac{A_H}{6}\left[\frac{a}{h} + \frac{a}{h+2a} + \ln\left(\frac{h}{h+2a}\right)\right] \tag{4.7}$$

$$\Phi_{EDL} = \pi\varepsilon_0\varepsilon_r\kappa(\psi_s^2 + \psi_p^2)\cdot$$
$$\int_0^a \left(\begin{array}{l} -\coth[\kappa(h+a-a\sqrt{1-(r/a)^2}\,] + \coth[\kappa(h+a+a\sqrt{1-(r/a)^2}\,] \\ +\dfrac{2\psi_s\psi_p}{(\psi_s^2+\psi_p^2)}\{\csc h[\kappa(h+a-a\sqrt{1-(r/a)^2}\,] - \csc h[\kappa(h+a+a\sqrt{1-(r/a)^2}\,]\} \end{array} \right) rdr \quad , \tag{4.8}$$

$$\kappa^{-1} = \left(\frac{\varepsilon_0\varepsilon_r k_B T}{2e^2 1000 I_c N_A}\right)^{0.5}$$

Here, A_H is the Hamaker constant which was estimated to be 4.71×10^{-21} J for the fullerene-silica-water system based on a C_{60}-C_{60} Hamaker number of 7.5×10^{-20} J (Chen and Elimelich, 2006), a is the average radius of the nC_{60} aggregate (120 nm), h is the distance between the surfaces of the n-C_{60} aggregates and the sands, ε_0 is the permittivity of a vacuum (8.85×10^{-12} F/m), ε_r is the relative dielectric constant of water (78.5), κ is the inverse Debye length (0.18 1/nm), e is the elementary charge (1.60×10^{-19} C), I_c is the ionic strength of the suspension (0.003 M), N_A is the Avogadro constant (6.02×10^{23}), k_B is Boltzmann constant (1.38×10^{-23} m^2 kg s^{-2} K^{-1}), T is temperature [K], and ψ_s and ψ_p are the surface potentials of the particle and sand surface, respectively. Here, ψ_s is estimated from the measured nC_{60} zeta potential value in a 1 mM $CaCl_2$ solution, i.e. -24.3 mV, while ψ_p is estimated as -30 mV based on previously reported zeta potential values of Ottawa sand at a similar ionic strength (Kaya and Yukselen, 2005). An analysis suggested that the potential influence of the Stern layer thickness on the calculated surface potential was minimal under these experimental conditions (see Supporting Information).

As computed from eqs 4.7 and 4.8, the nC_{60}-sand surface energy profile exhibits a sizable energy barrier (Φ_{pr}= 39.4 kT) ca. 1.4 nm from the sand surface and a small secondary minimum attractive region (Φ_{sec} = -0.053 kT) ca. 46.7 nm from the sand surface). Based upon this profile, a theoretical collision efficiency factor (α) can be estimated from (Shen et al., 2007):

$$\alpha = 1 - \int_{\sqrt{\Phi_{sec}}}^{\sqrt{\Phi_{pr}+\Phi_{sec}}} \frac{4}{\pi^{1/2}} E^2 \exp(-E^2) dE \tag{4.9}$$

Here, E is the kinetic energy of the particle normalized by k_BT. Eq 4.9 assumes that attachment will occur if the kinetic energy of a particle is smaller than the attractive energy of the secondary minimum (Φ_{sec}), or larger than the sum of the primary energy barrier and the secondary minimum (i.e., $\Phi_{pr} + \Phi_{sec}$).

Calculations based on eq 4.9 result in a theoretical collision efficiency factor of 0.009, which is an order-of-magnitude smaller than α values of ca. 0.14 obtained based on the experimentally-derived k_{att} values. Further, theoretical α values were calculated using eq 4.9 and the DLVO interaction energy profile for two nC_{60} transport experiments presented in Section 4.1, where 1.0 mM NaCl was used as electrolyte solution rather than $CaCl_2$. Once again, the value of α (4.0×10^{-5}) calculated using eqs 4.7, 4.8 and 4.9 is orders-of-magnitude smaller than the experimentally-derived values of α (0.0045 and 0.0046, respectively) obtained from column studies conducted with 40-50 or 100-140 mesh Ottawa sand at a pore-water velocity of ca. 8 m/d. Possible explanations for the discrepancy between the theoretical and experimentally-derived

values of α, including physical straining, deposition in the secondary minimum, and primary minimum deposition due to surface charge heterogeneity, are considered below.

4.3.5. PHYSICAL STRAINING OF NANOPARTICLES

Physical straining occurs when the pore throat between grains is not sufficient to permit the passage of particles. Traditionally, straining is considered to be important when the ratio of particle diameter to the grain diameter is greater than 0.15 (Xu et al., 2006). Recent studies conducted with colloidal-size particles (diameter of 0.5 – 5.1 μm), however, suggest that straining can be observed at a much smaller size ratio of 0.002 (Bradford et al., 2005) or 0.008 (Xu et al., 2006). The ratio of nC_{60} aggregate to sand grain diameter for the experiments reported herein range from 2×10^{-4} to 9.0×10^{-4}, which is about one order-of-magnitude smaller than the reported threshold values for straining. In addition, the observed flat nC_{60} retention profiles in this study do not exhibit the hyper-exponential retention profiles often reported for straining. An additional experiment, conducted in 100-140 mesh Ottawa sand with DI water, resulted in only ca. 7% retention of the applied nC_{60} aggregates (Table 4.3). This low retention of nC_{60} observed in the absence of a background electrolyte provides further evidence that physical straining did not contribute significantly to nC_{60} retention.

4.3.6. DEPOSITION OF NANOPARTICLES IN THE SECONDARY MINIMUM

Particle deposition in the attractive secondary minimum region has been proposed as a possible mechanism for nC_{60} retention (Brant et al., 2005). However, calculation of the DLVO interaction energy profile in (Brant et al., 2005) was based on a C_{60}-C_{60} Hamaker constant 50×10^{-20} estimated from carbon nanotubes. This value has subsequently been found to be an order-of-magnitude larger than the C_{60} fullerene Hamaker constant 3.7×10^{-20} reported in Chen and Elimelich (2006). Calculation of DLVO interaction energies using the new Hamaker constant as presented herein, leads to a secondary minimum value that is one order-of-magnitude smaller than the value reported in Brant et al., (2005), which greatly reduces the potential importance of the secondary minimum for nC_{60} deposition. Furthermore, when columns packed with 100-140 mesh Ottawa sand were flushed with deionized (DI) water following nC_{60} aggregate deposition from a 1.0 mM $CaCl_2$ suspension, only 1% of the deposited nC_{60} aggregates was released (see Section 4.2.2). Because the introduction of DI water eliminates the secondary minimum energy well, this observed 1% release of retained nC_{60} reflects the contribution of the secondary minimum to nC_{60} deposition. Based on these two lines of evidence it is clear that the secondary minimum plays only a minor role in nC_{60} deposition for the experimental conditions considered here.

4.3.7. DEPOSITION OF NANOPARTICLES IN THE PRIMARY MINIMUM

Recent studies have demonstrated that approximately 50% of deposited nC_{60} in a column packed with 100-140 mesh Ottawa sand can be recovered when solution pH increases from 8.8 to 12 (see Section 4.2.2). This behavior is consistent with deposition associated with the primary minimum (Chen and Elimelech, 2006). The release of nC_{60} at high pH could be attributed to a decrease in the surface potential of either the nC_{60} or sand surface large enough to displace the nC_{60} from the primary minimum. The $CaCl_2$ solution used in this study has been shown to produce a lower zeta potential for the nC_{60} than that in a NaCl solution (Section 4.2.1), suggesting specific adsorption of Ca^{2+} complex to the nC_{60} surface (Chen and Elimelech, 2006). However, the measured zeta potential of nC_{60} increased from -68.9 ± 1.3 mV at pH 8.8 to -51.7 ± 0.5 mV at pH 12, leading to a reduced energy barrier. Thus, the change in nC_{60} surface potential

cannot explain the observed release at pH 12. On the other hand, Ottawa sand zeta potential has been reported to decrease dramatically from -30mV at pH 7 to -60 mV at pH 12 (Kaya and Yukselen, 2005), which is consistent with the observed release at high pH. The sharp decrease of sand surface zeta potential could be attributed to surface charge heterogeneity. The Ottawa sand used in this study was composed of 99.8% of SiO_2 and a small percentage of metal oxides (e.g. Fe_2O_3, Al_2O_3, TiO_2, CaO, MgO, Na_2O, and K_2O). In the presence of water, silica surfaces may become hydroxylated, with the surface acquiring charge through the ionization of hydroxyl groups. Research Zhdanov et al. (1987) has shown that hydroxyl groups on a silica surface are not identical and that their dissociative tendencies (acidities) may be vary due to differences in crystalline structure. The more acidic sites may dissociate completely, producing a negative charge, while the less acidic sites may not contribute to the negative charge due to their negligible dissociation (Vaidyanathan and Tien, 1991). In addition to differences in surface hydroxyl groups, the presence of metal oxides may also contribute to surface charge heterogeneity. At pH 12, the solution may be near or above the isoelectric point of the metal oxides (Rao and Finch, 2003), leading to a negative surface charge. Results of a previous transport study (Song et al., 1994) conducted with 50 nm diameter latex beads suggest that particle deposition onto a surface exhibiting a large primary energy barrier can be enhanced by as much as a factor of ten when the surface heterogeneous area increases from 0.1% to 3%.

Based upon the above analysis, surface charge heterogeneity represents the likeliest explanation for deviation of the observed collision efficiency factor from its theoretical value. The attachment of nC_{60} attributable to sand surface charge heterogeneity was not included in the previous DLVO interaction energy calculation, where a sand zeta potential representing the average electrokinetic charge of the heterogeneous sand grain was employed. To address this omission, a patch-wise model (Song et al., 1994) was used to explore the potential influence of sand surface charge heterogeneity on nC_{60} attachment. The patch-wise model assumes that surface sites of equal potential are grouped together in macroscopic patches, each of which can be treated as a homogeneous surface. Further, this model assumes that only one kind of favorable patch, on which all collisions will result in attachment (i.e. $\alpha = 1$), exists on an otherwise homogeneous surface that is unfavorable for particle deposition. For each experiment, the fraction of surface area that is favorable for attachment (λ) can then be estimated by minimizing the difference between the measured and calculated removal efficiency:

$$\lambda = \min \left| \eta_0 \alpha_{\exp} - (\lambda \eta_0 .1 + (1-\lambda)\eta_0 \alpha_{theory}) \right| \tag{4.10}$$

Here, the single collector efficiency (η_0) was estimated based on the correlation equation provided in Tufenkji and Elimelech (2004). The experimental attachment efficiency factor (α_{exp}) was calculated using eq 8 (Table 4.3), and α_{theory} is the theoretical attachment efficiency factor, calculated using eq 4.9. The resulting λ values are relatively constant, ranging from 11.5% to 13.8%, with the exception of one outlier point where the λ value is 5.5%, corresponding to the column experiment conducted with 80-100 mesh sand at a pore-water velocity of ca. 8 m/d. This λ value corresponds to the slightly lower k_{att} obtained for 80-100 mesh sand at a pore-water velocity of ca. 8 m/d (Figure 4.13A), which may have been due to the greater mass balance error in these experiments. The value of λ has been reported to range from 0.4% to 19.5% for glass beads at different ionic strengths, pH, and subject to different acid washing procedures (Song et al., 1994). Considering that the surface charge heterogeneity of Ottawa sand is likely larger than that of glass beads, the λ values calculated here are reasonable, and suggest that surface charge heterogeneity could explain the greater retention of nC_{60} on Ottawa sand surfaces compared to

glass beads. Modeling results presented here demonstrate that modifications to clean-bed filtration theory, consistent with the existence of shadow zones and surface charge heterogeneity, are required to capture nC_{60} transport and retention behavior under varying flow conditions in saturated Ottawa sands.

4.4. Effects of Stabilizing Agents on the Mobility of nC60 Nanoparticles

The purpose of this aspect of the project was to investigate effects of SRHA, SRFA or Tween 80 on nC_{60} transport and deposition in porous media. A novel experimental protocol for quantification of SRHA or SRFA and nC_{60} in their mixture was developed using high performance liquid chromatography (HPLC) and liquid-liquid extraction. A series of transport experiments of nC_{60} in the presence of tetrohydroforun (THF), SRHA or SRFA was conducted in one-dimensional columns packed with 40-50 mesh Ottawa sand. Effluent and solid phase concentration data were collected to construct nC_{60} effluent BTCs and retention profiles. Additionally, the effect of a nonionic surfactant, Tween 80, on nC60 transport behavior was assessed by introducing a suspension containing nC_{60} and Tween 80 (Tw80+C_{60}) and by injection of nC_{60} alone after a Tween 80 pre-flood (Tw80, C_{60}). The experimental conditions for the 11 column experiments are provided below in Table 4.4.

Table 4.4. Experimental conditions for nC_{60} column studies conducted in 40-50 mesh Ottawa sand with 0.001 M $CaCl_2$ as a background electrolyte.

Column Identifier	C_0 [a] (mg/L)	PW [b] (pv)	ξ [c] (mv)	d_a [d] (nm)	Retention [e] (%)	MB [f] (%)
C_{60}	4.7	5.0	-23.5	94.2	29.0	92.9
THF+C_{60}	4.7	5.0	-25.8	95.4	27.4	89.5
TW80+C_{60}-1	4.9	5.0	-15.1	92.5	0.0	103.1
TW80+C_{60}-2	5.0	5.0	-17.0	92.6	0.0	103.1
TW80, C_{60}-1	4.2	5.0	-24.2	90.6	6.3	96.1
TW80, C_{60}-2	4.3	5.0	-22.9	93.6	7.1	96.4
SRHA+C_{60}	3.9	5.0	-19.1	96.9	1.2	96.7
SRHA+C_{60}-eq	3.9	5.2	-15.6	104.0	2.9	99.4
SRFA+C_{60}	4.4	5.4	-23.6	95.6	0.8	100.1
SRHA	20.8	2.0	ND	ND	ND	90.7 *
SRFA	19.9	2.0	ND	ND	ND	93.2 *

[a] input concentration of nC_{60}, SRHA or SRFA. [b] pulse width. [c] average zeta potential of nC_{60}. [d] nC_{60} mean hydrodynamic diameter. [e] mass percentage of retained nC_{60}. [f] mass balance. * mass retained in column was not measured. ND not determined.

4.4.1. Effects of Tetrahydrofuran (THF) on nC_{60} Transport

Tetrahydrofuran (THF) was used in the preparation of nC_{60} suspensions because it provides a reproducible and easily controlled method to produce nC_{60} aggregates (Fortner et al., 2005). However, presence of THF residual and THF decay products, in particular γ-butyrolactone (GBL) raise concerns that the toxicity of nC_{60}, in part, results from byproducts produced during preparations (Lyon et al., 2006; Andrievsky et al., 2005; Brant et al., 2005). Henry et al. (2007) detected ca. 158 ppm of GBL in an nC_{60} suspension, prepared using the similar method here, and found that GBL was responsible for nC_{60} toxicity. In the our experiments, the concentration of THF residual in nC60 stock suspension was determined to be 1.57 mg/L two days after

preparation, with no detectable levels of GBL, suggesting that repeating evaporation process three times greatly reduced THF level and oxidation of THF.

Effluent BTCs and retention profiles of nC_{60} in presence of 44.5 mg/L THF transported through 40-50 mesh water saturated Ottawa sands are shown in Figure 4.15A and 4.15B, respectively. To form a basis for comparison, a transport experiment was conducted with nC_{60} alone, in which the concentration of THF residual was less than 0.8 mg/L (Figure 4.15). Consistent with the data shown in Sections 4.1 and 4.2, the shape of the nC_{60} BTC was asymmetric, with a gradual ascent to a maximum value, followed by a sharp drop at the end of pulse injection. When THF was present in nC_{60} suspension at a concentration of 44.5 mg/L, both BTCs and retention profiles were identical to those of nC_{60} alone. These findings suggest that presence of THF at concentrations up to 44.5 mg/L does not alter to nC_{60} transport and deposition in 40-50 mesh Ottawa sand.

THF and GBL concentrations in effluent samples were monitored, and GBL levels were found to be below detection limit. The effluent BTC obtained for THF was symmetric, with sharp ascent and descent at ca. 1 and 6 PV, respectively. Once THF appeared in the column effluent, a plateau developed with an average THF relative concentration (C/C_0) of 0.89, indicting less than 11% of input THF was retained by the Ottawa sand. The retention of THF was mainly attributed to adsorption of THF by Ottawa sand and association of THF molecules with retained nC_{60} (Fortner et al., 2005; Brant et al., 2005). Since the presence of THF at a concentration of 44.5 mg/L did not impact nC_{60} transport and deposition, the influence of THF at concentrations below the detection limit (< 0.8 mg/L) was considered to be negligible, and thus, THF concentrations were not monitored in subsequent experiments.

4.4.2. Effects of Tween 80 on nC60 Transport and Deposition Processes

To investigate effects of a representative stabilizing agent, Tween 80, on nC_{60} transport and deposition a series of column experiments was conducted that involved (a) adding Tween 80 to the nC_{60} suspension or (b) pre-flushing the column with a Tween 80 solution prior to the injection of an nC_{60} suspension. The resulting effluent BTCs obtained for nC_{60} in presence of 1,000 mg/L Tween 80 and in Tween 80-coated Ottawa sand are shown in Figure 4.16A. When nC_{60} suspension was premixed with Tween 80 (TW80+C_{60}-1,2), nC_{60} BTCs were identical to that of a non-reactive tracer, with a C/C_0 plateau value of 1.0. When nC_{60} alone was introduced into 40-50 mesh Ottawa sand pre-treated with 5 PVs of a 1,000 mg/L Tween 80 solution followed by 3 PV elution of background electrolyte solution, relative n*C60* concentrations (C/C_0) rapidly increased to a maximum value of 0.9 after 1 PV and declined steadily during the pulse injection, and then dropped sharply when background electrolyte solution was reintroduced into the column. Consistent with the C/C_0 plateau value of 1.0, nC_{60} retention by the solid phase was not measurable when 1,000 mg/L Tween 80 was present in the nC_{60} input suspensions (Figure 4.16B). When nC_{60} was delivered to Tween 80-coated sand, the nC_{60} retention profiled decreased hypo-exponentially with distance from the column inlet, with more than 77% of the total retained nC_{60} mass present in the first 5 cm of the column (Figure 14.6B).

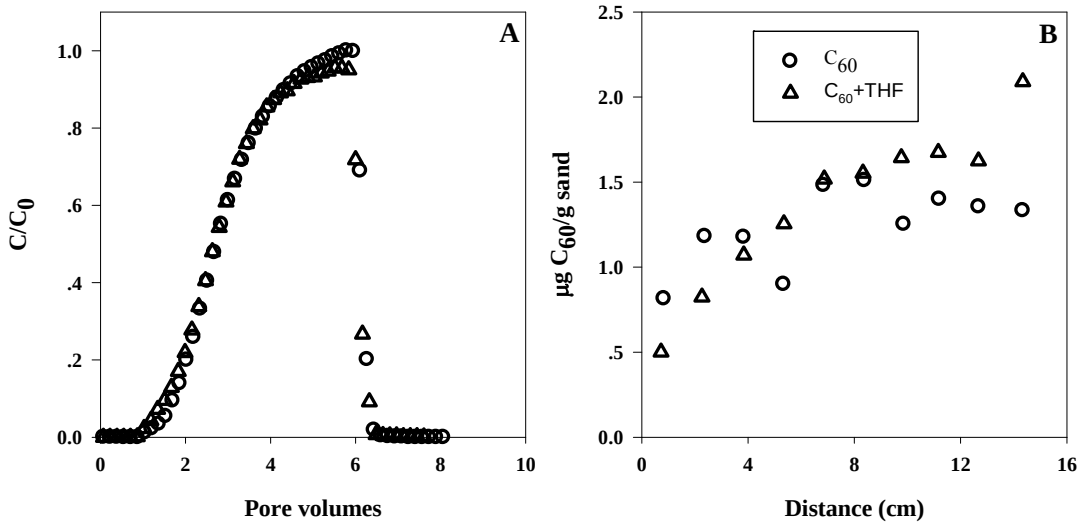

Figure 4.15. Effluent breakthrough curves (A) and retention profiles (B) for pulse injections of nC_{60} and nC_{60} + THF (44.5 mg/L) in columns packed with 40-50 Ottawa sand.

While effluent nC_{60} concentrations were monitored, concentrations of Tween 80 in effluent samples (Exp. TW80+C_{60}-1,2) were determined to assess Tween 80 transport and adsorption in 40-50 mesh Ottawa sand (Figure 4.16C). The BTC for Tween 80 alone (no nC_{60}) is shown in Figure 4.16C as a reference. In these experiments, Tween 80 appeared in effluent at ca. 1 PV and then their effluent concentration sharply increased to influent concentration, followed by a sharp drop at the conclusion of the pulse injection. Relative Tween 80 effluent concentrations in nC_{60} transport experiments (e.g., TW80+C_{60}-1,2) scattered around 1.0, with a t-test of data points between 1.57 and 5.89 PV indicating that these plateau concentrations were not significantly different. These data suggest that relative loss of Tween 80 to the solid phase via sorption was minimal, compared the introduced mass.

When pre-mixed with Tween 80, the nC_{60} aggregates were stabilized in suspension, which could be due to adsorption of Tween 80 onto the C60 aggregates and solubilization of C60 within Tween 80 micelles. The concentration of Tween 80 (1,000 mg/L) was approximately 75 times greater than the critical micelle concentration (CMC, 13 mg/L). In the presence of 1,000 mg/L Tween 80, the measured zeta potential of C_{60} nanoparticles was significantly reduction (i.e., less negative) as shown in Table 4.4. A comparison of nC_{60} BTCs in the presence of Tween 80 to those obtained in the absence of Tween 80 clearly demonstrate that Tween 80 enhanced nC_{60} transport. The zeta potential of Ottawa sands coated with Tween 80 were determined to be -30.3 mV, while a slight higher zeta potential (-31.4 mV) was obtained for uncoated Ottawa sands. Based on Derjaguin-Landau-Verwey-Overbeek (DLVO) theory, the interaction energy was calculated following approaches proposed by Guzman et al., (2006), where the Hamaker constant was 4.71×10^{-21} J for the fullerene-silica-water system (Section 4.3), average particle radius was 46.3 nm, and surface potentials of nC_{60} particle and Ottawa sand were approximated to measured zeta potentials. The resulting energy profile exhibited a primary barrier of approximately ~ 25 kT at ~ 2.5 nm from sand grain surface. The lower energy barrier calculated in the presence of Tween 80 should result in higher nC_{60} retention when 1,000 mg/L Tween 80 was premixed with the nC_{60} influent suspension (e.g., TW80+C_{60}-1,2). However, the opposite was observed (i.e., greater nC60 transport when mixed with Tween 80), suggesting that steric

repulsions were introduced by the coated Tween 80, rather than physicochemical interactions, were primarily responsible for the enhancement of nC_{60} transport in the presence of Tween 80.

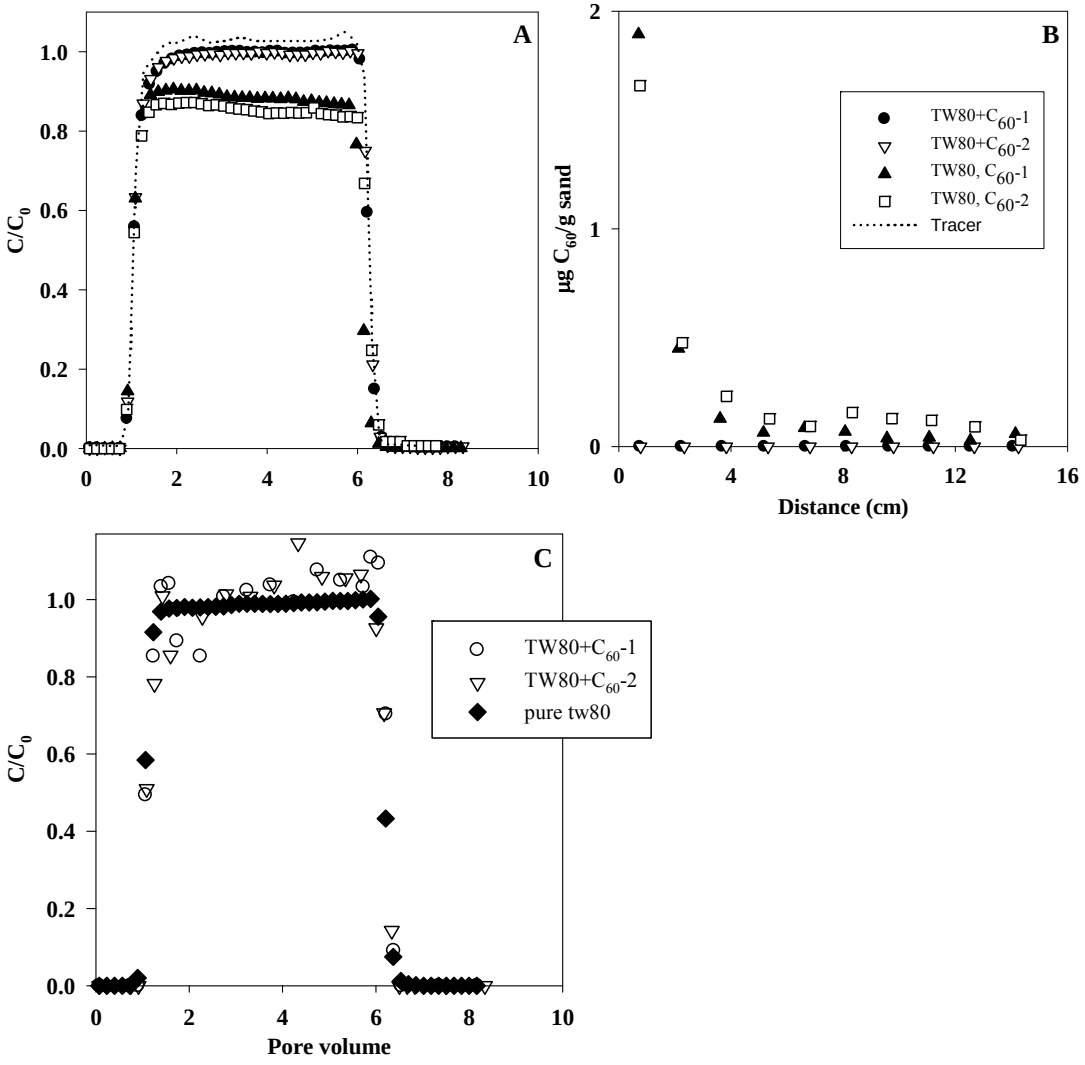

Figure 4.16. nC_{60} effluent breakthrough curves (A) and retention profiles (B) for a 5 PV injection of either a nC_{60} + Tween 80 (1,000 mg/L) mixture or Tween 80 (1000 mg/) pre-flood followed by 5 PV injection of nC_{60} in 40-50 mesh Ottawa sand. Effluent Tween 80 concentrations (C) during pulse injection of nC_{60} + Tween 80 (1,000 mg/L)and Tween 80 alone (solid symbols) for a pulse injection of Tween 80 (1,000 mg/L).

Effluent BTCs and retention profiles obtained for nC_{60} alone applied to Tween 80-coated Ottawa sands exhibited two important trends; slightly declined effluent concentration "plateau" and hypo-exponentially decreasing retention profiles, respectively (Figures. 4.16A and 4.16B). Conceptually, the slight decline in the plateau of the nC_{60} BTCs could imply the occurrence of filter ripening (Ginn et al., 2002), in which attached particles further serve as collectors causing more particle deposition near the injection point. However, data reported in Sections 4.1 and 4.2 indicate unfavorable interactions between nC_{60} and nC_{60} or Ottawa sand with 1 mM $CaCl_2$ as a background electrolyte, suggesting that ripening processes do not contribute to nC_{60} deposition.

Hypo-exponential decay of retained particles has been reported in colloid transport studies and attributed to varying particle attachment rates (k_{att}) with traveling distance (Tufenkji et al., 2004; Li et al., 2004).

4.4.3. MATHEMATICAL MODELING OF nC60 TRANSPORT AND DEPOSITION IN THE PRESENCE OF TWEEN 80

Careful inspection of the measured nC_{60} retention profiles revealed that the maximum nC_{60} concentrations on solid phases were consistent with retention capacity (e.g. 1.98 μg/g), which suggests that the retention capacity of nC_{60} was reached near the column inlet. Thus, it is hypothesized that non-exponentially decaying retention profiles in Tween 80 coated Ottawa sands are the result of gradual desorption of Tween 80 from the sand surface. Based on this conceptual model, a numerical model was developed that coupled the sorption-desorption of Tween 80 with the attachment-detachment of nC_{60}, described mathematically as follows:

$$\frac{\partial C_1}{\partial t} + \frac{\rho_b}{\theta_w}\frac{\partial S_1}{\partial t} = D_H \frac{\partial^2 C_1}{\partial x^2} - v_p \frac{\partial C_1}{\partial x} \tag{4.11}$$

$$\frac{\partial S_1}{\partial t} = \frac{Qb}{(1+bC_1)^2}\frac{\partial C_1}{\partial t} \tag{4.12}$$

$$\frac{\partial C_2}{\partial t} + \frac{\rho_b}{\theta_w}\frac{\partial S_2}{\partial t} = D_H \frac{\partial^2 C_2}{\partial x^2} - v_p \frac{\partial C_2}{\partial x} \tag{4.13}$$

$$\frac{\rho_b}{\theta_w}\frac{\partial S_2}{\partial t} = f\left(1 - \frac{S_2}{S_{2\max}}\right)C_2 \tag{4.14}$$

where, C_1 and C_2 are concentrations of Tween 80 and nC_{60} in aqueous phase, respectively, S_1 and S_2 are concentrations of attached Tween 80 and nC_{60}, respectively, t is time, x is the travel distance, ρ_b is the soil bulk density, θ_w is the volumetric water content, D_H is the hydrodynamic dispersion coefficient, v_p is the pore-water velocity, S_{2max} is the retention capacity of nC_{60} on 40-50 mesh Ottawa sand, Q is the maximum sorption capacity of Tween 80 on Ottawa sand in a Langmuir form, and b is the sorption constant. Additionally, the term f is a function of S_1 and expressed as follow,

$$f = k_{att}\left(1 - \frac{S_1}{TwS}\right) \tag{4.15}$$

where, TwS is a fitting parameter. D_H was obtained from fitting tracer BTC using the CXTFIT ver. 2.0 (Toride et al., 1999), k_{att} and S_{2max} were obtained from Section 4.1 data, and Q and b were obtained from sorption isotherm of Tween 80 to Ottawa sands. As illustrated in Figure 4.17 below, the resulting numerical model was able to accurately capture the measured nC_{60} BTCs and retention profiles.

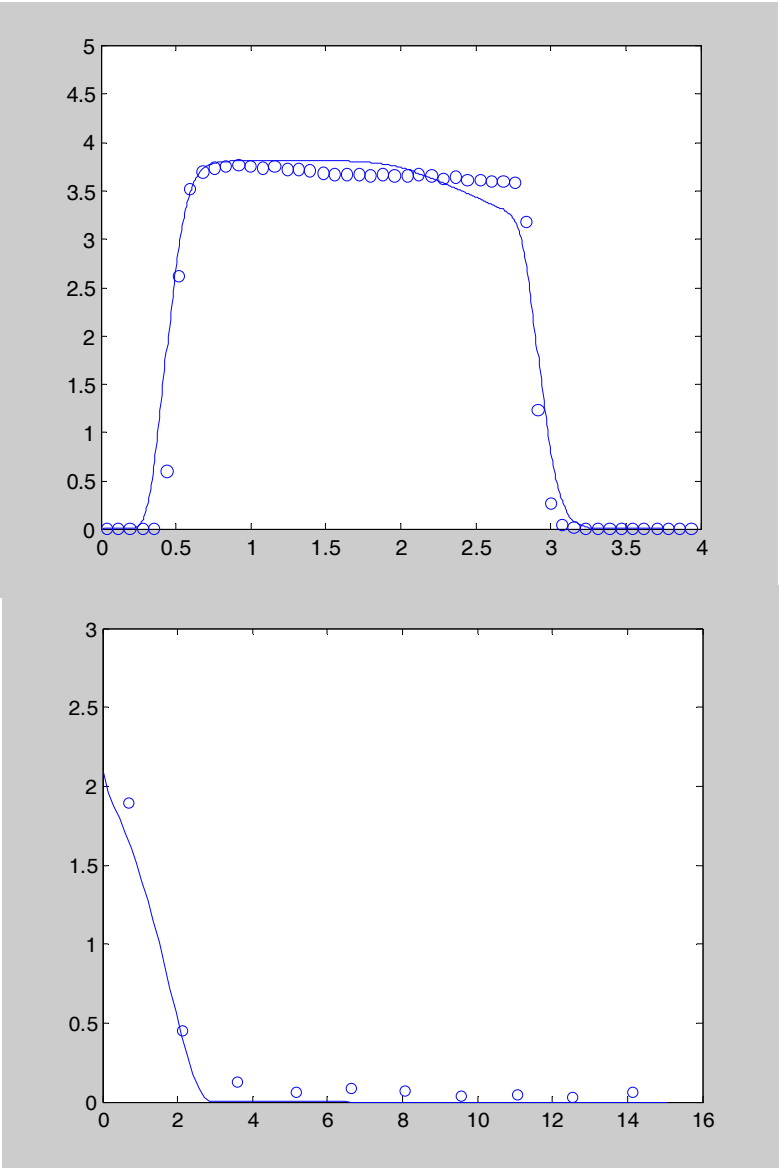

Figure 4.17. Simulated nC_{60} breakthrough curve (A) and retention profile (B) by modeling Tween 80 desorption and nC_{60} attachment simultaneously.

4.4.4. Effect of Natural Organic Matter (NOM) on nC60 Transport and Deposition

Effluent BTCs and retention profiles of nC_{60} premixed with 20 mg C/L SRHA or SRFA in water saturated 40-50 mesh Ottawa sands are shown in Figure 4.18. Regardless of input suspension, the presence of 20 mg C/L SRHA or SRFA resulted in breakthrough of nC_{60} through sand columns at ca. 1 PV, which was 0.5 PV earlier than that in absence of stabilizing agents (e.g., Exp. C_{60}). Once nC_{60} broke through sand columns, relative nC_{60} concentrations increased rapidly to a plateau relative concentration value of greater than 0.98, followed by sharp descent that approached zero at the end of pulse injection. When equilibrium between nC_{60} and SRHA

was achieved prior to pulse injections, the nC_{60} BTC exhibited identical characteristics to those at nonequilibrium status (e.g., Exp. SRHA+C_{60}). These findings suggest that the presence of SRHA or SRFA enhanced nC_{60} transport in saturated 40-50 mesh Ottawa sands.

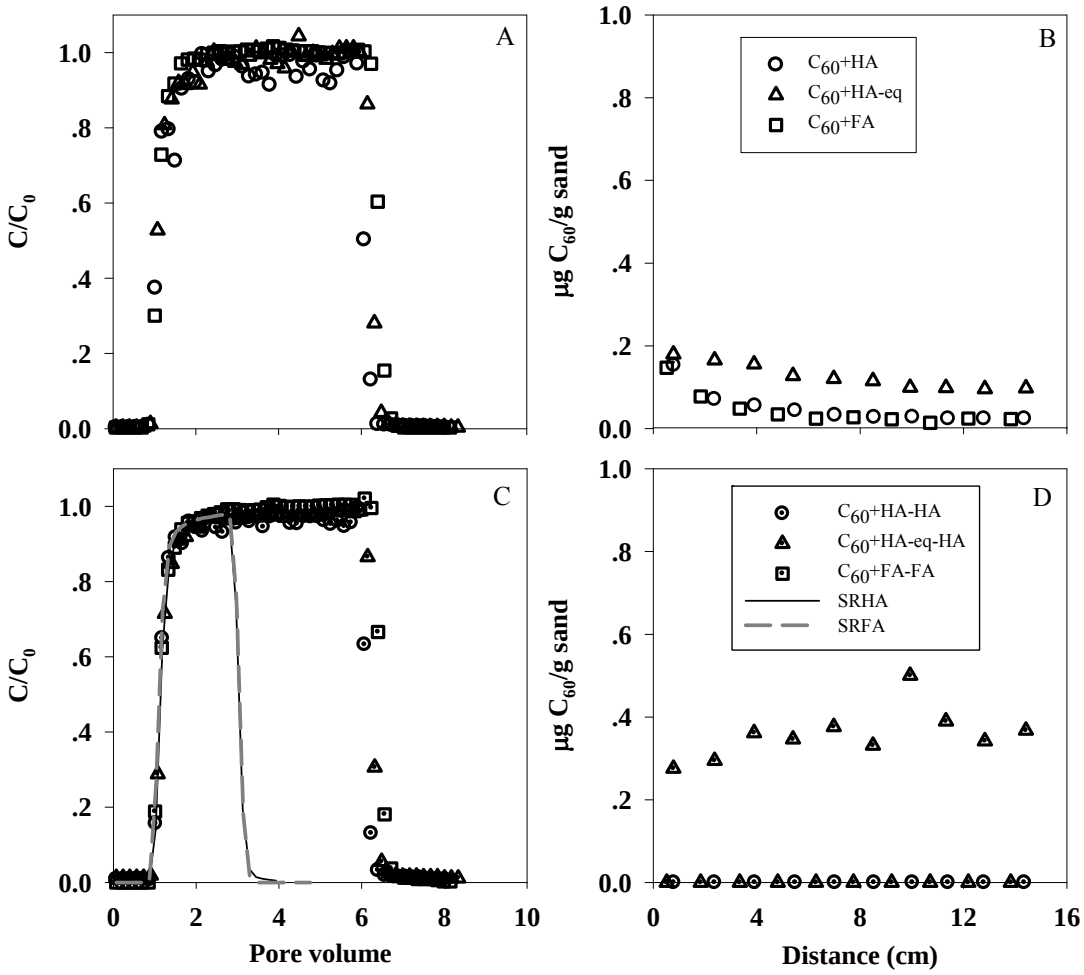

Figure 4.18. Effluent breakthrough curves (A and C) and retention profiles (B and D) of nC_{60} (open symbols) and extracted SRHA or SRFA (open symbols with central dot) for 5 pore volume injections of nC_{60} + SRHA (20 mg C/L) or SRFA (20 mg C/L) suspensions in water-saturated columns packed with 40-50 mesh Ottawa sand. Solid and dash lines denote effluent breakthrough curves for two pore volume injections of SRHA (20 mg C/L) and SRFA in 40-50 Ottawa sand, respectively.

At the conclusion of each transport experiment, the column was sectioned into ten 1.5 cm increments, from which retained nC_{60} and SRHA or SRFA were extracted through sonication and liquid-liquid extraction processes. The resulting retention profiles of nC_{60} are shown in Figure 4B. Generally, concentrations of nC_{60} retained by the solid phase decreased gradually with travel distance. While the retention profile of nC_{60} in the presence of SRFA was not discernable from that in the presence of non-equilibrated SRHA, allowing the nC_{60} and SRHA suspension to reach equilibrium resulted in slightly higher nC_{60} retention (Figure 4.18B). Regardless of equilibration time of the input suspensions, the maximum solid phase

concentrations of nC_{60} were identical (0.18 μg/g) and occurred near column inlets. A total mass balanced of greater than 96% was obtained for all column experiments, reflecting the accuracy of nC_{60} extraction and quantification protocols.

Although NOM has been considered as a natural surfactant, the SRHA/SRFA concentration (20 mg C/L) used in this study was well below reported CMCs, which range from 500 and 15,000 mg C/L for humic and fulvic acids, respectively (Hayase and Tsubota. 1983). In addition, no detectable aggregates with diameter greater than 0.6 nm (DLS detection limit) formed in pure SRHA/SRFA solutions at the concentration of 20 mg C/L. Thus, nC_{60} suspensions were stabilized by SRHA/SRFA through surface coatings rather than micellar solubilization. Electrophoresis measurements showed that adsorption of SRHA molecules onto nC_{60} particles reduced (less negative) the zeta potential of nC_{60} from ca. -23 to -16 mV, while change of nC_{60} zeta potential after mixing with SRFA was not discernable (Table 4.4).

In studies of colloid (e.g., latex microsphere) transport, the reduction of particle deposition in presence of natural organic matter has been attributed to increasing electrostatic repulsion and steric interaction (Franchi and O'Melia, 2003). In the presence of 20 mg C/L SRHA at equilibrium, an energy barrier with 18 kT was found at ca. 2.5 nm, while a relative higher barrier (ca. 36 kT) was observed at ca. 1.5 nm in presence of SRFA at the same concentration. In Section 4.1, we been demonstrated that nC_{60} particles are able to overcome energy barrier as high as 35 kT and are attached on quartz sand at the primary energy minimum. Assuming that the presence of SRHA does not change the particle energy (e.g., kinetic energy), nC_{60} particles should be able to overcome an energy barrier (18 kT), resulting in more nC_{60} retention, which is not consistent with observations. While in the presence of SRFA, the sizable energy barrier slightly increased compared to that in absence of stabilizing agents, which was consistent with the reduction of nC_{60} retention. However, steric repulsion between coated humic or fulvic acids on nC_{60} and quartz sands are dominant when surface distance of particle and sand is less than 1.5 or 2 nm. Here, we hypothesize that steric interactions prevented attachment of nC_{60} particles and, in turn, enhanced nC_{60} transport. Although first energy barriers became less than or comparable to that of pure nC_{60}-sand system, a small secondary minimum was still observed at distance of ca. 44 and 50 nm in presence of SRHA and SRFA, respectively. These secondary minima contributed to the relative small amount of nC_{60} retained under these conditions (see Table 4.4).

4.5. TRANSPORT AND RETENTION OF nC60 IN NATURAL SOILS

The transport and retention of nC_{60} aggregates in natural soils was investigated in a series of column experiments performed with Appling and Webster soils, which contain 0.75 and 3.35% organic carbon (OC) by weight, respectively. Aqueous nC_{60} suspensions were applied to each water-saturated soil column as a pulse injection, ranging in duration from 5 to 65 PVs. The concentration of nC_{60} in the column effluent was measured continuously, while the solid phase was destructively sampled at the conclusion of each experiments to construct nC_{60} breakthrough curves (BTCs) and retention profiles, respectively. To assess the potential effects of a natural stabilizing agent on nC_{60} transport, additional column experiments were conducted with 20 mg C/L Suwannee River humic acid (SRHA). The experimental data were simulated using a one-dimensional (1D) particle transport model designed (a) to evaluate the applicability of traditional clean-bed filtration and (b) to explore the utility of alternative descriptions of particle retention to

simulate the observed nC_{60} transport behavior. The experimental conditions of the six column studies are summarized below in Table 4.5.

Table 4.5. Experimental conditions for nC_{60} transport studies conducted in Appling (AP) and Webster (WB) soils with 1×10^{-3} M $CaCl_2$ and 5×10^{-5} M $NaHCO_3$.

Column Identifier	Soil	C_0[a] (mg/L)	PW[b] (pv)	ξ[c] (mV)	d_a[d] (nm)	MB[e] (%)	Retention (%)
AP-C_{60}-5pv	Appling	4.31	5.0	-23.4	110	94.8	100
AP-C_{60}-32pv	Appling	4.37	32.5	-22.9	121	101.9	100
AP-C_{60}-65pv	Appling	4.26	64.7	-25.3	98.6	102.4	100
AP-C_{60}SRHA-5pv	Appling	4.69	5.0	-19.6	98.5	99.0	100
WB-C_{60}-5pv-I	Webster	4.42	4.8	-23.9	99.9	85.0	100
WB-C_{60}-5pv-II	Webster	4.41	4.8	-23.9	99.9	89.1	100

[a] input concentration of nC_{60}. [b] pulse width. [c] zeta potential of nC_{60}. [d] nC_{60} mean hydrodynamic diameter. [e] mass balance.

4.5.1. TRANSPORT AND RETENTION OF nC60 IN NATURAL SOILS

For the initial set of column experiments, a 5-PV pulse (ca. 100 mL) of nC_{60} suspension was introduced into water-saturated Appling or Webster soil, followed by at least three PVs of an nC_{60}-free solution containing only background electrolytes. However, nC_{60} aggregates were not detected in the effluent of columns packed with either soil. The complete absence of breakthrough indicates that the transport behavior of nC_{60} in these soils was distinct from that reported previously for relatively "clean" porous media. In water-saturated glass beads, for example, nC_{60} breakthrough was consistently observed, and constant or slightly increasing effluent concentrations were achieved after continuous injection of less than 3 PVs of the influent suspension (Brant et al., 2005a; Espinasse et al., 2007; Lecoanet and Wiesner, 2004; Lecoanet et al., 2004). Those breakthrough data served as the basis for the application of traditional clean-bed colloid filtration theory by these investigators to describe nC_{60} transport, despite the lack of solid-phase retention data and mass balance closure.

To further assess the capacity of the natural soils to retain nC_{60}, the duration of the applied pulse was increased from 5 to 32.5 PVs, and then to 64.7 PVs, in separate Appling soil column experiments. Even after these prolonged delivery events, nC_{60} aggregates were not detected in any of the effluent samples from these of column experiments. The complete absence of nC_{60} breakthrough in Webster and Appling soils contrasts with the findings of Cheng et al. (2005), where nC_{60} appeared in the effluent of a column packed with Lula soil after only 3.2 PVs. The observed differences in nC_{60} transport behavior among these natural soils mirror differences in OC and clay size fraction content, which were approximately 3 and 12 times greater, and 5 and 17 times greater in Appling and Webster soils, respectively, compared to Lula soil (2 % clay size fraction, 0.3 % OC).

Following each column experiment, the soil was removed in ca. 1-cm increments and extracted to directly measure the amount and spatial distribution of nC_{60} retained in each column experiment. Mass balance recoveries for Appling soil ranged from 95 to 102%, while those of

Webster soil ranged from 85 to 89% (Table 4.5). The lower mass balance recoveries obtained for Webster soil were attributed to the higher OC content of this soil, which resulted in lower solid-phase extraction efficiency. Measured nC_{60} retention profiles for Appling and Webster soil columns, expressed as a solid phase concentration versus the distance from the column inlet, are shown in Figure 4.19.

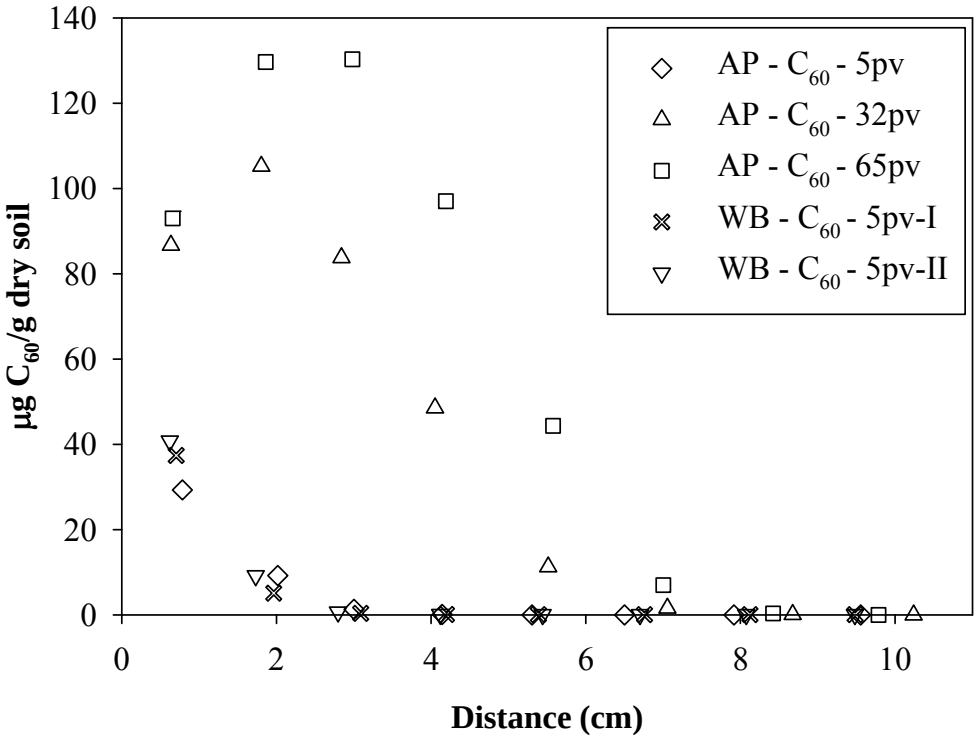

Figure 4.19. Retention profiles of nC_{60} aggregates in water-saturated columns packed with Appling (AP) or Webster (WB) soil. Influent nC_{60} suspensions were prepared in absence of stabilizing agents and contained 1.0 mM $CaCl_2$, applied at a pore-water velocity of 8 m/d. No nC_{60} breakthrough was observed in these experiments.

After a 5 PV pulse of nC_{60} suspension was introduced into either Appling or Webster soil, the spatial distributions of retained nC_{60} were similar, with a maximum concentration of approximately 38 µg nC_{60}/g dry soil 1 cm of the column inlet, decreasing rapidly to non-detect levels ca. 4 cm from the column inlet (Figure 4.19). The similarities in magnitude and shape of the nC_{60} retention profiles obtained for Appling and Webster soil suggest that organic matter did not strongly influence nC_{60} retention under these conditions since the OC content of Webster soil is ca 4.5 times greater than that of Appling soil.

When the volume of nC_{60} suspension applied to Appling soil was increased to 32.5 PV, the nC_{60} retention profile exhibited a maximum concentration of 110 µg nC_{60}/g dry soil ca. 2 cm from the column inlet, and decreased linearly to non-detect levels ca. 7 cm from the column inlet. Upon doubling the applied pulse width to 64.7 PVs, the solid-phase concentration reached a plateau of approximately 130 µg nC_{60}/g dry soil between 2 and 3 cm from the column inlet, and then decreased to non-detect levels ca. 8.5 cm from the column inlet. The general features of nC_{60} retention profiles observed in Appling soil, including the solid-phase concentration plateau,

are similar to those observed in Ottawa sands (see Section 4.3), and suggest that a maximum retention capacity of ca. 130 μg nC_{60}/g dry Appling soil was reached under these experimental conditions.

Most natural soils possess a broad distribution of particle sizes, as well as natural organic matter, which typically results in complex flow pathways, narrow pore throats and dead-end pores. Thus, the possibility exists that physical straining contributed to the sizable retention of nC_{60} observed in Appling and Webster soils. Physical straining occurs when particles are trapped at the intersection of two solid-water interfaces (grain-to-grain contacts), and often leads to pore throat blockage and extensive particle accumulation near the injection point. Experimentally, the straining process translates to almost complete particle retention at the column inlet, followed by a sharp decline in particle retention with distance (Bradford et al., 2002). In quartz sands and glass beads, physical straining has been found to be an important retention mechanism when the ratio of the particle diameter (d_p) to soil grain or "collector" diameter (d_c) exceeds a value of 0.0016 (Shen et al., 2008). Based upon an nC_{60} aggregate diameter of 100 nm and mean grain diameter of 0.220 μm for Appling soil, estimated from the measured particle size distribution, a d_p:d_c ratio of 0.00045 is obtained, suggesting that straining did not play a significantly role in nC_{60} retention. This empirical estimate is consistent with the absence of pronounced nC_{60} accumulation near column inlet (i.e., < 1 cm) and the development of a concentration plateau as the number of applied PVs increased.

To further explore the nC_{60} retention process, the fractional coverage (θ) of the solid phase by nC_{60} aggregates was estimated using the approach of Tufenkji et al. (2003), which assumes irreversible and monolayer particle deposition,

$$\theta = \frac{\pi a^2 r_c q N_0 \int_0^t (1 - N/N_0)dt}{3L(1-\theta_w)} \tag{4.16}$$

where, a and r_c are the mean radii of the nanoparticle and the soil grains, respectively, q is the superficial or Darcy velocity, N_0 is the influent concentration expressed as the number of nC_{60} aggregates per volume, and N is the effluent nC_{60} aggregate concentration. The estimated surface coverage of Appling soil by nC_{60} aggregates increased linearly, from 0.0036% to 0.05%, as the amount of nC_{60} introduced into the column increased from 5 to 65 PVs, respectively. This analysis indicates that even after 65 PVs, the nC_{60} surface coverage of Appling soil represented a relatively small fraction of the mineral surface area, consistent with the hypothesis that physical straining did not contribute significantly to nC_{60} retention.

Prior studies have shown that electrostatic forces play a critical role in the transport and retention of nC_{60} aggregates in glass beads and quartz sands (e.g., Espinasse et al., 2007, Section 4.1). To estimate the magnitude of electrostatic interactions between nC_{60} aggregates and soil grains, the streaming potential of Appling soil was measured and converted to a zeta potential of -5.68 ± 0.55 mV. This value is approximately 5.5 times lower than the zeta potential obtained for 40-50 mesh Ottawa sand (-31.44 ± 0.05 mV) using the same measurement technique. Based on the Derjaguin-Landau-Verwey-Overbeek (DLVO) sphere-plate model, an energy barrier of ca. 1.7 kT and secondary energy minimum of ca. -0.08 kT were calculated for the nC_{60}-Appling soil system (Figure 4.20). This primary energy barrier (1.7 kT) is 20 times less than that determined for nC_{60}-Ottawa sand system under the same solution conditions (1 mM $CaCl_2$), consistent with the greater nC_{60} retention observed in Appling soil compared to 40-50 mesh

Ottawa sand (see Section 4.1). The potential contribution of hydrophobic interactions to the energy profile, calculated based on the approach of Van Oss et al. (1986) and Yoon et al. (1997), were found to be minimal.

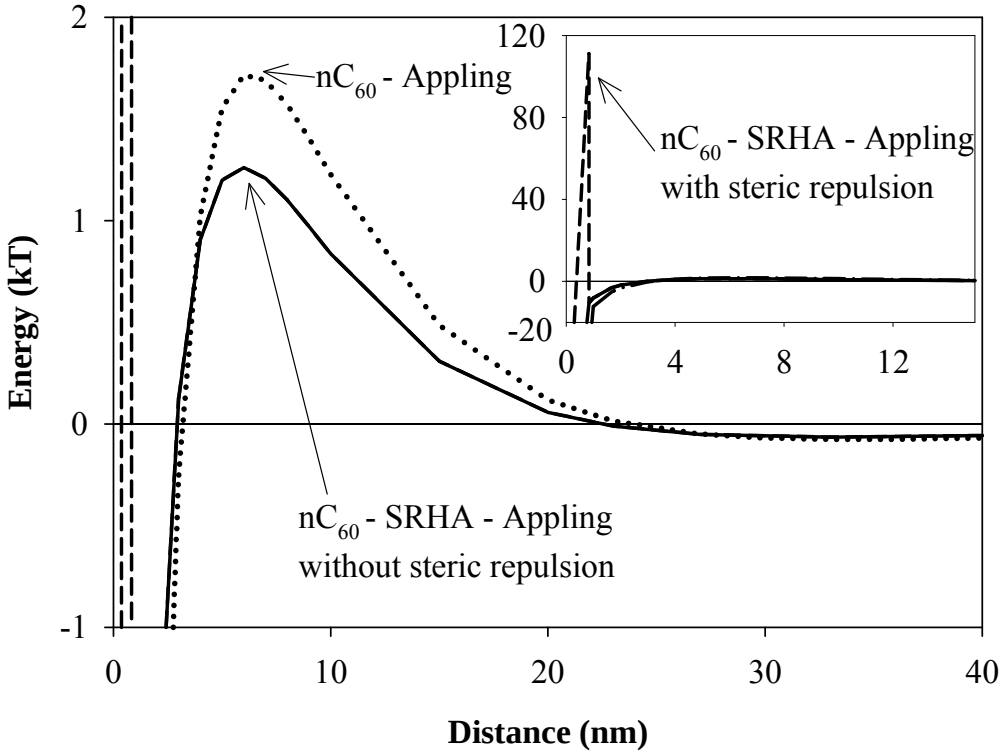

Figure 4.20. Interaction energy profiles for Appling soil and nC_{60} aggregates in the absence (dotted line) and presence of Suwannee River Humic Acid (SRHA). The dashed and solid lines represent the total interaction energy for an nC_{60}-SRHA-Appling system with and without steric repulsion forces, respectively. The energy profiles (dashed and solid lines) are identical when the separation distance is greater than 0.83 nm.

4.5.2. Effects of Humic Acid on nC60 in Natural Soils

To evaluate the potential effects of a stabilizing agent on nC_{60} transport and retention in natural soil, a pulse (e.g., 5 PVs) of nC_{60} suspension, premixed with SRHA, was introduced into an Appling soil column. In the presence of 20 mg C/L of SRHA, nC_{60} aggregates were not detected in column effluent, similar to the experiment conducted in the absence of SRHA. The corresponding nC_{60} retention profile (Figure 4.21) shows a maximum solid phase nC_{60} concentration of ca. 15 μg/g dry soil near the column inlet, which decreased steadily to non-detect levels at a distance of ca. 8 cm. Compared to the retention profile obtained in the absence of SRHA (AP-C_{60}-5pv), the nC_{60} travel distance, defined as the column length where the nC_{60} soil phase concentration approaches zero, increased from 3 cm to 8.5 cm. These findings clearly

demonstrate that the presence of SRHA at concentration of 20 mg C/L facilitated nC_{60} transport through Appling soil even though column breakthrough was not observed.

In the presence of 20 mg C/L of SRHA, the zeta potential of nC_{60} (Table 4.5), determined immediately after the input suspension preparation, was reduced to -19.6±0.3 mV from an average value of -23.9 mV in the absence of SRHA. Based on DLVO theory, the lower nC_{60} zeta potential would result in a lower primary energy barrier, which should result in greater nC_{60} retention and shorter travel distance than in the absence of SRHA, contrary to the observed results (Figure 4.21). One possible explanation for this discrepancy is the absence of a steric repulsive interaction term in conventional DLVO theory. When adsorbed molecules (e.g., SRHA on the surface of nC_{60} aggregates) are compressed during particle approach to a solid surface, steric repulsion occurs due to the increase of local osmotic pressure and entropy loss (Degennes, 1987; Elimelech et al., 1995). To illustrate the potential effect of adsorbed SRHA on nC_{60} deposition, the steric repulsive energy of an nC_{60}-SRHA-sand system was calculated based on equations of Tiraferri and Sethi (2009), assuming an SRHA volume fraction of 0.1, average molecular weight of 3,000 Da (Hong and Elimelech, 1997), average density of 1.45 g/mL (Relan et al., 1984), and linear addition of all interaction energies. The SRHA layer thickness on nC_{60} was estimated to be 0.83 nm based on the difference between the DLS-measured hydrodynamic radii of nC_{60} aggregates in the presence and absence of 20 mg C/L SRHA. The total interaction energy, including van de Waals attractive energy, electronic double layer repulsive energy, and steric repulsive energy, for this scenario are plotted in Figure 4.20. The resulting energy profile exhibited a sizeable primary energy barrier, with a maximum value of ca. 110 kT. While these calculations are applicable to a quartz sand system, the general magnitude suggests that steric repulsive energy associated with SRHA adsorbed on nC_{60} aggregates contributed to the enhanced migration of nC_{60} aggregates in Appling soil in the presence of 20 mg C/L of SRHA.

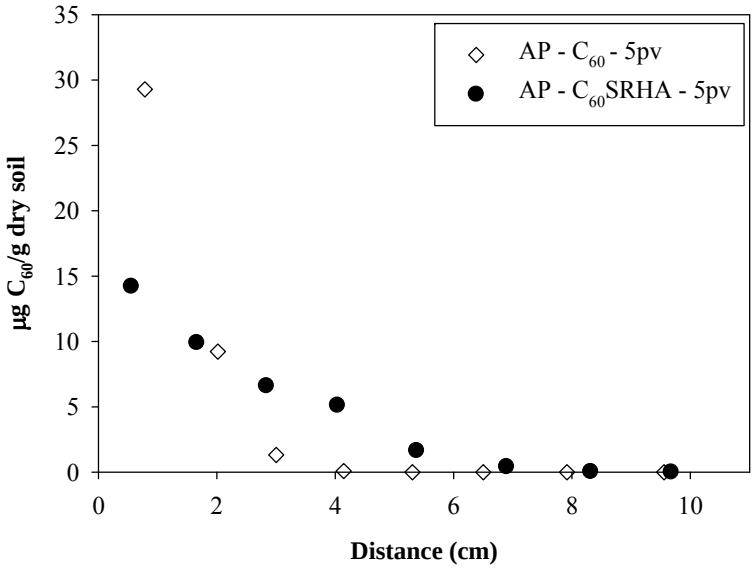

Figure 4.21. Retention profiles obtained for nC_{60} in the absence (◊) and presence (●) of 20 mg C/L Suwannee River Humic Acid (SRHA) in columns packed with Appling soil following a 5 pore volume (5-PV) pulse injection. No breakthrough of nC_{60} or SRHA was observed.

4.5.3. MATHEMATICAL MODELING OF nC60 RETENTION IN NATURAL SOILS

Initially, the model based on traditional clean-bed filtration theory (CBFT) was used to simulate the experimental retention profiles obtained for nC_{60} in Appling soil at 5, 32.5 and 64.7 PVs (Figure 4.22A). Here, the attachment rate (k_{att}) was obtained by minimizing the sum of the squares residuals between measured and modeled retention profile data using a nonlinear, least-squares optimization function provided by MATLAB R2008b. As illustrated in Figure 4.22A, simulations based on clean-bed filtration capture the general trends observed nC_{60} retention profile at 5 PVs. Discrepancies between the simulated and observed nC_{60} retention profiles in Appling soil, however, are readily apparent for applications of 32.5 and 64.7 PVs of nC_{60} suspension. In particular, the model predicts substantially higher retained nC_{60} concentrations (>400 μg/g) at the column inlet compared to the observed values, which did not exceed 140 μg/g. These findings illustrate one of the main limitations of the traditional clean-bed filtration model, where the influence of attached particles on the subsequent deposition is ignored. For relatively small injected pulse widths or at early time, the solid surface will be relatively clean, and the influence of resident particles on the subsequent attachment process is negligible, consistent with comparisons of model predictions and measured deposition at 5 PVs. The influence of attached particles becomes increasingly important as more nC_{60} mass is applied and more favorable attachment sites are occupied, resulting in the divergence between the traditional clean-bed filtration model and experimental data at higher loadings. It should be noted, however, that the model did not capture the lower retention data points nearest to the column inlet (ca. 1 cm) for the 32.5 and 64.7 PV injections. Additional experiments are underway to verify this finding and investigate factors that may have contributed to this observation.

The measured nC_{60} retention profile data for Appling and Webster soils were then simulated using the maximum retention capacity model (see Sections 4.1 and 4.3), which also accounts for rate-limited retention processes (Figure 4.23). The model successfully captured the non-exponential decay and the concentration plateau of retention profiles observed for the 5, 32.5, and 64.7 PV of nC_{60} injection cases. The improved performance of the maximum retention capacity model is consistent with the existence of a maximum retention capacity of Appling soil. As more nC_{60} aggregates attach, the number of available favorable deposition sites will be reduced, which limits subsequent deposition. Optimization of the mathematical model fit to the experimental data yielded a maximum retention capacity of 140 μg/g for Appling soil, which was consistent with the value observed experimentally. This S_{max} value is about 12 times greater than the value of 11.45 μg/g obtained for 100-140 mesh Ottawa sand under similar experimental conditions (Section 4.3). The higher S_{max} value reflects the more heterogeneous Appling soil surfaces, where more favorable attachment sites may be associated with surface charge heterogeneity, surface roughness, and the presence of clay minerals and organic matter. The fitted attachment rate was 50 1/h, which is 77 times larger than that obtained for Lula soil (Cheng et al., 2005), and greater than the value obtained for 100-140 mesh Ottawa sand (33.6 1/h) at the similar flow rate. The attachment rate is directly related to the attachment efficiency factor α, which depends upon the interaction energy between nC_{60} aggregates and solid surfaces The high attachment rate obtained here qualitatively agrees with calculations of a much lower energy barrier (ca. 1.7 kT) between nC_{60}-Appling soil than nC_{60}-Ottawa sand (ca. 39 kT) under identical solution conditions (1mM $CaCl_2$) (Section 4.3).

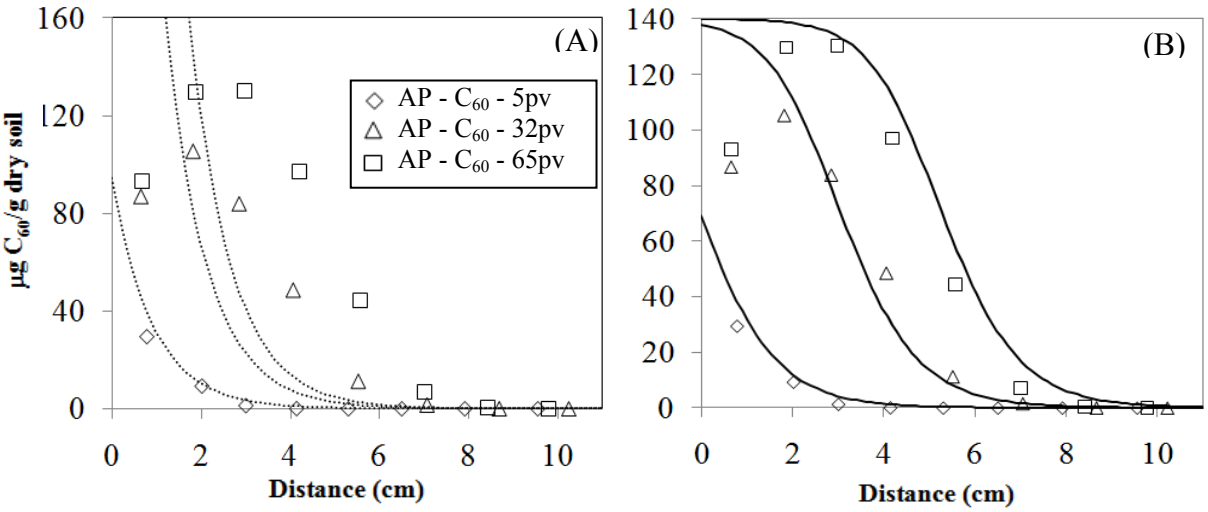

Figure 4.22. Comparison of measured and simulated retention profiles for nC_{60} in water-saturated columns packed with Appling soil obtained using (A) traditional clean-bed filtration model and (B) maximum retention capacity model.

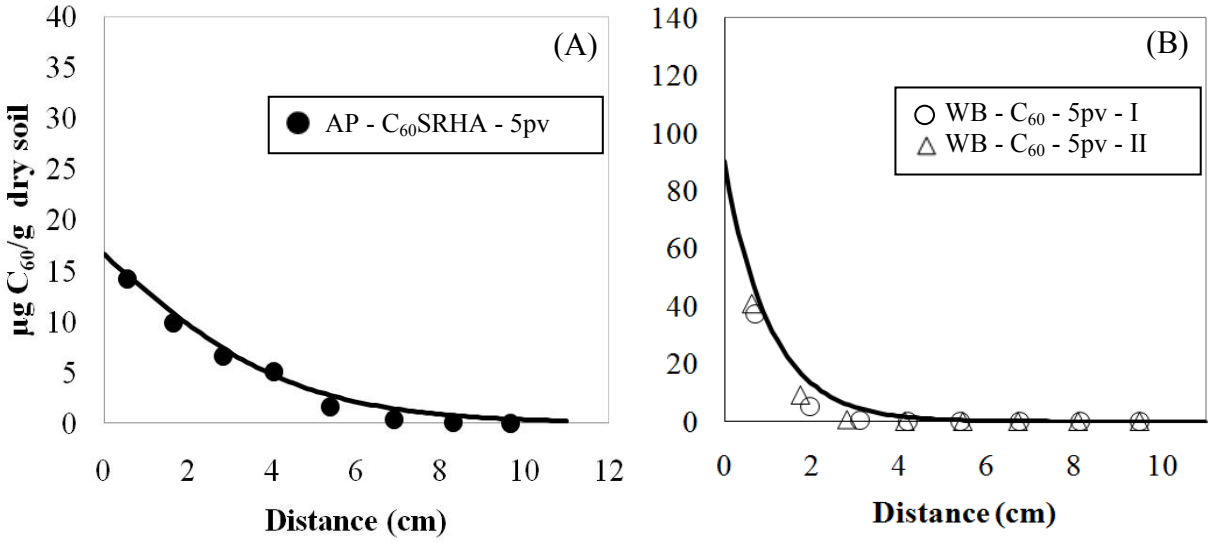

Figure 4.23. Simulated retention profiles obtained using a maximum retention model for (A) nC_{60} alone in water-saturated Webster soil and (B) a mixture of nC_{60}-and Suwannee River Humic Acid (SRHA) in water-saturated Appling soil.

Applying the same model to the transport of the nC_{60} suspension containing SRHA in Appling soil resulted in a reduced k_{att} value of 18 1/h, and S_{max} value of 30 µg/g (Figure 4.23A). The smaller k_{att} and S_{max} values, obtained in the presence of SRHA, result in greater travel distances, consistent with the experimental observations. The smaller k_{att} value could be due to the existence of steric repulsions, which would tend to increase the energy barrier between nC_{60}-

Appling soil as discussed above. The smaller S_{max} value may be due to the adsorption of SRHA on mineral surfaces and association with soil organic matter, which could act to block favorable deposition sites. For nC_{60} transport in Webster soil (Figure 4.23B), the fitted k_{att} value of 55 1/h was similar to that obtained for Appling soil, while the S_{max} approached a value of 2×10^5 μg/g. Based on Eq. 5, when S_{max} is very large or approaches infinity, the maximum retention capacity model reduces to the traditional clean-bead filtration model.

4.6. MULTI-WALLED CARBON NANOTUBE (MWCNT) TRANSPORT AND RETENTION

The objectives of this study were to (a) investigate the effects of tube length on the transport and retention of MWCNTs in water-saturated quartz sand and (b) to directly assess the role of physical straining based on measured MWCNT retention profiles. Understanding such effects is challenging because of the difficulty of preparing aqueous-stable MWCNT samples with distinct size ranges using conventional methods such as acid digestion. Therefore, a novel chemical modification method, which disperses CNTs in water with minimal structural damage, was employed to prepare aqueous MWCNT suspensions from three initial manufacture-reported tube lengths: 0.5-2, 10-30, and 100 μm. A series of one-dimensional (1-D) transport experiments were conducted at two input concentrations (10 and 90 mg/L) in a water-saturated quartz sand to obtain MWCNT effluent BTCs and solid-phase retention profiles. The experimental data were simulated using mathematical models based on traditional CBFT, corrected for rod-shaped particles, or modified to account for first-order particle attachment and physical straining. The experimental conditions of the column transport experiments are summarized below in Table 4.6.

Table 4.6. Experimental conditions and simulation parameters for transport and retention of with three size fractions of MWCNTs conducted in 1-D columns packed with 40-50 mesh (d_{50} = 0.36 mm) quartz sand and operated at a pore-water velocity of 7.6 m/day.

Column Identifier[a]	PW[b]	IS[c]	EM[d]	Ret[e]	MB[f]	k_{att}	95%CL[g]	k_{str}	95%CL	MMB[h]
	PV	mM	μm·cm/V·s	%	%	$\times 10^{-7}$ min^{-1}	$\times 10^{-4}$	$\times 10^{-2}$ min^{-1}	$\times 10^{-3}$	%
Short-10	4.5	6	-3.0±0.1	1.0	90.6	1.78	±7.76	0.456	±5.09	99.9
Medium-10-1	5.1	6	-3.4±0.1	2.9	95.6	1.89	±10.9	1.40	±7.18	99.9
Medium-10-2	5.0	6	-3.3±0.1	3.0	93.9	8.47	±11.1	1.52	±7.36	99.8
Long-10	4.4	6	-3.8±0.0	20.3	99.3	3.09	±28.1	9.27	±19.6	99.3
Short-90	5.0	75	-2.6±0.1	0.2	98.7	4.88	±3.70	0.375	±2.60	99.8
Medium-90-1	5.0	75	-3.0±0.2	6.7	98.9	3.27	±46.7	3.43	±32.2	99.8
Medium-90-2	6.3	75	-3.1±0.0	6.7	98.7	515	±43.0	3.55	±28.2	99.5
Long-90	4.4	75	-3.2±0.1	23.7	102.1	32.5	±136	12.3	±84.5	95.4

[a] Short, medium and long designation corresponds to MWCNTs with measured length ranges of 0.2-1.3, 0.2-7.5, and 0.2-21.4 μm, 10 and 90 designation indicates the input concentration, and 1 and 2 represent replicate columns. [b] pulse width. [c] ionic strength. [d] electrophoretic mobility. [e] retention. [f] overall mass balance, equal to the sum of curve areas underneath BTC and retention profile divided by total input mass. [g] 95% confidence limit. [h] overall mass balance in modeling

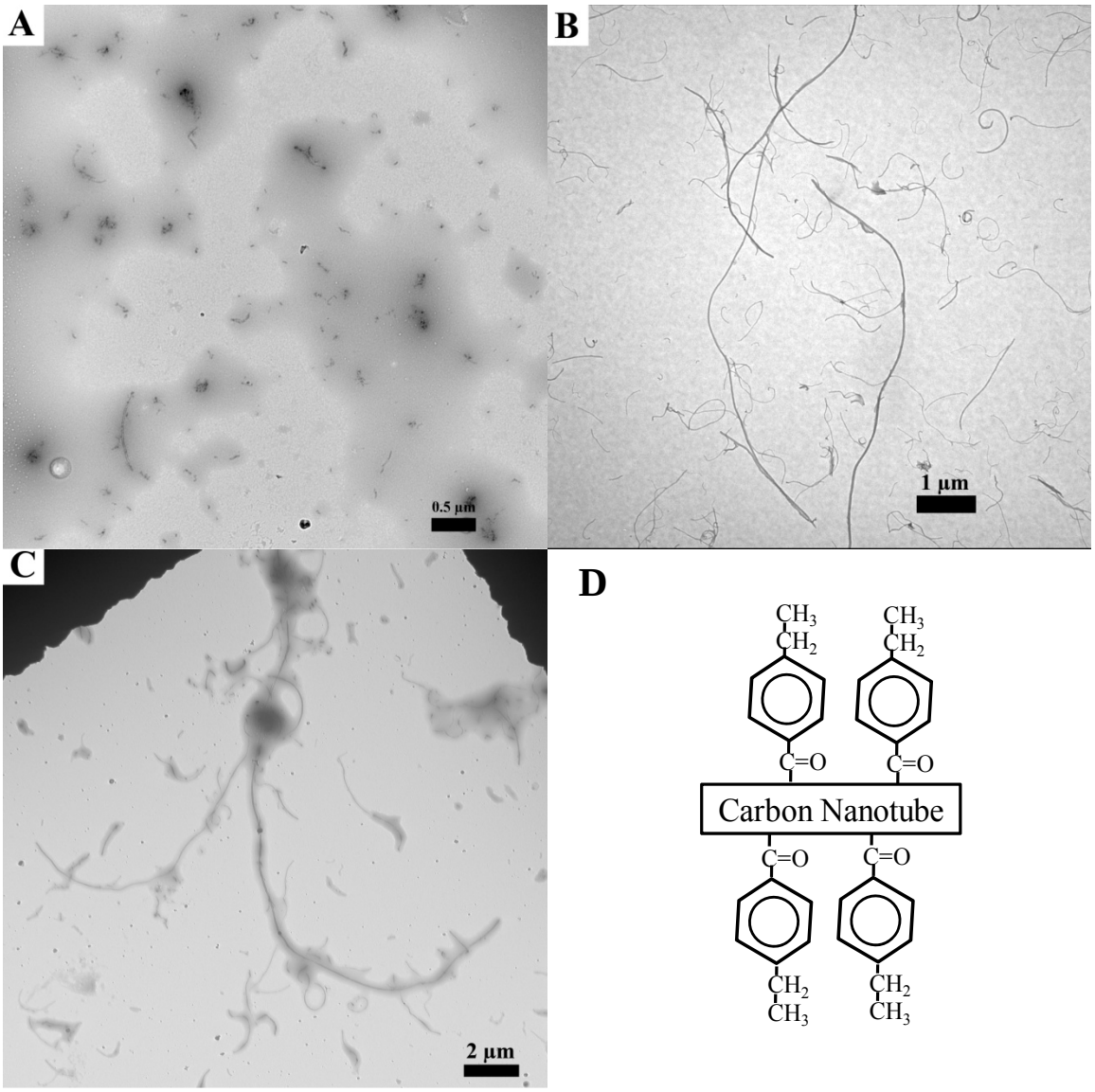

Figure 4.24. Representative TEM images of short (A), medium (B), and long (C) MWCNTs obtained from aqueous suspensions (90 mg/L) at pH 5 with an ionic strength of 75 mM. The schematic structure of functionalized MWCNT is shown in panel D.

4.6.1. CHARACTERIZATION OF MWCNT SUSPENSIONS

Images of short, medium, and long size fractions of MWCNTs functionalized with 4-EBAc are shown in Figures 4.24A, B, C, respectively. These images indicate that isolated MWCNTs were present in all of the suspensions. The length of nanotubes in the short, medium and long samples ranged from 0.2 to 1.3μm, 0.2 to 7.5 μm, and from 0.2 to 21.4 μm, respectively. Note that the functionalization method employed in this study used phosphoric acid, which is less aggressive than either nitric or sulfuric acid, and performed in the absence of ultrasonication, to minimize physical alteration such as tube shortening (Lee et al., 2008). Nevertheless, the length ranges obtained for 4-EBAc functionalized MWCNTs were substantially less than values provided by the manufacture (0.5-2 μm, 10-30 μm, and 100 μm, respectively), which were estimated based on carbon nanotube growth recipe or scanning electron microscope images of pristine carbon nanotubes (Lustig et al., 2003; Ren et al., 1998;Vajtai et al. 2004).

Further analysis of the TEM images revealed that the diameters of short, medium, and long MWCNTs ranged from 10–30 nm, 10–40 nm, and 30-70 nm, respectively. When ethoxybenzoyl moieties are covalently bonded to the MWCNT surface, the expected increase in nanotube diameter is approximately 1 nm. Comparison of the TEM-generated diameters to manufacturer-reported values for pristine MWCNTs (i.e., 10-20 nm, 10-20 nm, and 8-15 nm, respectively) suggests that there was minimal association or bundling of individual nanotubes in suspensions containing short and medium size fractions, while a greater proportion of the long MWCNTs were in bundled state. The possibility exists, however, that the values reported by the manufacturer for dry, pristine MWCNTs were not representative of the samples as received.

Size distribution of MWCNTs in aqueous suspension was further characterized using DLS. For the DLS instrument employed herein, nanoparticle size information was reported in two forms; the mean hydrodynamic diameter obtained by fitting the correlation function to a single exponential function, and the particle size distribution, based on fitting the correlation function to multiple exponential functions (Jiang et al., 2009). The mean hydrodynamic diameter of MWCNTs used in each column experiment ranged from 200 to 800 nm, and increased with increasing tube length. It is important to note that DLS size determination is based on diffusion (i.e., Stokes-Einstein equation), and thus the reported mean hydrodynamic diameter is equivalent that of a spherical particle with the same diffusion coefficient. The polydispersivity index (PDI) for all MWCNT suspensions was greater than 0.4, consistent with the MWCNT size distributions which typically exhibited a bimodal shape.

All of the dispersed MWCNTs exhibited a negative charge, with EMs ranging from -2.6 to -3.5 μm·cm/V·s (Table 4.6). For each concentration (10 or 90 mg/L), the measured EM values increased incrementally with increasing mean tube length. Since no oxidizing agent (e.g., nitric acid) or ultrasonication was used during functionalization with 4-EBAc, the presence of hydroxyl or carboxyl groups on MWCNT surface is not anticipated. Based on the Smoluchowski model (Hiemenz and Rajagopalan, 1997), the calculated zeta potential of the medium size fraction MWCNTs ranged from -38.0 to -43.6 mV, consistent with values reported in Section 4.1

4.6.2. MWCNT TRANSPORT AND RETENTION

Relative effluent MWCNT concentrations (C/C_0, where C is measured effluent concentration and C_0 is the influent concentration) were plotted against the number of dimensional PVs of influent solution introduced into the column. The resulting effluent BTCs obtained in 40-50

mesh Ottawa sand for three MWCNT size fractions, applied at input concentrations of either 10 or 90 mg/L, are shown in Figures 4.25A and 4.25C, respectively. Regardless of tube length and input concentration MWCNTs appeared in the column effluent after approximately one PV, consistent with observations in previous studies (Jaisi et al., 2008; Lui et al., 2009). In general, MWCNT relative concentrations rapidly increased to a plateau, and then decreased sharply, approaching non-detectable levels after introducing approximately one PV of the MWCNT-free background solution. The steep ascending and descending portions of the MWCNT BTCs coincided with those measured for the non-reactive tracer BTC, except for the long tube length at the lower input concentration (10 mg/L), and for the medium and long tube lengths at the higher input concentration (90 mg/L). In these cases, a concentration spike occurred near the end of the plateau that corresponded to the end of the MWCNT pulse injection, when the flow was returned to the background electrolyte solution. Here, we hypothesize that the brief period of flow stoppage (< 30 sec) followed by the re-initiation of flow allowed nanotubes that were held by interception or physical straining mechanisms, primarily near the column inlet, to be dislodged and transported through the column. This hypothesis is consistent with the increasing concentration of MWCNTs observed in the first PV of effluent after the pulse injection ceased (i.e., 4-5 PVs in Figure 4.25A and 4.25C), where the highest concentrations correspond to displaced resident solution closest to column inlet.

Regardless of the input concentration (10 or 90 mg/L), MWCNT transport was influenced by the tube length, with the plateau levels decreasing from relative concentrations of 0.97 to 0.71 when the measured tube length and mean effective hydrodynamic radius increased from 0.2-1.3 μm to 0.2-21.4 μm, and from ca. 200 to 800 nm, respectively. In a general sense, however, the 4-EBAc-functionalized MWCNTs were readily transported through the water-saturated quartz sand (d_{50} = 0.36 mm), with greater than 76% of the introduced mass appearing in the column effluent even for the longest tube lengths at an ionic strength of 75 mM. In contrast, when a plateau concentration of ca. 0.1 was observed when SWCNTs (mean d_H ca. 120 nm), applied at an input concentration of 87 mg/L and ionic strength of 55 mM (KCl), were introduced into a water-saturated sand (d_{50} = 0.26 mm) column operated at a pore-water velocity of ca. 18 m/d (Jaisi et al., 2008). This discrepancy suggests that MWCNTs functionalized with 4-EBAc are more stable relative to SWCNTs stabilized by carboxyl groups, and highlights the important role of surface properties on nanotube transport behavior.

At the conclusion of each transport experiment, the column was sectioned and extracted to obtain retention profiles, plotted as the MWCNT solid-phase concentration versus the distance from the column inlet. Measured retention profiles at input concentrations of 10 and 90 mg/L are presented in Figures 4.25B and 4.25D, respectively. These data provide quantitative information on the spatial distribution of deposited MWCNTs, which allows for assessment of conceptual and theoretical models describing coupled nanoparticle transport and deposition, and direct computation of mass balance closure, which ranged from 90.6 to 102.1% (Table 4.6).

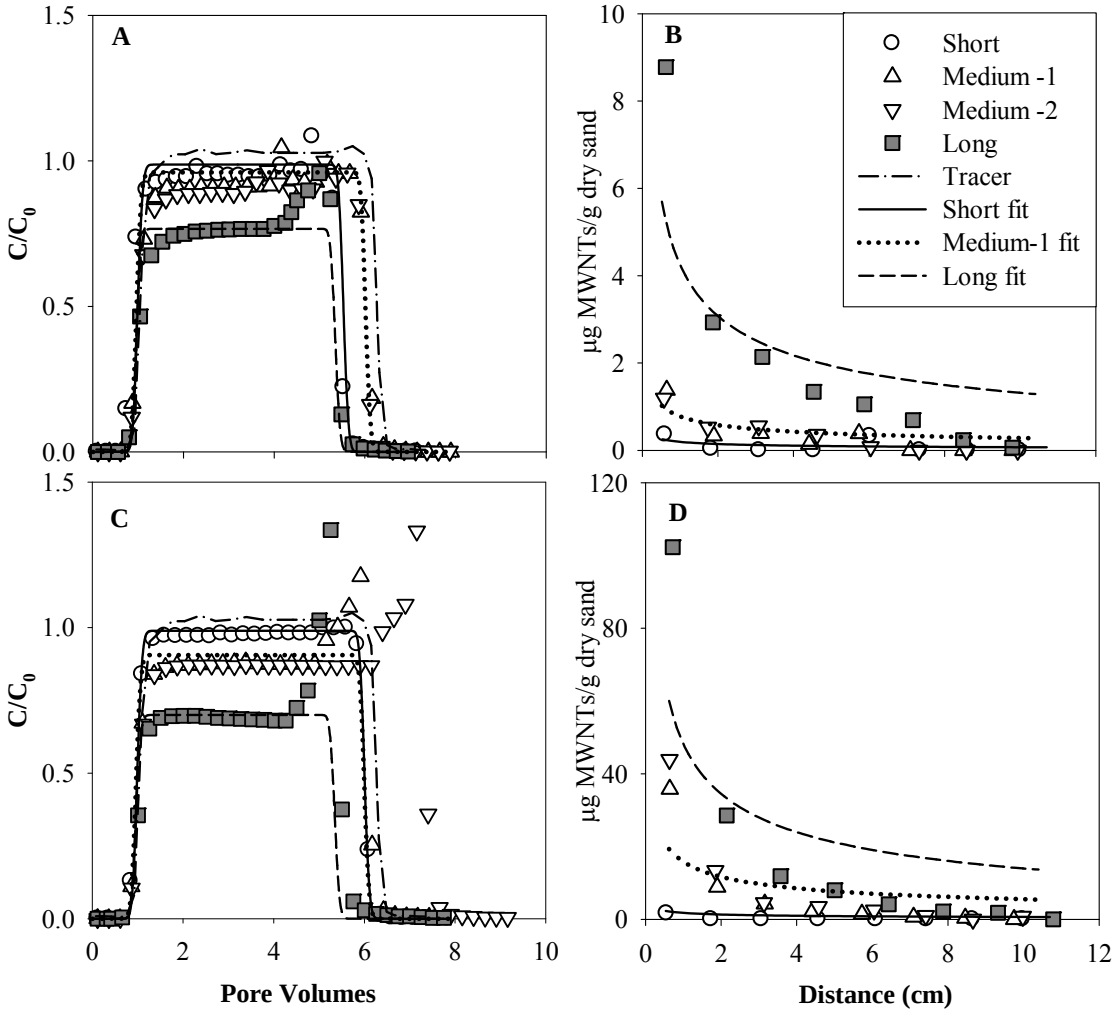

Figure 4.25. Measured and fitted effluent breakthrough curves and retention profiles of short, medium, and long MWCNTs applied to water-saturated columns packed with 40-50 mesh Ottawa sand at input concentrations of 10 mg/L (A and B) or 90 mg/L (C and D).

The amount of MWCNTs retained increased incrementally with increasing tube length for both the 10 and 90 mg/L input concentrations (Figures 4.21B and 4.21D). In addition, solid phase MWCNT concentrations decreased with increasing distance from the column inlet, a trend that is generally consistent with CBFT (Yao et al., 1971). The MWCNT retention profiles were distinct from those obtained for C_{60} fullerene nanoparticles, which exhibited relatively constant retention profiles that could be described using a maximum or limiting retention capacity blocking function (Sections 4.1 and 4.3). To investigate the effect of tube length on MWCNT deposition, and in particular, preferential retention of longer tuber lengths, five effluent samples from each of the higher input concentration experiments (90 mg/L) were imaged using TEM (Figure 4.26). Effluent samples were selected to correspond to the ascending (ca. 1.1 PV),

plateau (ca. 2.3, 3.6, and 4.7 PVs), and descending portions of the BTCs (ca. 6.0 PVs). In addition, TEM specimens were prepared from samples collected directly from syringe prior to injection (0 PV). For short (0.2 to 1.3 μm) MWCNTs, greater than 80% of total counted tubes exhibited lengths of less than 0.5 μm nanotubes, although lengths greater than 1 μm were present in all samples except at 1.1 PV. The medium MWCNT (0.2 to 7.5 μm) input suspension contained a small number of tubes with lengths greater than 7 μm, which were not observed in any of the effluent samples. A similar trend was observed with the longest size fraction of MWCNTs (0.2 to 21.4 μm), where nanotubes longer than 11 μm were not detected in any of the effluent samples. These findings suggest that MWCNTs with length greater than approximately 8 μm were preferentially removed by 40-50 quartz sand, while retention was not length selective for tube lengths of less than 8 μm.

4.6.3. MATHEMATICAL MODELING OF MWCNT TRANSPORT

Non-reactive tracer (Br^-) BTCs, which were symmetrical in shape and absent of tailing, were fit to a dimensionless form of the 1-D ADR equation. The fitted retardation factor for all tracer experiments was 1.01 ± 0.01, while the hydrodynamic dispersion coefficient (D_H) was 0.067 ± 0.01 cm^2/min, consistent with results reported in previous work with the same size fraction of Ottawa sand (Section 2.1). These findings indicate that water flow through the column was ideal, and more specifically, that physical non-equilibrium processes (e.g., diffusion into regions of immobile water) did not influence MWCNT transport and retention.

Initial simulations of MWCNT transport and deposition were performed using a mathematical model based on clean-bed filtration theory (CBFT). The CBFT model accurately captured the flat plateau, as well as the sharp ascent and descent of the MWCNT BTCs yielding attachment rate coefficients that ranged from 1.9×10^{-3} to 12.7×10^{-3} min^{-1} , and increased with tube length. However, model fits to the corresponding MWCNT retention profiles were generally poor, failing to match the relatively large concentration of MWCNTs deposited near the column inlet, and the exponential decrease in retained mass with travel distance. In an effort to improve the retention profile fits, the least squares fitting routine in HYDRUS 1-D was modified from equal weighting of the BTC and retention profile. The weight of the effluent BTC was varied from 0.001 to 2, while the retention profile weighting was kept as a constant of one. The resulting retention profiles simulations increased in magnitude and remained relatively constant with travel distance (flat) as the value of the BTC weighting function was increased to 2. An alternative approach, involving manual adjustment of the attachment rate (k_{att}) from 0.002 to 2.0 min^{-1}, was then employed to determine if the general shape of the retention profile could be reproduced. A one order-of-magnitude increase in the value of k_{att} (0.02 min^{-1}) decreased the breakthrough curve plateau from a relative concentration of 0.96 to 0.68 and greatly increased the magnitude of the retention profile, such that neither the simulation BTC nor the retention profile corresponded to the measured data. These trends were accentuated at higher values of k_{att}, where simulated BTCs were not observable (i.e., complete retention) and the corresponding retention profile became very large although the general shape of the profile was more consistent with the observed elevation of MWCNT retention near the column inlet. These findings demonstrate that mathematical model based on CBFT was not able to simulate both the measured BTC and retention data, and clearly illustrates the potential errors that may arise when filtration models are only fit to effluent concentration data.

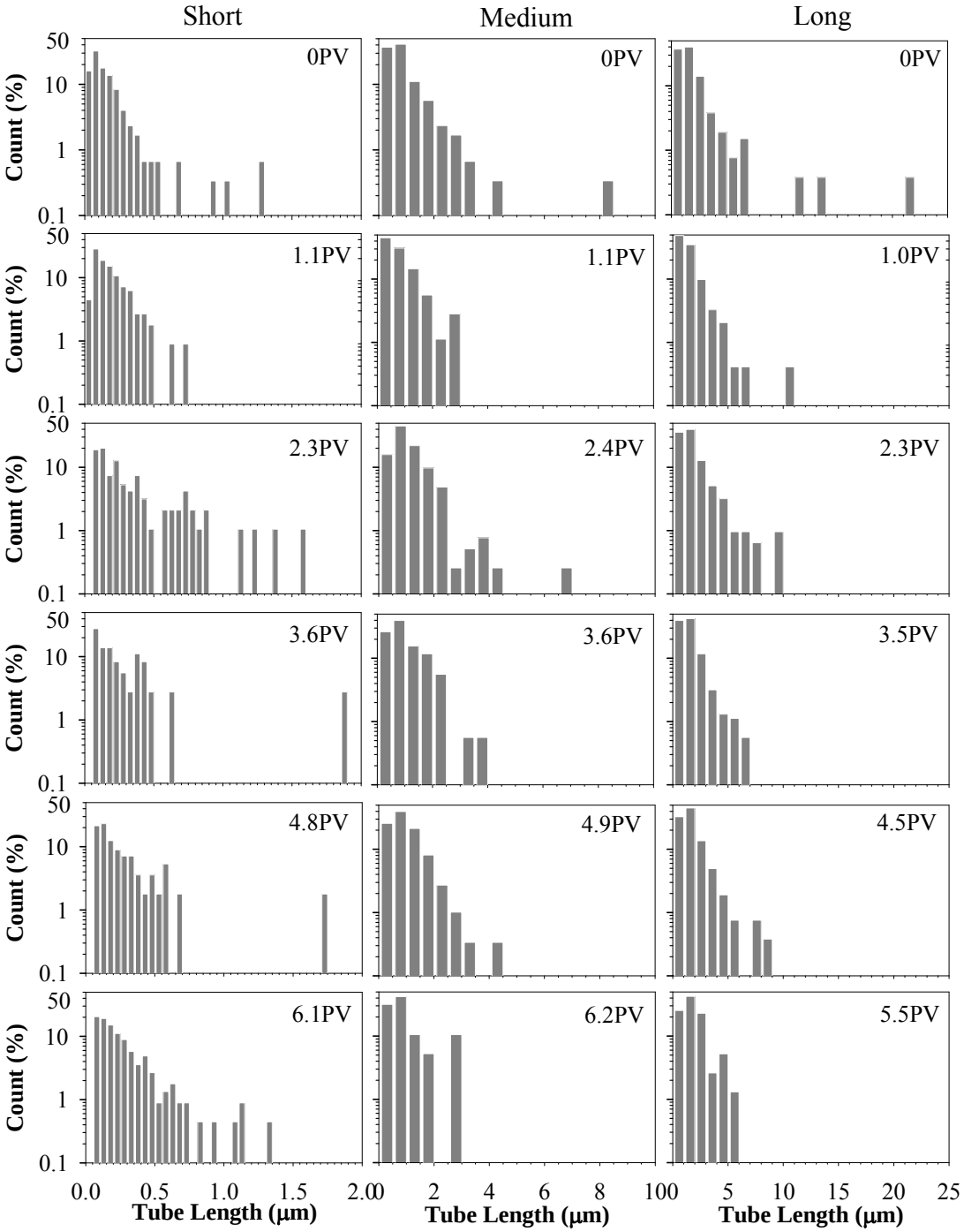

Figure 4.26. Length distribution of MWCNTs obtained from TEM image analysis of samples collected immediately prior to injection (0 PV) and in column effluent samples. Each bar represents a length range of 0.05, 0.5, and 1 μm for short-, medium-, and long-MWCNTs, respectively.

Despite efforts to improve model fit to the measured retention data, it is apparent that CBFT alone is not able to capture the high concentrations near the column inlet, which was most apparent for MWCNTs with the longest tube lengths (0.2 to 21.4 μm). This type of particle retention profile is characteristic of a physical straining phenomenon, where particles are retained or trapped at intersections of grain to grain contact points, which may result in pore throat blockage. For example, Bradford et al. (2003) reported almost complete retention of colloids at the inlet of columns packed with either quartz sand or glass beads. Based on comparisons with fullerene (C_{60}) and responses to changes in solution chemistry, Jaisi and Elimelech (2009) concluded that physical straining controlled the filtration and transport of carboxyl functionalized SWCNTs (0.6 to 8 μm tube length) in a water-saturated soil (aggregate sizes of 0.42 to 1.00 mm).

Therefore, the mathematical model (see eq 3.11-3.15) was refined to account MWCNT deposition as a combination of first-order attachment and physical straining:

$$\frac{\rho_b}{\theta_w}\frac{\partial S}{\partial t} = k_{att}C + k_{str}\psi C \tag{4}$$

where k_{str} is the straining rate coefficient and ψ is the depth-dependent blocking coefficient, expressed as:

$$\psi = \left(\frac{d_c + x}{d_c}\right)^{-\beta} \tag{5}$$

Here, d_c is the median grain size and β is an empirical factor with a value of 0.432. These equations were solved using the Hydrus-1D model, version 4.14 (Simunek et al., 2005) with k_{att} and k_{str} as fitting parameters. Non-reactive tracer BTCs were fit to the dimensionless form of the 1-D advective-dispersive-reactive (ADR) transport equation (3.5-3.6) using CXTFIT ver. 2.0 (Toride et al., 1999) to independently obtain D_H and assess flow conditions.

As anticipated, greatly improved fits to the MWCNT retention profiles (Figure 4.25) were obtained, with minimal impact on the BTC fits, relative to those obtained when the unmodified CBFT model was used. The resulting physical straining rates (k_{str}) were more than four orders-of-magnitude greater than the corresponding attachment rates (k_{att}), which now ranged from 1.78 x 10^{-7} to 5.15 x 10^{-5} min^{-1} (Table 4.6). These results indicate that the physical straining contributed far more significantly to MWCNT retention than traditional physic-chemical deposition processes under the conditions investigated herein, consistent with the findings of Jaisi and Elimelech (2009) for SWCNTs in an aggregated soil. Furthermore, the fitted straining rates increased dramatically with increasing tube length. For example, the straining rates obtained for longest MWCNTs were two orders-of-magnitude greater than those of the shortest MWCNTs (0.2 to 1.3 μm). Although physical straining played a dominant role in MWCNT retention, more than 75% of total delivered mass was transported through the column (Table 4.6). This rather high mobility is attributed to the relatively large negative surface charge of the functionalized MWCNTs (ca. -40 mV), coupled with the potential alignment of the shorter nanotubes with the local flow direction, a phenomenon that has been observed with non-spherical latex microspheres Xu et al. (2008).

CHAPTER 5

PUBLICATIONS, PRESENTATIONS, AND PERSONNEL

5.1. JOURNAL PUBLICATIONS

1. Li, Y., Y. Wang, Y., K.D. Pennell, L.M. Abriola. 2008. Investigation of the transport and deposition of fullerene (C60) nanoparticles in quartz sand under varying flow conditions. *Environmental Science and Technology*, 42:7174-7180.
2. Wang, Y., Li, Y., K.D. Pennell. 2008. Influence of electrolyte concentration and species on the aggregation and transport of fullerene nanoparticles in quartz sand. *Environmental Toxicology & Chemistry*, 29: 1860-1867.
3. Wang, Y., Y. Li, J.F. Fortner, J.B. Hughes, L.M. Abriola, K.D. Pennell. 2008. Transport and retention of nanoscale C60 aggregates in water-saturated porous media. *Environmental Science and Technology*, 42:3588-3594.
4. Wang, Y., Y. Li, H. Kim, S.L. Walker, L.M. Abriola, K.D. Pennell. 2010. Transport and retention of fullerene nanoparticles in natural soils. *Journal of Environmental Quality* 39:1925-1933.
5. Wang, Y., J.-H. Kim, J.-B. Baek, G.W. Miller, K.D. Pennell. 2011. Transport behavior of multi-wall carbon nanotubes in water-saturated quartz sand as a function of tube length. *Environmental Science and Technology* (in review).

5.2. BOOK CHAPTERS

1. Hatcher, J.H., D.P. Jones, G.W. Miller, K.D. Pennell. 2008. Neurotoxicity of ambient and manufactured nanoparticles. In Nanoscience and Nanotechnology: Environmental and Health Impacts, Grassian, V.H. (Ed.), Chapter 16, John Wiley & Sons, NY.
2. Pennell, K.D., J. Costanza, Y. Wang. 2008. Transport and retention of nanomaterials in water-saturated porous media. In Nanoscience and Nanotechnology: Environmental and Health Impacts, Grassian, V.H. (Ed.), Chapter 5, John Wiley & Sons, NY.

5.3. CONFERENCE PROCEEDINGS AND PRESENTATIONS

1. Pennell, K.D., Abriola, L.M., Wang, Y., Li, Y. 2008. Transport and retention of fullerene nanoparticles in porous media. American Geophysical Union National Meeting, December 15-19, 2008, San Francisco, CA. (invited)
2. Wang, Y., Li, Y., Abriola, L.M., Pennell, K.D. 2008. Transport and retention of fullerene (C60) nanoparticles in natural soils. American Geophysical Union National Meeting, December 15-19, 2008, San Francisco, CA.
3. Li, Y., Wang, Y., Pennell, K.D., Abriola, L.M. 2008. Modeling of the transport and retention of fullerene C60 aggregate in porous media. American Geophysical Union National Meeting, December 15-19, 2008, San Francisco, CA.
4. Pennell, K.D., J.B. Hughes, L.M. Abriola, Y. Wang, Y. Li, J.D. Fortner. 2008. Fate and transport C60 nanomaterials in unsaturated and saturated soils. Interagency Workshop on the Environmental Implications of Nanotechnology, U.S. Environmental Protection Agency, November 19-21, 2008, Tampa, FL.

5. Wang, Y., Y. Li, L.M. Abriola, K.D. Pennell. 2008. Transport of fullerene nanoparticles in quartz sands: Experiments and modeling. Joint Geological Society of America and Soil Science Society of America Meeting, October 5-9, 2008, Houston, TX.

6. Li, Y. Wang, Y., Abriola, L.M., Pennell, K.D. 2008. Influence of flow rate, grain size, electrolyte species and concentration on the transport and retention of fullerene C60 aggregates in saturated porous media. International Environmental Nanotechnology Conference: Applications and Implications, U.S. Environmental Protection Agency, October 7-9, 2008, Chicago, IL.

7. Wang, Y., K.D. Pennell 2008. Effects of surfactant and natural organic matter on the transport of nanoscale C60 aggregates under water-saturated conditions. Gordon Research Conference, Environmental Sciences: Water, June 22-27, 2008. Holderness, NH.

8. Li, Y., Y. Wang, K.D. Pennell, L.M. Abriola. 2007. Investigation of n-C60 nanoparticle transport and retention in saturated porous media. American Geophysical Union National Meeting, December 10-14, 2007, San Francisco, CA.

9. Pennell, K.D., J.B. Hughes, L.M. Abriola, Y. Wang, Y. Li, J.D. Fortner. 2007. Transport of nC60 through soils: experiments and theory. Nanoscale Science and Engineering Conference, National Science Foundation, December 3-6, 2007, Arlington, VA. (invited).

10. Pennell, K.D., J.B. Hughes, L.M. Abriola, Y. Wang, Y. Li, J.D. Fortner. 2007. Transport and retention of nanoscale fullerene aggregates in water-saturated soils. Interagency Workshop on the Environmental Implications of Nanotechnology, U.S. Environmental Protection Agency, September 5-7, 2007, Washington, DC.

11. Li, Y., Y. Wang, L.M. Abriola, K.D. Pennell. 2007. Influence of grain size and flow rate on the transport and retention of C-60 fullerene in water-saturated soils. Special Session on Colloid and Interfacial Phenomena in Environmental Systems, 81st Colloid and Surface Science Symposium, June 24-27, 2007, Newark, NJ.

12. Wang, Y., Y. Li, J.D. Fortner, J.B. Hughes, L.M. Abriola, and K.D. Pennell. 2007. Transport and retention of C60-fullerene in water-saturated soils. In Preprints of Extended Abstracts, 47(1), Special Symposium on Environmental Characterization, Impacts and Applications of Nanocarbons, Division of Environmental Chemistry, American Chemical Society 233rd National Meetings, March 25-29, 2007, Chicago, IL.

13. Pennell, K.D., J.B. Hughes, L.M. Abriola, Y. Wang, Y. Li, Y., J.D. Fortner. 2006. Fate and transport of carbon nanomaterials in unsaturated and saturated soils. Nanotechnology Environmental Implications, U.S. Environmental Protection Agency, November 13-14, 2006, Arlington, VA.

5.4. STUDENTS AND POST-DOCS SUPPORTED BY THE PROJECT

1. Mingjie Chen, Research Assistant Professor, Department of Civil and Environmental Engineering, Tufts University, Period of Involvement: November 2008-September 2009 (currently Research Engineer and Lawrence Livermore Laboratory)

2. Yonggang Wang, Ph.D. Candidate, Environmental Engineering Program, School of Civil and Environmental Engineering, Georgia Institute of Technology, Period of Involvement: November 2005-September 2009 (currently Post-Doctoral Fellow at Tufts University)

3. Yusong Li, Ph.D., Post-Doctoral Fellow, Department of Civil and Environmental Engineering, Tufts University, Period of Involvement: November 2005-December 2008, (currently Assistant Professor at University of Nebraska-Lincoln).
4. John D. Fortner, Ph.D., Post-Doctoral Fellow, School of Civil and Environmental Engineering, Georgia Institute of Technology, Period of Involvement: November 2005-October 2007 (currently Assistant Professor at Washington University)

CHAPTER 6

REFERENCES CITED

Andrievsky, G.V., M.V. Kosevich, O.M. Vovk, V.S. Shelkovsky, L.S. Vashchenko. 1995. On the production of an aqueous colloidal solution of fullerenes. J. Chem. Soc. Comm., 12: 1281-1282.

Bensasson, R.V., E. Bienvenue, M. Dellinger, S. Leach, P. Seta. 1994. C_{60} in model biological systems. A visible-UV absorption study of solvent-dependent parameters and solute aggregation. J. Phys. Chem., 98: 3492-3500.

Bhattacharjee, S. and M. Elimelech. 1997. Surface element integration: A novel technique for evaluation of DLVO interaction between a particle and a flat plate. J. Colloid Interface Sci., 193:273-285.

Bradford, S. A., S.R. Yates, M. Bettahar, J. Simunek, J. 2002. Physical factors affecting the transport and fate of colloids in saturated porous media. Water Resour. Res., 38: 1327-1338.

Bradford, S.A., J. Simunek, M. Bettahar, M.Th. Van Genuchten, and S.R. Yates. 2003. Modeling colloid attachment, straining, and exclusion in saturated porous media. Environ. Sci. Technol.**,** 37: 2242-2250.

Bradford, S. A., J. Simunek, M. Bettahar, Y.F. Tadassa, M.Th. van Genuchten, S.R. Yates. 2005. Straining of colloids at textural interfaces. Water Resour. Res., 41:.

Brant, J., H. Lecoanet, and M.R. Wiesner. 2005. Aggregation and deposition characteristics of fullerene nanoparticles in aqueous systems. J. Nanopart. Res. 7:545-553.

Chen, K.L., and M. Elimelech. 2006. Aggregation and deposition kinetics of fullerene (C-60) nanoparticles. Langmuir 22:10994-11001.

Cheng, X., A.T. Kan, and M.B. Thomson. 2005. Study of C60 transport in porous media and the effect of sorbed C60 on naphthalene transport. J. Mater. Res. 20:3244-3254.

Chin, Y.P., G. Aiken, and E. Oloughlin. 1994. Molecular weight, polydispersity, and spectroscopic properties of aquatic substances. *Environ. Sci. Technol*., 28:1853-1858.

Degennes, P.G. 1987. Polymers at an interface: A simplified view. Adv. Colloid Interface Sci. 27:189-209.

Deguchi, S., R.G. Alargova, and K. Tsujii. 2001. Stable dispersions of fullerenes, C-60 and C-70, in water. Preparation and characterization. Langmuir 17:6013-6017.

Deguchi, S., S. Mukai, M. Tsudome, and K. Horikoshi. 2006. Facile generation of fullerene nanoparticles by hand-grinding. Adv. Mater. 18:729-732.

Elimelech, M. and C.R. O'Melia. 1990. Kinetics of deposition of colloidal particles in porous media. *Environ. Sci. Technol.*, 24, 1528-1536.

Elimelech, M., J. Gregory, X. Jia, R.A. Williams. 1995. Particle Deposition and Aggregation: Measurement, Modeling and Simulation. Butterworth-Heinemann: Woburn, MA.

Espinasse, B., E.M. Hotze, and M.R. Wiesner. 2007. Transport and retention of colloidal aggregates of C-60 in porous media: Effects of organic macromolecules, ionic composition, and preparation method. Environ. Sci. Technol., 41:7396-7402.

Fortner, J.D., D.Y. Lyon, C.M. Sayes, A.M. Boyd, J.C. Falkner, E.M. Hotze, L.B. Alemany, Y.J. Tao, W. Guo, K.D. Ausman, V.L. Colvin, and J.B. Hughes. 2005. C60 in water: Nanocrystal formation and microbial response. Environ. Sci. Technol., 39:4307.

Franchi, A. and C.R. O'Melia. 2003. Effects of natural organic matter and solution chemistry on the deposition and reentrainment of colloids in porous media. Environ. Sci. Technol., 37: 1122-1129.

Freeze, R. A. and J.A. Cherry. 1979. Groundwater, Prentice Hall: Upper Saddle River, NJ.

Guzman, K. A. D. M.P. Finnegan, and J.F. Banfield. 2006. Influence of surface potential on aggregation and transport of titania nanoparticles. Environ. Sci. Technol., 40: 7688-7693.

Harvey, R. W. and S.P. Garabedian. 1991. Use of colloid filtration theory in modeling movement of bacteria through a contaminated sandy aquifer. Environ. Sci. Technol., 25, 178-185.

Hayase, K. and H. Tsubota. 1983. Sedimentary humic-acid and fulvic-acid as surface-active substances. Geochim. Cosmochim. Acta**,** 47: 947-952.

Henry, T.B., F.M. Menn, J.T. Fleming, J. Wilgus, R.N. Compton, G.S. Sayler. 2007. Attributing effects of aqueous C-60 nano-aggregates to tetrahydrofuran decomposition products in larval zebrafish by assessment of gene expression. Environ. Health Perspect., 115: 1059-1065.

Hiemenz, P.C. and R. Rajagopalan. 1997. Principles of Colloid and Surface Chemistry, 3rd ed; Marcel Dekker, Inc.: New York, NY.

Hong, S.K., and M. Elimelech. 1997. Chemical and physical aspects of natural organic matter (NOM) fouling of nanofiltration membranes. J. Membrane Sci. 132:159-181.

Hyung, H., J.D. Fortner, J.B. Hughes, J.H. Kim. 2007. Natural organic matter stabilizes carbon nanotubes in the aqueous phase. Environ. Sci. Technol., 41: 179-184.

Iijima, S. 1991. Helical microtubules of graphitic carbon. Nature, 354:56-58.

Isaacson, C.W., C.Y. Usenko, R.L. Tanguay, and J.A. Field. 2007. Quantification of fullerenes by LC/ESI-MS and its application to in vivo toxicity assays. Anal. Chem. 79:9091-9097.

Israelachvili, J. 1992. Intermolecular and Surface Forces, 2nd ed.; Academic Press Inc.: San Diego, CA.

Jaisi, D.P., N.B. Saleh, R.E. Blake, and M. Elimelech. 2008. Transport of Single-Walled Carbon Nanotubes in Porous Media: Filtration Mechanisms and Reversibility. Environ. Sci. Technol., 42:8317-8323.

Jaisi, D.P. and M Elimelech. 2009. Single-walled carbon nanotubes exhibit limited transport in soil columns. Environ. Sci. Technol., 43: 9161-9166.

Jiang, J.K., G. Oberdorster, and P. Biswas. 2009. Characterization of size, surface charge, and agglomeration state of nanoparticle dispersions for toxicological studies. J. Nanopart. Res., 11: 77-89.

Johnson, P.R. and M. Elimelech. 1995. Dynamics of colloid deposition in porous media - Blocking based on random sequential adsorption. Langmuir, 11: 801-812.

Karagunduz, A., K.D. Pennell, and M.H. Young. 2001. Influence of a nonionic surfactant on the water retention properties of unsaturated soils. Soil Sci. Soc. Am. J., 65:1392-1399.

Kaya, A. and Y. Yukselen. 2005. Zeta potential of clay minerals and quartz contaminated by heavy metals. Canad. Geotech. J., 42:1280-1289.

Ko, C.-H. and M. Elimelech. 2000. The "shadow effect" in colloid transport and deposition dynamics in granular porous media: Measurements and mechanisms. Environ. Sci. Technol., 34*:* 3681-3689.

Ko, C.H., S. Bhattacharjee, M. Elimelech. 2000. Coupled influence of colloidal and hydrodynamic interactions on the RSA dynamic blocking function for particle deposition onto packed spherical collectors. J. Colloid Interface Sci., 229, 554-567.

Kroto, H.W., J.R. Heath, S.C. Obrien, R.F. Curl, and R.E. Smalley. 1985. C60-Buckminsterfullerene. Nature, 318:162-163.

Kuznar, Z.A. and M. Elimelech. 2004. Adhesion kinetics of viable *Cryptosporidium parvum* oocysts to quartz sand. Environ. Sci. Technol., 38: 6839-6845.

Lecoanet, H.F., and M.R. Wiesner. 2004. Velocity effects on fullerene and oxide nanoparticle deposition in porous media. Environ. Sci. Technol., 38:4377-4382.

Lecoanet, H.F., J.-Y. Bottero, and M.R. Wiesner. 2004. Laboratory assessment of the mobility of nanomaterials in porous media. Environ. Sci. Technol., 38:5164-5169.

Lee, H.J., S.W. Han, Y.D. Kwon, L.S. Tan, and J.B. Baek. 2008. Functionalization of multi-walled carbon nanotubes with various 4-substituted benzoic acids in mild polyphosphoric acid/phosphorous pentoxide. Carbon 46:1850-1859.

Levich, V.G.. 1962. Physicochemical Hydrodynamics. Prentice-Hall, Englewood Cliffs, N.J.

Li, X.Q., T.D. Scheibe, and W.P. Johnson. 2004. Apparent decreases in colloid deposition rate coefficients with distance of transport under unfavorable deposition conditions: A general phenomenon. Environ. Sci. Technol., 38: 5616-5625.

Lustig, S.R. E.D. Boyes, R.H. French, T.D. Gierke, M.A. Harmer, P.B. Hietpas, A. Jagota, R.S. McLean, G.P. Mitchell, G.B. Onoa, and K.D. Sams. 2003. Lithographically cut single-walled carbon nanotubes: Controlling length distribution and introducing end-group functionality. Nano Lett., 3: 1007-1012.

Lyon, D.Y., J.D. Fortner, C.M. Sayes, V.L. Colvin, J.B. Hughes. 2005. Bacterial cell association and antimicrobial activity of a C_{60} water suspension. Environ. Toxicol. Chem., 24: 2757-2762.

Maynard, A.D., R.J. Aitken, T. Butz, V. Colvin, K. Donaldson, G. Oberdorster, M.A. Philbert, J. Ryan, A. Seaton, V. Stone, S.S. Tinkle, L. Tran, N.J. Walker, D.B. Warheit. 2006. Safe handling of nanotechnology. Nature, 444*:* 267-269.

Nel, A.; T. Xia, L. Madler, and N. Li. 2006. Toxic potential of materials at the nano level. Science, 311: 622-627.

Oberdorster, E. 2004. Manufactured nanomaterials (Fullerenes, C-60) induce oxidative stress in the brain of juvenile largemouth bass. Environ. Health Perspect., 112: 1058-1062.

Pennell, K.D., L.M. Abriola, and W.J. Weber, Jr. 1993. Surfactant-enhanced solubilization of residual dodecane in soil columns. 1. Experimental investigation. Environ. Sci. Technol., 27:2332-2340.

Pennell, K.D., S.A. Boyd, and L.M. Abriola. 1995. Surface area of soil organic matter reexamined. Soil Sci. Soc. Am. J., 59:1012.

Pennell, K.D., A.M. Adinolfi, L.M. Abriola, and M.S. Diallo. 1997. Solubilization of dodecane, tetrachloroethylene, and 1,2-dichlorobenzene in micellar solutions of ethoxylated nonionic surfactants. Environ. Sci. Technol., 31:1382-1389.

Ramsburg, C.A. and K.D. Pennell. 2001. Experimental and economic assessment of two surfactant formulations for source zone remediation at a former dry cleaning facility. Ground Water Monitor. Remed., 21:68-82.

Rao, S.R. and J.A. Finch. 2003. Base metal oxide flotation using long chain xanthates. Int. J. Miner. Process., 69: 251-258

Relan, P.S., K.K. Girdhar, and S.S. Khanna. 1984. Molecular-configuration of compost humic acid by viscometric studies. Plant Soil 81:203-208.

Ren, Z.F., Z.P. Huang, J.W. Xu, J.H. Wang, P. Bush, M.P. Siegal, P.N Provencio. 1998. Synthesis of large arrays of well-aligned carbon nanotubes on glass. Science, 282: 1105-1107.

Saiers, J. E., G.M. Hornberger, and L.Y. Liang. 1994. First-order and second-order kinetics approaches for modeling the transport of colloidal particles in porous media. Water Resour. Res., 30: 2499-2506.

Saleh, N.B., L.D. Pfefferle, and M. Elimelech. 2008. Aggregation kinetics of multi-walled carbon nanotubes in aquatic systems: Measurements and environmental implications. Environ. Sci. Technol., 42:7963-7969.

Sayes, C.M., A.M. Gobin, and K.D. Ausman, J. Mendez, J.L.West, V.L. Colvin.2005. Nano C60 cytotoxicity is due to lipid peroxidation. Biomater. 26: 7587-7595.

Shen, C. Y., B.G. Li, Y.F. Huang, Y. Jin. 2007. Kinetics of coupled primary- and secondary-minimum deposition of colloids under unfavorable chemical conditions. Environ. Sci. Technol.**,** 41: 6976-6982.

Simunek, J.; Genuchten, M. T. V.; Sejna, M. 2005. The HYDRUS-1D Software Package for Simulating the Movement of Water, Heat, and Multiple Solutes in Variably Saturated Media, Version 3.0, HYDRUS Software Series 1, Department of Environmental Sciences, University of California Riverside: Riverside, CA.

Song, L.F., P.R. Johnson, M. Elimelech. 1994. Kinetics of colloid deposition onto heterogeneously charged surfaces in porous media. Environ. Sci. Technol., 28:1164-1171.

Terashima, M. and S. Nagao. 2007. Solubilization of fullerene in water by aquatic humic substances. Chem. Lett. 36: 302-303.

Tiraferri, A., and R. Sethi. 2009. Enhanced transport of zerovalent iron nanoparticles in saturated porous media by guar gum. J. Nanopart. Res. 11:635-645.

Toride, N., F.J. Leij, M.Th. van Genuchten. 1999. The CXTFIT Code for Estimating Transport Parameters from Laboratory or Field Tracer Experiments, Version. 2.1; Research Report No. 137, U.S. Department of Agriculture, Salinity Laboratory: Riverside, CA.

Tufenkji, N., J.A. Redman, and M. Elimelech. 2003. Interpreting deposition patterns of microbial particles in laboratory-scale column experiments. Environ. Sci. Technol., 37: 616-623.

Tufenkji, N. and M. Elimelech. 2004. Correlation equation for predicting single-collector efficiency in physicochemical filtration in saturated porous media. Environ. Sci. Technol., 38: 529-536.

Tufenkji, N. and M. Elimelech. 2005. Spatial distributions of Cryptosporidium oocysts in porous media: Evidence for dual mode deposition. Environ. Sci. Technol., 39: 3620-3629.

Vaidyanathan, R. and C. Tien. 1991. Hydrosol Deposition in antigranualocytes media under unfavorable surface conditions. Chem. Eng. Sci., 46: 967-983.

Vajtai, R., B.Q. Wei, P.M. Ajayan.2004. Controlled growth of carbon nanotubes. Phil. Trans. Royal Soc. London Ser. A-Mathemat. Phys. Eng. Sci., 362: 2143-2160.

Wang, P., Q.H. Shi, H.J. Liang, D.W. Steuerman, G.D. Stucky, and A.A. Keller. 2008. Enhanced environmental mobility of carbon nanotubes in the presence of humic acid and their removal from aqueous solution. Small, 4: 2166-2170.

Wiesner, M.R., G.V. Lowry, P. Alvarez, D. Dionysiou, and P Biswas. 2006. Assessing the risks of manufactured nanomaterials. Environ. Sci. Technol., 40: 4336-4345.

Xia, X.R., N.A. Monteiro-Riviere, and J.E. Riviere. 2006. Trace analysis of fullerenes in biological samples by simplified liquid-liquid extraction and high-performance liquid chromatography. J. Chromat. A, 1129:216-222.

Xu, S.P., B. Gao, and J.E. Saiers. 2006. Straining of colloidal particles in saturated porous media. Water Resour. Res., 42:

Xu, S.P., Q. Liao, and J.E. Saiers. 2008. Straining of nonspherical colloids in saturated porous media. Environ. Sci. Technol., 42: 771-778.

Yao, K. M.; Habibian, M. M.; Omelia, C. R. 1971. Water and waste water filtration - Concepts and applications. *Environ. Sci. Technol.*, *5*, 1105-1109.

Zhdanov, S. P., L.S. Kosheleva, T.I. Titova. 1987. IR Study of hydroxylated silica. Langmuir, 3: 960-967.